

NAVAL POSTGRADUATE SCHOOL

Monterey, California



THESIS

**APPLICATIONS OF ARBITRARY
LAGRANGIAN EULERIAN (ALE) ANALYSIS
APPROACH TO UNDERWATER AND AIR
EXPLOSION PROBLEMS**

by

Theodore Trevino

September 2000

Thesis Advisor:

Young S. Shin

Approved for public release; distribution is unlimited.

DTIC QUALITY INSPECTED 4

20001128 096

REPORT DOCUMENTATION PAGE

Form Approved OMB No. 0704-0188

Public reporting burden for this collection of information is estimated to average 1 hour per response, including the time for reviewing instruction, searching existing data sources, gathering and maintaining the data needed, and completing and reviewing the collection of information. Send comments regarding this burden estimate or any other aspect of this collection of information, including suggestions for reducing this burden, to Washington Headquarters Services, Directorate for Information Operations and Reports, 1215 Jefferson Davis Highway, Suite 1204, Arlington, VA 22202-4302, and to the Office of Management and Budget, Paperwork Reduction Project (0704-0188) Washington DC 20503.

1. AGENCY USE ONLY (Leave blank)		2. REPORT DATE September 2000	3. REPORT TYPE AND DATES COVERED Master's Thesis
4. TITLE AND SUBTITLE: Applications of Arbitrary Lagrangian-Eulerian (ALE) Analysis Approach to Underwater and Air Explosion Problems			5. FUNDING NUMBERS
6. AUTHOR(S) Trevino, Theodore			
7. PERFORMING ORGANIZATION NAME(S) AND ADDRESS(ES) Naval Postgraduate School Monterey CA 93943-5000			8. PERFORMING ORGANIZATION REPORT NUMBER
9. SPONSORING/MONITORING AGENCY NAME(S) AND ADDRESS(ES)			10. SPONSORING/MONITORING AGENCY REPORT NUMBER
11. SUPPLEMENTARY NOTES The views expressed here are those of the authors and do not reflect the official policy or position of the Department of Defense or the U.S. Government.			
12a. DISTRIBUTION/AVAILABILITY STATEMENT Approved for public release; distribution is unlimited.			12b. DISTRIBUTION CODE
13. ABSTRACT (maximum 200 words) <p>A series of underwater and air explosion investigations was conducted using the Arbitrary Lagrangian-Eulerian (ALE) numerical technique. The investigation primarily examined the explosive-fluid, fluid-structure, and fluid-air interaction effects, and the shock wave pressure propagation through a subjected medium, with the intent of verifying and validating the ALE analysis. The research also noted the explosive-air and air-structure interaction effects as well as shock wave pressure propagation effects. Three-dimensional underwater explosion analyses was conducted using TNT detonations. Two-dimensional air explosion analyses was completed using TNT detonations. With viable ALE results, underwater and air explosion modeling and simulation could become dependable, cost-effective, and time-efficient.</p>			
14. SUBJECT TERMS Underwater Explosion, Air Explosion, Arbitrary Lagrangian-Eulerian Analysis			15. NUMBER OF PAGES 202
			16. PRICE CODE
17. SECURITY CLASSIFICATION OF REPORT Unclassified	18. SECURITY CLASSIFICATION OF THIS PAGE Unclassified	19. SECURITY CLASSIFICATION OF ABSTRACT Unclassified	20. LIMITATION OF ABSTRACT UL

NSN 7540-01-280-5500

Standard Form 298 (Rev. 2-89)
Prescribed by ANSI Std. Z39-18 298-102

THIS PAGE INTENTIONALLY LEFT BLANK

Approved for public release; distribution is unlimited

**APPLICATIONS OF ARBITRARY LAGRANGIAN-EULERIAN (ALE)
ANALYSIS APPROACH TO UNDERWATER AND AIR EXPLOSION
PROBLEMS**

Theodore Trevino
Lieutenant, United States Navy
B.S., University of Arizona, 1991

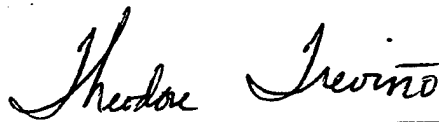
Submitted in partial fulfillment of the
Requirements for the degree of

MASTER OF SCIENCE IN MECHANICAL ENGINEERING

from the

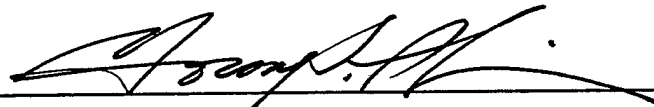
**NAVAL POSTGRADUATE SCHOOL
September 2000**

Author:

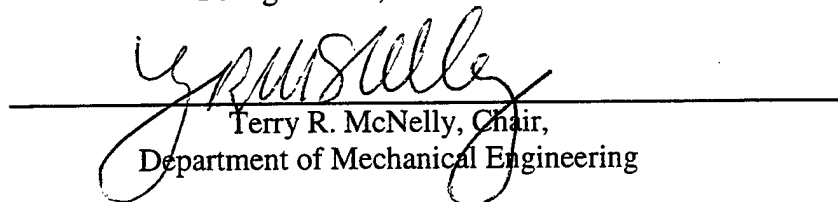


Theodore Trevino

Approved by:



Young S. Shin, Thesis Advisor



Terry R. McNelly, Chair,
Department of Mechanical Engineering

THIS PAGE INTENTIONALLY LEFT BLANK

ABSTRACT

A series of underwater and air explosion investigations was conducted using the Arbitrary Lagrangian-Eulerian (ALE) numerical technique. The investigation primarily examined the explosive-fluid, fluid-structure, and fluid-air interaction effects, and the shock wave pressure propagation through a subjected medium, with the intent of verifying and validating the ALE analysis. The research also noted the explosive-air and air-structure interaction effects as well as shock wave pressure propagation effects. Three-dimensional underwater explosion analyses was conducted using TNT detonations. Two-dimensional air explosion analyses were completed using TNT detonations. With viable ALE results, underwater and air explosion modeling and simulation could become dependable, cost-effective, and time-efficient.

THIS PAGE INTENTIONALLY LEFT BLANK

TABLE OF CONTENTS

I.	INTRODUCTION.....	1
	A. BACKGROUND	1
	B. SCOPE OF RESEARCH	2
II.	NUMERICAL ANALYSIS	5
	A. ARBITRARY LAGRANGIAN-EULERIAN (ALE) TECHNIQUE	5
	B. TIME INTEGRATION.....	6
	C. MATERIAL MODELS	7
	D. EQUATIONS OF STATE.....	9
	E. ADVECTION ALGORITHM.....	11
	F. COUPLING ALGORITHM.....	13
III.	THEORY.....	19
	A. UNDERWATER SHOCK PHENOMENA.....	19
	B. CAVITATION.....	23
	1. Local Cavitation	23
	2. Bulk Cavitation	27
IV.	UNDERWATER EXPLOSION.....	35
	A. MODEL CONSTRUCTION AND DIMENSIONS	36
	1. Explosive Model	36
	2. Fluid Model	39
	3. Air Model	40
	4. Structural Model.....	41
	B. ANALYSIS AND SOLUTION	41
	1. Analysis Code Description.....	41
	2. Test Description	42
	C. POST-PROCESSING	42
V.	AIR EXPLOSION.....	61
	A. MODEL CONSTRUCTION AND DIMENSIONS	61
	1. Explosive Model	61
	2. Air Model	62

3. Structural Model.....	62
B. ANALYSIS AND SOLUTION	63
1. Analysis Code Description.....	63
2. Test Description	63
C. POST-PROCESSING	64
VI. SHOCK SIMULATION RESULTS	71
A. UNDERWATER EXPLOSION	71
1. Rectangular Block Explosive Simulation	72
2. Stair Explosive Simulation.....	101
B. TWO-DIMENSIONAL AIR EXPLOSION	126
VII. CONCLUSIONS AND RECOMMENDATIONS.....	135
APPENDIX A. BULK CAVITATION PROGRAM.....	137
APPENDIX B. USEFUL TRUEGRID COMMANDS	141
APPENDIX C. TRUEGRID COMMANDS: UNDEX 3-D MODEL WITH BLOCK TNT EXPLOSIVE MODEL.....	143
APPENDIX D. TRUEGRID COMMANDS: UNDEX 3-D MODEL WITH STAIR TNT EXPLOSIVE MODEL.....	145
APPENDIX E. LS-DYNA INPUT DECK: UNDEX 3-D MODEL WITH BLOCK TNT EXPLOSIVE MODEL.....	149
APPENDIX F. LS-DYNA INPUT DECK: UNDEX 3-D MODEL WITH STAIR TNT EXPLOSIVE MODEL.....	153
APPENDIX G. USEFUL LS-DYNA COMMANDS.....	157
APPENDIX H. USEFUL LS-POST COMMANDS	159
APPENDIX I. TRUEGRID COMMANDS: 2-D AIR EXPLOSION	161
APPENDIX J. LS-DYNA INPUT DECK: 2-D AIR EXPLOSION WITH ONE-INCH THICK STEEL	163
APPENDIX K. LS-DYNA INPUT DECK: 2-D MINE AIR EXPLOSION WITH HALF-INCH THICK STEEL.....	167

APPENDIX L. LS-DYNA INPUT DECK: 2-D MINE AIR EXPLOSION WITH	
QUARTER-INCH THICK STEEL	171
LIST OF REFERENCES	175
INITIAL DISTRIBUTION LIST	179

THIS PAGE INTENTIONALLY LEFT BLANK

LIST OF FIGURES

Figure 1. Second Order Van Leer Algorithm [From Ref.13].....	15
Figure 2. Lagrangian/Eulerian Coupling [After Ref. 13].....	16
Figure 3. Penalty Coupling [From Ref. 13]	17
Figure 4. Gas Bubble and Shock Wave from an Underwater Explosion [From Ref. 19].	20
Figure 5. Shock Wave Profiles From a 300 lb. TNT Charge [From Ref. 18].....	20
Figure 6. Taylor Plate Subjected to a Plane Wave [From Ref. 19].....	24
Figure 7. Bulk Cavitation Zone [From Ref. 19].....	28
Figure 8. Charge Geometry for Bulk Cavitation Equations [From Ref. 19].....	31
Figure 9. Bulk Cavitation Zones for 60 lbf TNT Charge at Depth of 25 ft	32
Figure 10. Bulk Cavitation Zones for 60 lbf TNT Charge at Depth of 50 ft	33
Figure 11. Flow Chart Model Construction and Simulation.....	35
Figure 12. TNT Rectangular Block Explosive Model	44
Figure 13. Stair-Cased Explosive Model for TNT	45
Figure 14. Stair-Cased Explosive Model for TNT (Side View).....	46
Figure 15. Stair-Cased Explosive Model for TNT (Angle View).....	47
Figure 16. Fluid Mesh (Top View)	48
Figure 17. Fluid Mesh (Side View).....	49
Figure 18. Three-Dimensional Fluid Mesh	50
Figure 19. Three-Dimensional Fluid Mesh Parameters (Top View).....	51
Figure 20. Air Model (Top View)	52
Figure 21. Air Model (Side View)	53
Figure 22. Three-Dimensional Air Mesh	54
Figure 23. Three-Dimensional Air Mesh Parameters	55
Figure 24. Three-Dimensional Barge.....	56
Figure 25. Three-Dimensional Barge (Bulkheads)	57
Figure 26. Three-Dimensional Barge with Lumped Mass Locations (Top View)	58
Figure 27. Offset Charge Test Geometry	59
Figure 28. Bulk Cavitation Zones for 60-lbf TNT Charge at 24 ft	60
Figure 29. Three-Dimensional Barge with Lumped Mass Locations	65

Figure 30. Explosive Model (Top View)	66
Figure 31. Air Model (Top View)	67
Figure 32. Air Model (Angle View).....	68
Figure 33. Steel Shell Plating	69
Figure 34. TNT Explosive and Steel Shell Plating	70
Figure 35. Barge Nodes in Rectangular Box Charge Case	77
Figure 36. Barge Nodes in Stair Charge Case	78
Figure 37. Fluid Nodes in Rectangular Box Charge Case	79
Figure 38. Fluid Nodes in Stair Charge Case	80
Figure 39. Fluid Element 1128 Pressure Profile	81
Figure 40. Fluid Element 1139 Pressure Profile	82
Figure 41. Fluid Element 46247 Pressure Profile	83
Figure 42. Fluid Element 46256 Pressure Profile	84
Figure 43. Fluid Element 46264 Pressure Profile	85
Figure 44. Fluid Element 67155 Pressure Profile	86
Figure 45. Fluid Element 69178 Pressure Profile	87
Figure 46. Fluid Element 79616 Pressure Profile	88
Figure 47. Fluid Element 79786 Pressure Profile	89
Figure 48. Fluid Element 89068 Pressure Profile	90
Figure 49. Fluid Element 25576 Pressure Profile	91
Figure 50. Fluid Element 43680 Pressure Profile	92
Figure 51. Fluid Element 46087 Pressure Profile	93
Figure 52. Fluid Element 47694 Pressure Profile	94
Figure 53. Fluid Element 47706 Pressure Profile	95
Figure 54. Fluid Element 46968 Pressure Profile	96
Figure 55. Velocity Response at Nodes 124024/16862	97
Figure 56. Velocity Response at Nodes 124134/39870	98
Figure 57. Velocity Response at Nodes 124173/39868	99
Figure 58. Velocity Response at Nodes 124190/40492	100
Figure 59. Fluid Element 3277 Pressure Profile	106

Figure 60. Fluid Element 3290 Pressure Profile	107
Figure 61. Fluid Element 73350 Pressure Profile	108
Figure 62. Fluid Element 73360 Pressure Profile	109
Figure 63. Fluid Element 73370 Pressure Profile	110
Figure 64. Fluid Element 105852 Pressure Profile	111
Figure 65. Fluid Element 112932 Pressure Profile	112
Figure 66. Fluid Element 126792 Pressure Profile	113
Figure 67. Fluid Element 127012 Pressure Profile	114
Figure 68. Fluid Element 141092 Pressure Profile	115
Figure 69. Fluid Element 40981 Pressure Profile	116
Figure 70. Fluid Element 40993 Pressure Profile	117
Figure 71. Fluid Element 75223 Pressure Profile	118
Figure 72. Fluid Element 75245 Pressure Profile	119
Figure 73. Fluid Element 75261 Pressure Profile	120
Figure 74. Fluid Element 74296 Pressure Profile	121
Figure 75. Velocity Response at Nodes 195467/62654	122
Figure 76. Velocity Response at Nodes 195450/61950	123
Figure 77. Velocity Response at Nodes 195304/26928	124
Figure 78. Velocity Response at Nodes 195411/61952	125
Figure 79. Air Pressure Signatures at Radius = 2.09 ft	127
Figure 80. Air Pressure Signatures at Radius = 3.60 ft	128
Figure 81. Air Pressure Signatures at Radius = 6.73 ft	129
Figure 82. Air Velocity at Radius = 2.09 ft	130
Figure 83. Air Velocity at Radius = 3.60 ft	131
Figure 84. Air Velocity at Radius = 6.73 ft	132
Figure 85. Structural Particle Velocities	133

THIS PAGE INTENTIONALLY LEFT BLANK

LIST OF TABLES

Table 1. TNT Charge Modeling Characteristics	38
Table 2. TNT Charge Characteristics (Ref. 17)	38
Table 3. TNT Equation of State Parameters (Ref. 17)	38
Table 4. Material Property Characteristics.....	63
Table 5. Rectangular Block Case Results: Nodes Along X-Y Plane	74
Table 6. Rectangular Block Case Results: Nodes Along NRB 1	75
Table 7. Rectangular Block Case Results: Nodes Along NRB 2.....	76
Table 8. Stair Case Results: Nodes Along X-Y Plane	103
Table 9. Stair Case Results: Nodes Along NRB 1	104
Table 10. Stair Case Results: Nodes Along NRB 2	105

THIS PAGE INTENTIONALLY LEFT BLANK

ACKNOWLEDGEMENTS

I take extreme pleasure in thanking Professor Young S. Shin for his keen guidance, extreme patience, and greatest support throughout this research. Additionally, Dr. Robert Rainsberger, Dr. M'hamed Souli, and Dr. Lars Olovsson deserve much recognition for their technical expertise and support to this research. Furthermore, I would also extend a great thanks to Tom Christian for his computer technical support.

Finally, I dedicate this research to my loving wife Chanida and beautiful daughters Vanisha and Olivia for their love, support, and understanding during our time at the Naval Postgraduate School.

I. INTRODUCTION

A. BACKGROUND

Air and underwater explosion blast waves have been of great interest to the military. An explosion created by a mine produces a pressure pulse or shock wave. When a shock wave impacts a structural surface, the shock wave can cause severe negative structural and equipment damage, as well as personnel casualties. As a result, military hardware must be shock hardened to ensure combat survivability to both personnel and equipment. NAVSEA 0908-LP-000-3010A [Ref. 1] and MIL-S-901D [Ref. 2] provide the Navy with guidelines and specifications for shock testing and hardening of shipboard equipment. OPNAVINST 9072.2 [Ref. 3] requires a total ship system design validation through a series of shock trials. Shock trials are performed on the lead ship of a new class of surface ship in order to correct design deficiencies early.

Unfortunately, shock trials also need extensive planning and coordination. For example, planning shock trials for USS Jon Paul Jones (DDG-53) started four years prior to the test date. Furthermore, an environmental lawsuit delayed shock trials by three months. Shock trials happened in June 1994, but only two of the four planned tests could be accomplished due to inclement weather, ship's post trial delivery date, and deployment preparations [Ref. 4].

Live Fire Test and Evaluation (LFT&E) assesses a system's vulnerabilities under realistic combat conditions. LFT&E's objectives are to correct design deficiencies and reduce personnel casualties. LFT&E can be expensive due to the destruction and/or damage to the ship's structure and equipment after a shock trial [Ref. 5]. Furthermore, realistic testing is often sacrificed because of environmental constraints. Thus, realistic combat testing of military systems is highly impractical [Ref. 6]. Modeling and simulation offers a potential advantage for studying structural failure responses and weapons effects under simulated combat test conditions [Ref. 6].

Furthermore, land mines represent a serious threat to personnel and motor vehicles. Designing a vehicle to withstand the small mine effects is equally important.

The value of such a vehicular design can clear lanes through a scatterable minefield. But, the need to understand the air blast wave propagation and the resulting mine solid particle dynamics is paramount to the vehicular design. Modeling and simulation of the air blast wave and the effects of the mine fragmentation can offer such a perspective.

With recent computer hardware technology advances and increased research in numerical simulation of partial differential equations, finite element modeling and simulation provides a viable, cost effective alternative to live fire testing under realistic combat conditions. Using commercial software packages such as *TrueGrid*[®] [Ref. 7] and LS-DYNA [Ref. 8] have enabled researchers to produce detailed finite element models in a timely manner. "Sufficient fidelity" mesh modeling is required to produce acceptable results [Ref. 9].

Hydrocodes are defined as tools for the simulation of multi-material, compressible, transient continuum mechanics (i.e. mechanical wave propagation through multiple fluids and solids) [Ref. 10]. Hydrocodes for mesh descriptions categorically fall into two basic arenas: Lagrangian and Eulerian. Each has its distinct advantages and disadvantages. Over the past few years, various hybrid hydrocode schemes have been developed to handle both Lagrangian and Eulerian. The Arbitrary Lagrangian-Eulerian (ALE) numerical formulation was mainly incorporated to study the mitigation effects of the explosive-water, explosive-air and structure-fluid/air medium interaction.

B. SCOPE OF RESEARCH

This paper investigates the Arbitrary Lagrangian-Eulerian (ALE) formulation technique using LS-DYNA in both underwater and air explosion computer modeling and simulations. For the underwater explosion (UNDEX) computer simulation modeling, the thesis explores the explosive charge modeling effects in shock wave propagation in the fluid medium models and the structural response of the structural finite element models. Based on the numerical feasibility or confidence of the UNDEX simulation, the thesis will then explore the air explosion (AIREX) simulation modeling. The AIREX scenarios will investigate the air blast wave propagation and the effects of the blast wave

propagation on a varying cylindrical surface thickness. As an overview, Chapter II will discuss the important features of the numerical analysis code used in the ALE formulation. Chapter III will cover underwater shock principles. Chapters IV will describe the modeling setup for the UNDEX scenarios. After gaining numerical confidence in the ALE technique, Chapter V will describe the AIREX model setups. And, Chapter VI will discuss the results obtained from the conducted simulations.

THIS PAGE INTENTIONALLY LEFT BLANK

II. NUMERICAL ANALYSIS

A. ARBITRARY LAGRANGIAN-EULERIAN (ALE) TECHNIQUE

Explosions involve liquid and gas flow, as well as high-pressure shock waves. A Lagrangian finite element mesh in the explosive charge region is not always feasible. The surrounding fluid medium elements around the explosive charge deform severely in Lagrangian based meshes. Consequently, the time step size per iteration becomes extremely small resulting in large computational time [Ref. 11]. Furthermore, numerical approximation inaccuracies can exist due to mesh distortions [Ref. 12].

Eulerian based finite element modeling advance solutions in time on a fixed mesh using Navier-Stokes equations. When the solutions are progressed on a fixed mesh, the Eulerian hydrocodes avoid mesh distortions as presented in the Lagrangian hydrocodes. Additionally, algorithms have been developed to prevent the diffusion between two material types at a higher computational expense. Furthermore, solving the Navier-Stokes equations (Eulerian) are generally more expensive computationally and complicated than the Lagrangian formulation [Ref. 13]. As a result, a hybrid numerical formulation technique has been developed which tries to utilize the advantages of both the Eulerian and Lagrangian schemes.

The numerical analysis processor conducted in this study utilizes an ALE finite element code. LS-DYNA [Ref. 8] was used for the numerical analysis during this investigation. ALE hydrocodes utilize both Lagrangian and Eulerian hydrocodes that perform automatic rezoning [Ref. 14]. An ALE hydrocode involves a Lagrangian time step followed by a remap or advection phase. The advection phase may pursue one of three avenues in which the spatial mesh is (a) not rezoned due to reasonable mesh deformation (Lagrangian), (b) rezoned to its original shape due to severe mesh deformation (Eulerian), or (c) rezoned to a more suitable form (Lagrangian and Eulerian) thus allowing the topology of mesh to remain fixed [Refs. 10 and 14]. It provides suitable material models and essential equations of state (EOS) for underwater and air explosions. Furthermore, the code provides advection and coupling algorithms in the ALE method in order to provide accurate, stable, conservative, and monotonic results.

Mass, momentum, and energy transport is systematically computed for all elements in the model. Each element's density, velocity, and energy will be updated. Pressure in each element is computed using the updated density and specific internal energies in the model's EOS.

B. TIME INTEGRATION

The processor uses the central difference method to advance the mesh position in time [Refs. 13 and 14]. The Eulerian time step (Δt) requires stability and is a function of the element's characteristic length (Δx), material's speed of sound (c) and particle velocity (u) such that

$$\Delta t < \frac{\Delta x}{c + u} \quad (2.1)$$

The displacement (x) and velocity (u) vectors are staggered in time to provide a second order accurate scheme in time for an "n" iteration step.

$$x^{n+1} = x^n + u^{n+1/2} \Delta t^n \quad (2.2)$$

$$u^{n+1/2} = u^{n-1/2} + \frac{1}{2} a^n (\Delta t^n + \Delta t^{n+1}) \quad (2.3)$$

where acceleration vector (a^n) is $\frac{F^n}{M}$. The total nodal force vector and diagonal mass matrix are represented by F^n and M , respectively. Substituting the acceleration term into Equation (2.3) yields:

$$u^{n+1/2} = u^{n-1/2} + \frac{F^n}{2M} (\Delta t^n + \Delta t^{n+1}) \quad (2.4)$$

The total nodal force vector consists of an internal nodal force vector (F_{int}^n) and an external nodal force vector (F_{ext}^n) such that

$$F^n = F_{int}^n + F_{ext}^n \quad (2.5)$$

The internal nodal force is a function of the stress (σ^n) where the stress includes the deviatoric sum of the equation of state pressure ($-P^n I_d$) and material strength (σ_d^n) vectors such that

$$F_{int}^n = \int_V B^t \sigma^n dx \quad (2.6)$$

$$\sigma^n = -P^n I_d + \sigma_d^n \quad (2.7)$$

where B^t is the strain-displacement matrix, and I_d is a principal strain invariant. The external nodal force vector (F_{ext}^n) consists of the body forces, boundary forces, non-reflecting boundary conditions, and contact forces [Refs. 13 and 14].

C. MATERIAL MODELS

This research involves several types of material models. The models incorporated the following material models: (a) plastic kinematic/isotropic, (b) null material, and (c) high explosive burn.

The plastic kinematic/isotropic model is used for modeling composites, metals, and plastics. This material type effectively measures strain-rate and failure effects and is used in beam, shell and solid element modeling [Refs. 8 and 14]. The plastic kinematic/isotropic material type is used in modeling the structural metals.

For the air and water modeling, equations of state (EOS) are employed with the null material type. The material strength in the null material element is ignored when the

model is combined with a high explosive material type. The null material type is effective in modeling fluids and hydrodynamic medium. Additionally, this material type can measure failure and thermal effects [Refs. 8 and 14]. The solid element deformation is due to a displacement gradient or strain (ϵ). The fluid element deformation is due to a velocity gradient or strain rate ($\dot{\epsilon}$). For fluid elements, the deviatoric shear stress (σ_d) is proportional to the shear strain rate ($\dot{\epsilon}$) such that

$$\sigma_d = 2\mu\dot{\epsilon} \quad (2.8)$$

where μ is the fluid viscosity. When a fluid experiences shear stress, the fluid deforms as long as a shear stress is applied [Ref. 13]. Hence, air and water are modeled as null materials.

In the high explosive burn model material type, an EOS is used. In this material type, burn fractions, F , direct a chemical energy release for detonation simulations. The burn fraction is taken as the maximum:

$$F = \max(F_1, F_2) \quad (2.9)$$

where F_1 is a function of density, ρ , the explosive detonation velocity, D , ratio of volumetric compression, $\frac{v}{v_0}$, and the Chapman-Jouget pressure, P_{cj} such that

$$F_1 = \frac{\rho D^2}{P_{cj}} \left(1 - \frac{v}{v_0} \right) \quad (2.10)$$

and F_2 is a function of the detonation velocity, D , burn time, t_b , current time, t , and characteristic length of element, Δx .

$$F_2 = \frac{2(t - t_b)D}{3\Delta x} \quad (2.11)$$

If the burn fraction, F , exceeds unity, F is reset to one and is held constant [Refs. 8, 13, and 14]. The high explosive pressure, P , in an element is scaled by the burn fraction, F , such that:

$$P = F \cdot P_{\text{eos}}(V, E) \quad (2.12)$$

where P_{eos} is the pressure from an EOS based on the relative volume, V , and internal energy density per unit initial volume, E [Ref. 14]. Thus, TNT is modeled using a high explosive burn material model type.

D. EQUATIONS OF STATE (EOS)

An equation relating the pressure, temperature, and specific volume of a substance is known as an EOS. Property relations involving other properties of a substance at equilibrium states are also known as an equation of state [Ref. 15]. This investigation utilized three different EOS in the modeling and simulation. The EOS involved were the linear polynomial, Gruneisen, and Jones, Wilkins, and Lee (JWL) equations.

Air is modeled using the linear polynomial EOS. The linear polynomial EOS is linear in internal energy per unit initial volume, E . The pressure is given by

$$P = C_0 + C_1\mu + C_2\mu^2 + C_3\mu^3 + (C_4 + C_5\mu + C_6\mu^2)E \quad (2.13)$$

where C_0 , C_1 , C_2 , C_3 , C_4 , C_5 , and C_6 are constants and

$$\mu = \frac{1}{V} - 1 \quad (2.14)$$

where V is the relative volume [Ref. 14].

The Gruneisen EOS is used to model the seawater. The Gruneisen EOS incorporates a cubic shock velocity-particle velocity, which defines the pressure for a compressed material as

$$P = \frac{\rho_0 C^2 \mu \left[1 + \left(1 - \frac{\gamma_0}{2} \right) \mu - \frac{a}{2} \mu^2 \right]}{\left[1 - (S_1 - 1) \mu - S_2 \frac{\mu^2}{\mu + 1} - S_3 \frac{\mu^3}{(\mu + 1)^2} \right]} + (\gamma_0 + a\mu)E \quad (2.15)$$

where C is the intercept constant of the shock wave velocity (u_s)-particle velocity (u_p) curve, γ_0 is the Gruneisen gamma, "a" is the first order volume correction to γ_0 , and S_1 , S_2 , and S_3 are slope coefficients of the u_s - u_p curve [Ref. 14]. Compression is defined using the relative volume, V , as:

$$\mu = \frac{1}{V} - 1 \quad (2.16)$$

The particle velocity (u_p) is related to the shock wave velocity (u_s) [Refs. 13 and 14] through

$$u_s = C + S_1 u_p + S_2 \left(\frac{u_p}{u_s} \right)^2 u_p + S_3 \left(\frac{u_p}{u_s} \right)^3 u_p \quad (2.17)$$

For TNT, a JWL EOS is used. The JWL EOS defines the pressure as a function of the relative volume, V , and initial energy per initial volume, E , such that

$$P = A \left(1 - \frac{\omega}{R_1 V} \right) e^{-R_1 V} + B \left(1 - \frac{\omega}{R_2 V} \right) e^{-R_2 V} + \frac{\omega E}{V} \quad (2.18)$$

The parameters ω , A , B , R_1 , and R_2 are constants pertaining to the explosive. This EOS is well suited because it determines the explosive's detonation pressure in applications involving structural metal accelerations [Ref. 17].

E. ADVECTION ALGORITHM

A good advection (remap) step involves accuracy, stability, conservation, and monotonicity [Ref. 14]. A monotonic, second order accurate "Van-Leer and Half-Shift Index" advection scheme is used for material transport. In mass advection, a new Eulerian density for each element is solved using the following scheme [Ref. 13]:

$$\rho_e V_e = \rho_L V_L + \sum_{\text{faces}} \rho_L^j \phi_j \quad (2.19)$$

where

- ρ_e - Eulerian element density
- V_e - Eulerian element volume
- ρ_L - Lagrangian element density
- V_L - Lagrangian element volume
- ρ_L^j - Density of adjacent Lagrangian element j
- ϕ_j - Volume flux through adjacent element j

Internal energy advection is expressed in terms of a variable, s , where

$$s = \frac{E}{V} \quad (2.20)$$

Or, mass advection can be expressed in terms of a variable, s , such that,

$$s = \rho \quad (2.21)$$

Thus, equation (2.19) is now written as a general advection equation of $s_e V_e$ where

$$s_e V_e = s_L V_L + \sum_{\text{faces}} s_L^j \phi_j \quad (2.22)$$

In a one-dimensional coordinate system, the change in momentum in the x -direction can be solved in terms of the u -velocity. The Lagrangian element u -velocity (u_L^{elem}) can be expressed as

$$u_L^{\text{elem}} = \frac{1}{8} \sum_{j=1}^8 u_L^j \quad (2.23)$$

Using the velocity result from Equation 2.23, the variable x -momentum (s_L^{elem}) is

$$s_L^{\text{elem}} = \rho_L^{\text{elem}} \cdot u_L^{\text{elem}} \quad (2.24)$$

The updated or new element centered x -momentum flux becomes

$$s_e V_e = s_L V_L + \Delta M_x \quad (2.25)$$

where ΔM_x is defined as the change in x -momentum resulting from advection:

$$\Delta M_x = \sum_{j=1}^{\text{faces}} s_L^j \phi_j \quad (2.26)$$

A similar analysis is applied to Equations (2.19) through (2.26) when dealing with a three-dimensional model.

Using the analysis in Equations (2.23) – (2.26) yields a first order accurate scheme. The Van-Leer scheme yields a second order accurate advection scheme where the variable, s_L^{elem} , is modified (Figure 1). Instead of using Equation (2.24), the Van-Leer scheme utilizes Equation (2.27) to calculate s_L^{elem} :

$$s_L^{\text{elem}} = \rho_0 + \frac{1}{2}(x_1 - x_0) \frac{\partial \rho}{\partial x}(x_1) \quad (2.27)$$

F. COUPLING ALGORITHM

In Figure 2, the structure-medium coupling interface designates a structural surface, typically shell elements, as a "slave" material and the fluid as a "master" material [Refs. 13 and 14]. This model uses a "penalty coupling" factor in the Lagrangian-Eulerian coupling. No special pre-processing manipulation of the intersecting surfaces between the master and slave materials is required.

The penalty coupling factor tracks the relative displacement (d) between a Lagrangian node (structure i.e. slave material) and the Eulerian fluid (master) material location (Figure 3). Each slave node is checked for penetration through the master surface. If no slave node penetration occurs, nothing is done. If slave node penetration into the master surface occurs, an interface force (F) is distributed to the Eulerian fluid nodes. The interface force's magnitude is proportional to the amount of penetration occurring such that:

$$F = k_i \cdot d \quad (2.28)$$

where k_i is a stiffness factor based on the master and slave nodes mass model properties.

As the interface force (F) in Equation (2.28) is solved for each time integration, F is considered as one of the external body forces in Equation (2.5). Thus, a total nodal force (F^n) can be solved in each time integration resulting in structural accelerations, velocities, and displacements.

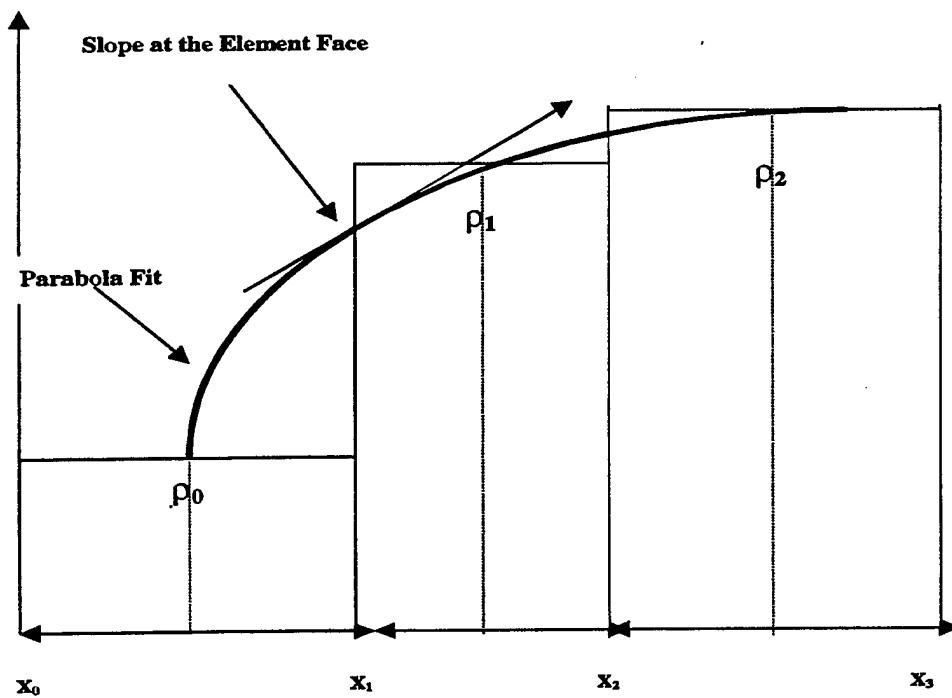


Figure 1. Second Order Van Leer Algorithm (From Ref. 13)

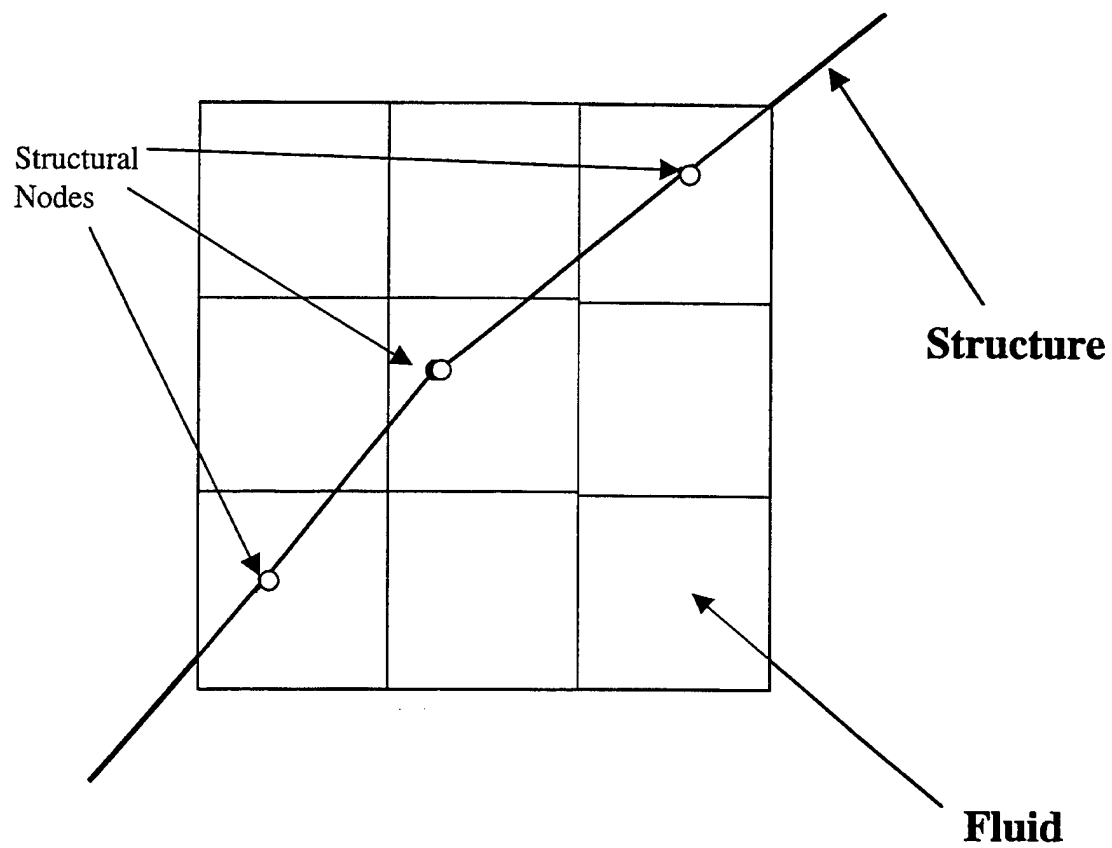


Figure 2. Lagrangian/Eulerian Coupling (After Ref. 13)

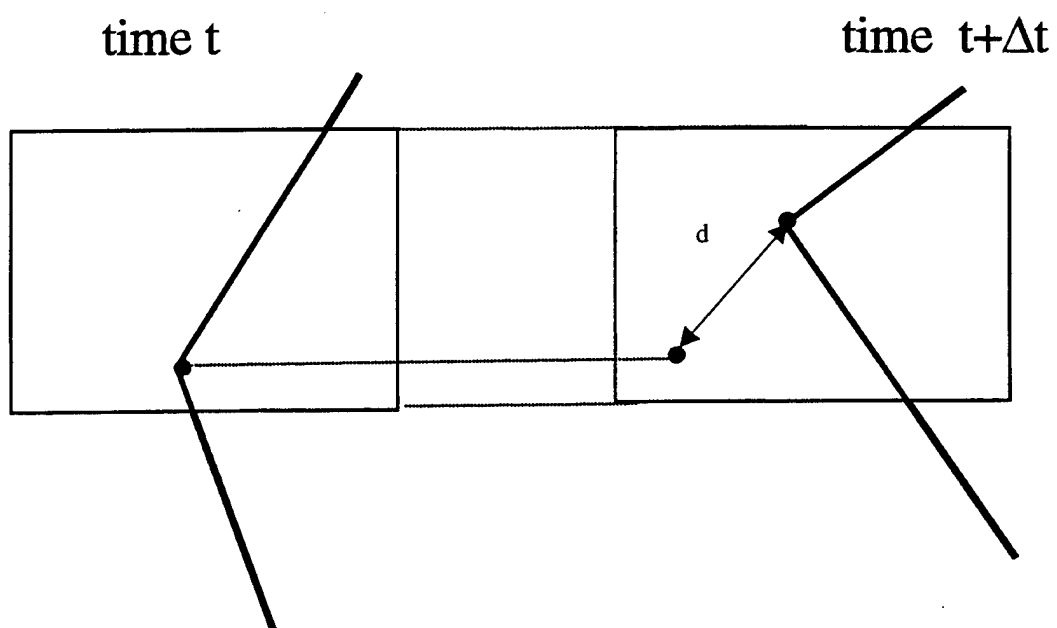


Figure 3. Penalty Coupling (From Ref. 13)

THIS PAGE INTENTIONALLY LEFT BLANK

III. THEORY

A. UNDERWATER SHOCK PHENOMENA

An underwater explosion is a complex sequence of events. The explosion starts with a high explosive detonation. The explosion consists of a chemical reaction in an initial unstable substance. The initial chemical reaction converts the unstable material into a stable gas at a very high temperature and pressure (on the order of 3000°C and 50000 atm.) [Ref. 18]. As the initial pressure wave within the explosive disseminates, additional chemical reactions follow thus creating additional pressure waves. The pressure wave velocity steadily increases within the explosive until velocity exceeds the speed of sound in the explosive. Consequently, the explosive produces a shock wave. The combination of high temperature and pressure describes the detonation as a self-exerting process where the temperature and pressure profiles exist behind the shock wave. The high temperature and pressure gas expands in an outward motion into the surrounding fluid medium [Ref. 19].

The high-pressure disturbance traveling outward radially at the speed of sound is referred to as the shock wave. As the shock wave expands outward, the explosion also induces an outward velocity to the surrounding fluid medium as described in Figure 4. The initial high-pressure is greater than the opposing atmospheric and hydrostatic pressure. Thus, the initial pressure is compressive in nature. At detonation, the pressure rise produces a steep fronted discontinuous wave decaying exponentially with respect to time as shown in Figure 5. The pressure disturbance lasts only a few milliseconds. Although the shock wave character near the explosive charge is unknown, the shock wave propagates roughly at several (3~5) times the speed of sound in water, approximately $5,000\text{ ft/sec}$, which then falls rapidly to acoustic velocity as it travels outward in the water [Ref. 18].

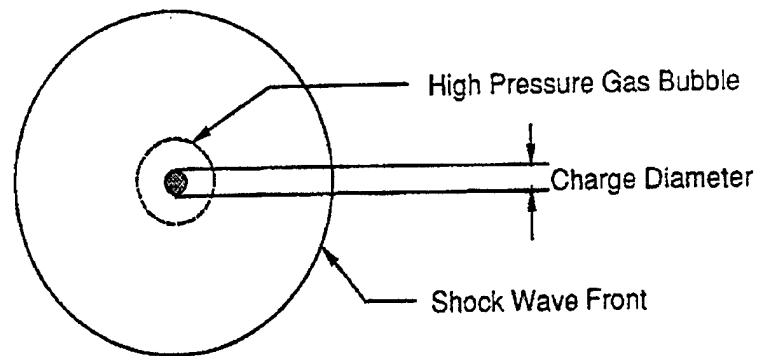


Figure 4. Gas Bubble and Shock Wave from an Underwater Explosion

[From Ref. 19]

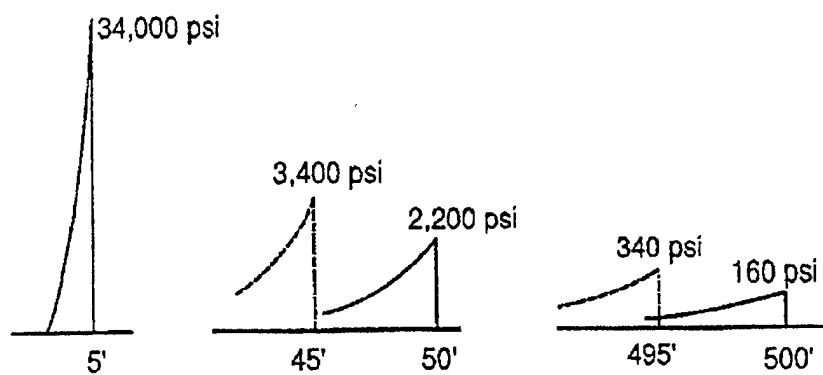


Figure 5. Shock Wave Profiles From a 300 lb. TNT Charge [From Ref. 18]

Furthermore, the shock wave pressure is proportional to the inverse of the distance from the charge to the target, $1/d$. Additionally, the shock wave profile gradually broadens as it spreads out [Ref. 18]. Empirical equations have been formulated to describe the shock wave profile. These relations calculate of the shock wave pressure profile, $P(t)$, the maximum shock front pressure, P_{\max} , the shock wave decay constant θ , the gas bubble period (T), and the maximum gas bubble radius (A_{\max}).

$$P(t) = P_{\max} e^{\frac{-(t-t_1)}{\theta}} \quad (\text{psi}); \quad t \geq t_1 \quad (3.1)$$

$$P_{\max} = K_1 \left(\frac{\frac{1}{W^3}}{R} \right)^{A_1} \quad (\text{psi}) \quad (3.2)$$

$$\theta = K_2 W^{\frac{1}{3}} \left(\frac{\frac{1}{W^3}}{R} \right)^{A_2} \quad (\text{msec}) \quad (3.3)$$

$$T = K_5 \frac{\frac{1}{W^3}}{\frac{5}{(D+33)^{\frac{1}{6}}}} \quad (\text{sec}) \quad (3.4)$$

$$A_{\max} = K_6 \frac{W^{\frac{1}{3}}}{(D + 33)^{\frac{1}{3}}} \quad (\text{ft}) \quad (3.5)$$

where:

W = Charge weight (lbf)

R = Standoff distance (ft)

D = Charge depth (ft)

t₁ = arrival time of shock wave (msec)

t = time of interest (msec)

K₁, K₂, K₅, K₆, A₁, A₂ = Explosive Shock wave parameters

Equation (3.1) is good only for pressures greater than one third of P_{max} (Equation 3.2). Through calculation, it can be determined that P_{max} decreases by approximately one-third after one decay constant (θ).

In the underwater explosion process, the gas bubble oscillation produces subsequent pressure waves or bubble pulses. The peak pressure of the first bubble pulse is approximately 10-20% of the shock wave, but is of greater duration making the area under both pressure curves similar [Ref. 19]. The bubble expands until dynamic equilibrium is reached. The bubble then contracts until dynamic equilibrium is again reached, followed by another expansion. This oscillation sequence continues until the energy of the reaction is dissipated or the bubble reaches the free surface or impacts the target.

Depending on the charge location relative to the surface and the bottom, other issues have an effect on underwater shock. Bottom reflection waves involve bouncing shock wave off the sea bottom. Bottom reflection waves are considered compressive waves in nature. Refraction waves encompass shock waves traveling through the sea

bottom before emerging again in the water. Refraction waves are also considered compressive waves. In deep water, these two phenomena are not usually an issue for surface vessels.

Free surface reflection is a very important effect, however. Reflection or rarefaction waves are tensile, as opposed to the other compressive wave effects. Rarefaction waves are produced from the shock wave reflecting from the free surface. Consequently, rarefaction waves contribute to the bulk cavitation phenomenon.

B. CAVITATION

During an UNDEX, two types of cavitation can occur, namely local and bulk cavitation. Local cavitation occurs at the fluid-structure interface, while bulk cavitation occurs near the free surface and covers a relatively large area.

1. Local Cavitation

Taylor flat plate theory, the simplest case of fluid-structure interaction, depicts how local cavitation occurs. In this case, an infinite, air-backed plate is acted upon by an incident plane shock wave as shown in Figure 6.

Once the shock wave strikes the plate, a reflected shock wave leaves the plate. Using Newton's second law of motion for the equation of motion yield:

$$m \frac{du}{dt} = P_1 + P_2 \quad (3.6)$$

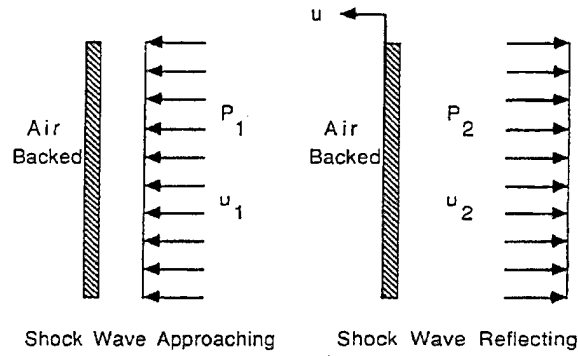


Figure 6. Taylor Plate Subjected to a Plane Wave [From Ref. 19]

where m is the plate mass per unit area, u is the plate velocity after being subjected to the shock wave, $P_1(t)$ is the incident wave pressure and $P_2(t)$ is the reflected, or scattered, wave pressure. The fluid particle's velocities behind the incident and reflected shock waves are defined as $u_1(t)$ and $u_2(t)$. The plate velocity, $u(t)$, is defined by Equation (3.7),

$$u(t) = u_1(t) - u_2(t) \quad (3.7)$$

For the one dimensional plane wave, the wave equation is $P = \rho c u$. The incident and reflected shock wave pressures are shown in Equations (3.8) and (3.9) respectively:

$$P_1 = \rho c u_1 \quad (3.8)$$

$$P_2 = \rho c u_2 \quad (3.9)$$

where ρ is the fluid density and c is water's acoustic velocity. Substituting Equations (3.8) and (3.9) into the plate velocity Equation (3.7) yields:

$$u = \frac{P_1 - P_2}{\rho c} \quad (3.10)$$

Using Equation (3.1), the incident shock wave pressure, $P_1(t)$, now becomes:

$$P_1(t) = P_{\max} e^{\frac{-t}{\theta}} \quad (3.11)$$

where time, t , is measured after the shock wave arrives at the target. Using Equation (3.10), the reflected shock pressure, $P_2(t)$, gives:

$$P_2 = P_1 - \rho c u \quad (3.12)$$

$$P_2 = P_{\max} e^{\frac{-t}{\theta}} - \rho c u \quad (3.13)$$

Combining the equation of motion, Equation (3.6), with Equations (3.11) and (3.13):

$$m \frac{du}{dt} + \rho c u = 2P_1 \quad (3.14)$$

$$m \frac{du}{dt} + \rho c u = 2P_{\max} e^{\frac{-t}{\theta}} \quad (3.15)$$

where Equation (3.15) is a first order, linear differential equation. Solving the differential equation in Equation (3.15) produces a solution, $u(t)$:

$$u = \frac{2P_{\max}\theta}{m(1-\beta)} \left[e^{\left(\frac{-\beta t}{\theta}\right)} - e^{\left(\frac{-t}{\theta}\right)} \right] \quad (3.16)$$

with $\beta = \rho C\theta/m$ and $t > 0$. The total pressure that impinges on the plate is defined as:

$$P_1 + P_2 = P_{\max} \left[\frac{2}{1-\beta} e^{\frac{-t}{\theta}} - \frac{2\beta}{1-\beta} e^{\frac{-\beta t}{\theta}} \right] \quad (3.17)$$

As the value of β becomes larger, as in the case of a lightweight plate, the total pressure will become negative at a very early time. However, since water cannot support tension, negative pressure cannot exist. Therefore, as the water pressure reduces to vapor pressure at the surface of the plate, local cavitation occurs. At this point, the pressure in front of the plate has been cut off and the plate has reached its maximum velocity [Ref. 19].

A ship's hull can be easily generalized as a Taylor flat plate. Local cavitation is likely to occur along the hull where the pressure pulse from the UNDEX impinges with sufficient force and the hull plating β value is large enough to make the net pressure negative.

2. Bulk Cavitation

As discussed previously, the incident shock wave is compressive in nature. A rarefaction wave (tensile wave) is created when the shock wave is reflected from the free surface. Since water cannot sustain a significant amount of tension, cavitation occurs when the fluid pressure drops to zero or below. Upon cavitation, the water pressure rises to the vapor pressure of water, approximately 0.3 psi. This cavitated area produced by the rarefaction wave is known as the bulk cavitation zone. The bulk cavitation region contains an upper and lower boundary. The bulk cavitation zone relies on the charge size, type, and depth [Refs. 20 - 22].

Figure 7 shows a typical bulk cavitation zone. The cavitation zone is symmetric about the y-axis in the figure; typically only one-half is shown due to the symmetry about the y-axis. At the time of cavitation, the water particles' velocities behind the shock wave front depend on their location relative to the charge and the free surface. For example, the water particles' velocities near the free surface will have a primarily vertical velocity at cavitation. As the reflected wave passes, gravity and atmospheric pressure will primarily act on the water particles' velocities.

The upper cavitation boundary consists of a set of points where the rarefaction wave passes and reduces the absolute pressure to zero or a negative value. This region will remain cavitated as long as the pressure remains below the vapor pressure. The total or absolute pressure, which determines the upper boundary, is composed of atmospheric pressure, hydrostatic pressure, incident shock wave pressure, and rarefaction wave pressure.

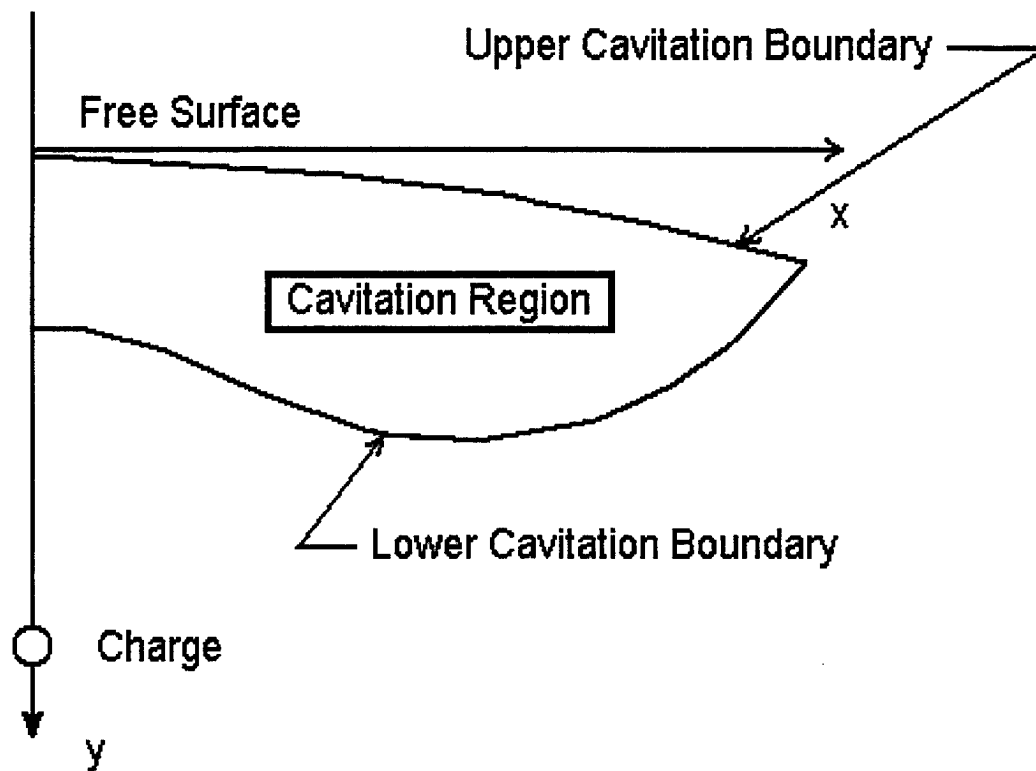


Figure 7. Bulk Cavitation Zone [From Ref. 19]

The lower cavitation boundary is determined by equating the decay rate of the breaking pressure to the decay rate of the total absolute pressure. The breaking pressure is the rarefaction wave pressure that reduces a particular location of a fluid to the point of cavitation pressure, or zero psi.

The upper and lower cavitation boundaries are calculated using Equations (3.18) and (3.19), respectively [Ref. 21]. Any point which satisfies $F(x,y)$ and $G(x,y) = 0$ determines the bulk cavitation boundary.

$$F(x,y) = K_1 \left(\frac{1}{\frac{W^3}{r_1}} \right)^{A_1} e^{-\frac{(r_2 - r_1)}{c\theta}} + P_A + \gamma - K_1 \left(\frac{1}{\frac{W^3}{r_2}} \right)^{A_1} \quad (3.18)$$

$$G(x,y) = -\frac{P_i}{C\theta} \left\{ 1 + \left[\frac{r_2 - 2D \left(\frac{D+y}{r_2} \right)}{r_1} \right] \left[\frac{A_2 r_2}{r_1} - A_2 - 1 \right] \right\} - \frac{A_1 P_i}{r_1^2} \left[r_2 - 2D \left(\frac{D+y}{r_2} \right) \right] + \gamma \left(\frac{D+y}{r_2} \right) + \frac{A_1}{r_2} (P_i + P_a + \gamma) \quad (3.19)$$

where

$$P_i = K_1 \left(\frac{1}{\frac{W^3}{R}} \right)^{A_1} e^{-\frac{(r_2 - r_1)}{c\theta}} \quad (3.20)$$

The variables in Equations (3.18) and (3.19) are:

- x, y = horizontal range and vertical depth of the point
- r_1 = standoff distance from the charge to the point
- r_2 = standoff distance from the image charge to the point
- c = acoustic velocity in the water
- D = charge depth
- θ = decay constant
- γ = weight density of water
- P_A = atmospheric pressure
- W = charge weight
- θ = decay constant
- K_1, A_1 = shock wave parameters

Figure 8 shows the charge geometry for Equation (3.18) and (3.19).

Appendix A provides a MATLAB m-file [Ref. 23] calculating and plotting the bulk cavitation zone for a user supplied charge weight (HBX-1 and TNT) and depth by solving Equations (3.18) and (3.19). Figures 9 and 10 provide an example of bulk cavitation curves generated using the program for two different charge depths.

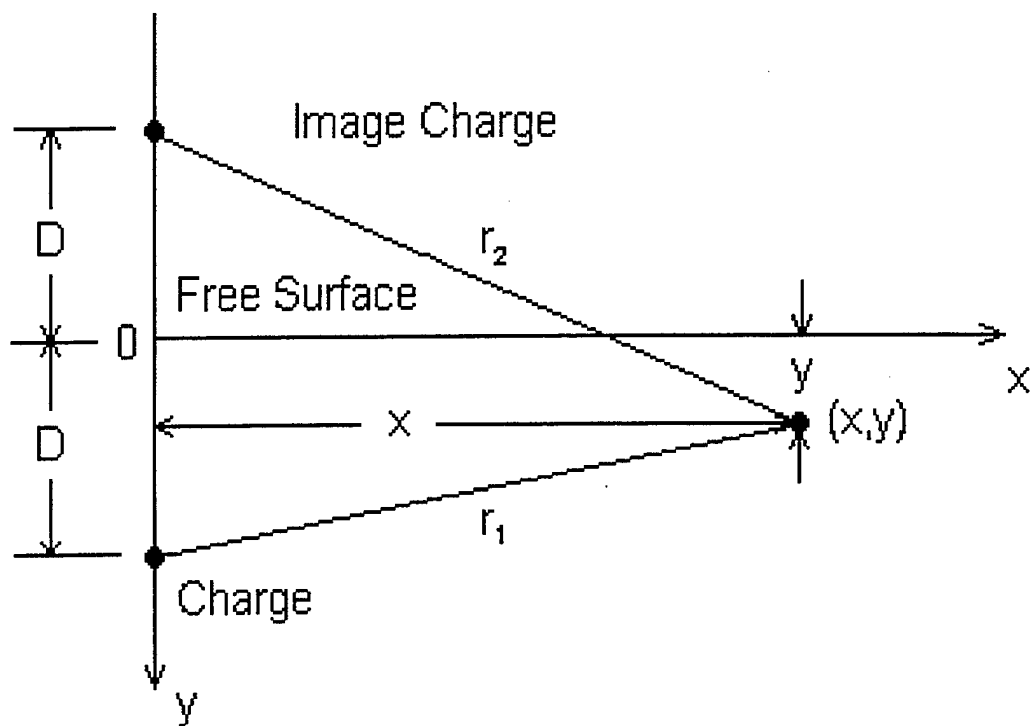


Figure 8. Charge Geometry for Bulk Cavitation Equations [From Ref. 19]

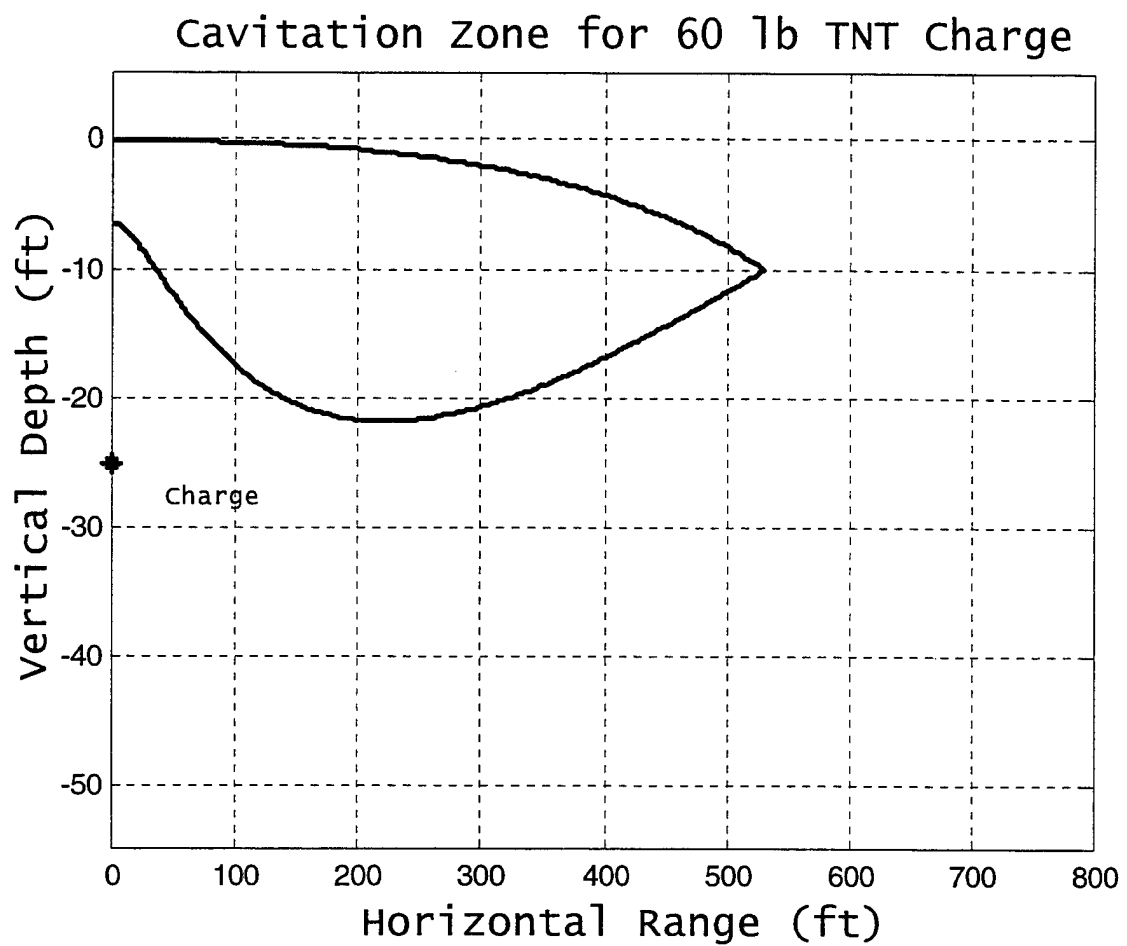


Figure 9. Bulk Cavitation Zone for 60 lbf TNT Charge at Depth of 25 ft

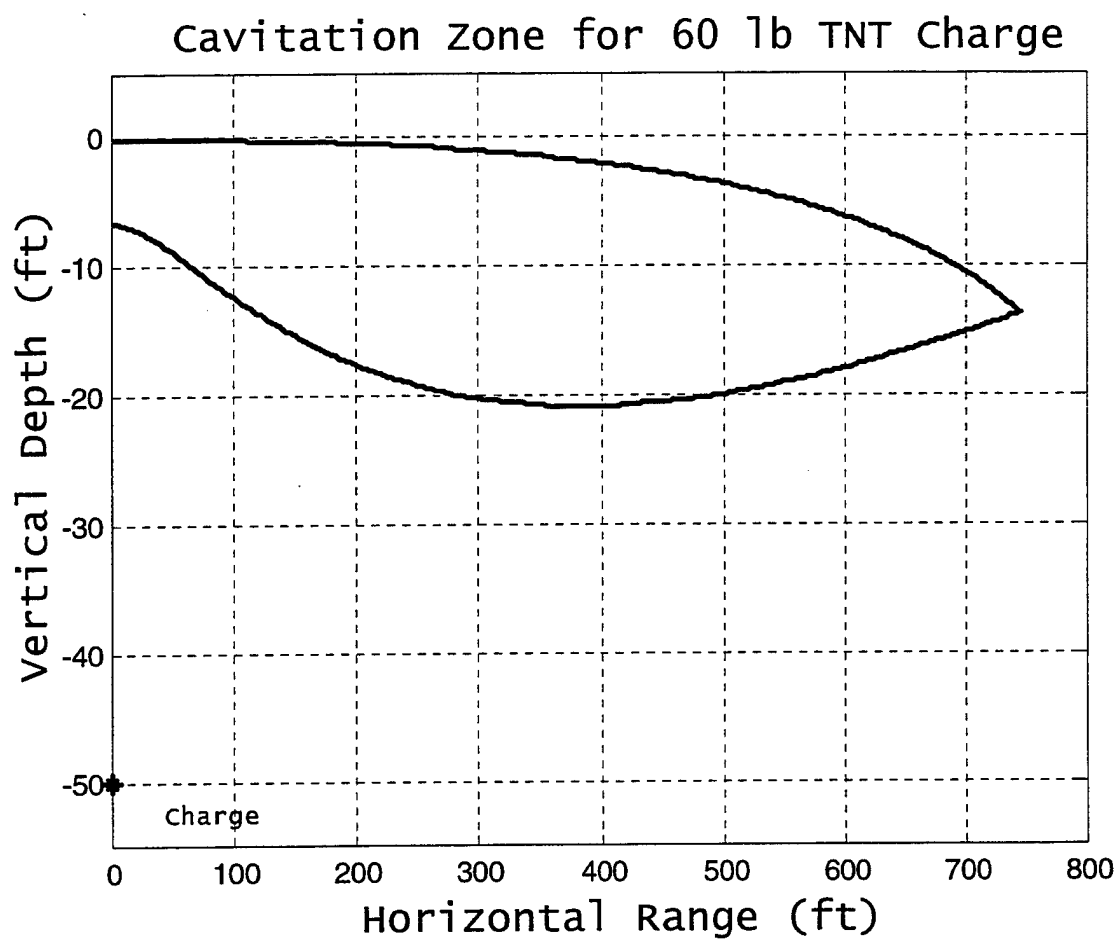


Figure 10. Bulk Cavitation Zone for 60 lbf TNT Charge at Depth of 50 ft

THIS PAGE INTENTIONALLY LEFT BLANK

IV. UNDERWATER EXPLOSION

Modeling and simulation involved a pre-processor, processor, and post-processor. A flow chart of the model building and testing procedure is shown below in Figure 11. In this investigation, the models were generated or preprocessed using TrueGrid. Next, LS-DYNA was used for the analysis and solution (processor). Finally, results were displayed utilizing LS-POST and MATLAB programs.

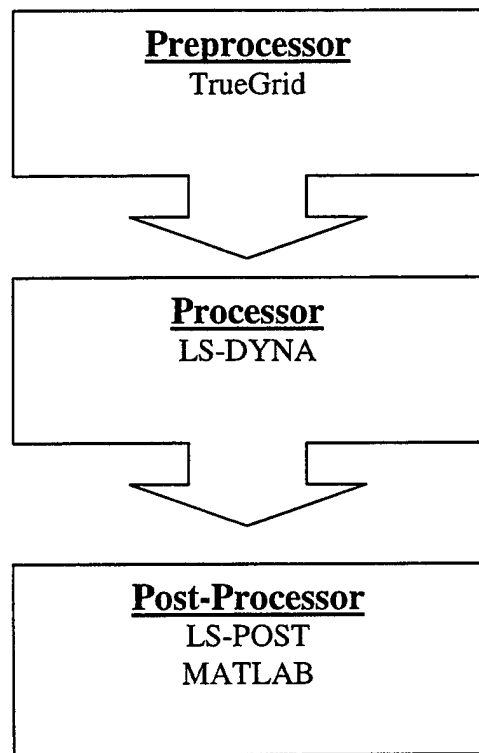


Figure 11. Flow Chart Model Construction and Simulation

A. MODEL CONSTRUCTION AND DIMENSIONS

TrueGrid was used to model several underwater explosion scenarios. The TNT explosive was modeled first, since the TNT's geometry dictated the entire model mesh. Next, the surrounding fluid and air meshes were generated. And finally, a floating structural model, a barge, was modeled as an "independent system" within the fluid mesh. Appendix B provides a general listing of TrueGrid commands [Ref. 7].

1. Explosive Model

The underwater explosion scenarios started with explosive modeling. Two different models were used in this study. The two models involved the use of a TNT explosive. The models were differed by the explosive geometry, namely a block charge and a "stair-cased" or "stair" charge. Since high explosives react rapidly to provide gaseous products at high temperatures and pressures from an initial volume, the explosive was modeled from an initial charge density (ρ) and charge weight (W). A charge weight of 60 lbf or 266.9 N was used in the TNT models. The explosive's initial densities were obtained [Refs. 17 and 24]. Knowing

$$W = mg \quad (4.1)$$

$$V = \frac{m}{\rho} \quad (4.2)$$

where g is the gravitational constant, m is the explosive mass, V is the explosive's initial volume. So, the TNT's initial volume was computed. The TNT explosive was initially modeled as a rectangular box (Figure 12). Appendix C provides the TrueGrid commands for the TNT rectangular explosive block case.

The entire mesh for the rectangular explosive block case would prove to be too coarse during the simulation runs, so the entire mesh was refined through remodeling the TNT explosive. A stair-cased shape TNT explosive model was generated to simulate a

quarter of a sphere. In order to accomplish this, the original volume, V , was broken up into fourteen separate sub-volumes, V^* , such that

$$V^* = \frac{V}{14} \quad (4.3)$$

These sub-volumes were then arranged in a "stair" manner to simulate a one-fourth of a spherical mine (Figures 13 through 15). Furthermore, the "stair" element length size, l_s , was calculated from V^* such that:

$$l_s = \sqrt[3]{V^*} \quad (4.4)$$

Since stair element length size is less than the rectangular block element length size, the overall mesh modeling is much more refined with the stair element length size. Appendix D provides the TrueGrid commands for stair TNT explosive. Table 1 provides the charge modeling characteristics for both the rectangular block and stair geometries.

The TNT rectangular block explosive charge consisted of 16 nodes, which composed 3 eight-noded solid elements. For stair explosive charge, the explosive model consisted of 50 nodes, which composed 14 eight-noded solid elements. LSDYNA's MAT_HIGH_EXPLOSIVE_BURN material type was used to model the TNT. Table 2 illustrates TNT's material properties [Ref. 17]. TNT material type also requires an EOS. Equation (2.18) is the JWL EOS for high explosives. Table 3 provides TNT's parameters for the JWL EOS [Ref. 17].

Appendices E and F are the LSDYNA input decks for the rectangular box and stair charges respectively. The explosive required axis-symmetric boundaries along two faces of the explosive. By placing an axis-symmetric boundary along the charge's X-Y plane, the nodes along the boundary were translationally and rotationally constrained in the Z direction. Additionally, by placing an axis-symmetric boundary along the X-Z plane, the nodes along the boundary were translationally and rotationally constrained in the Y direction. Figures 12 and 14 illustrate the axis-symmetric boundaries.

Charge Type	Charge Weight (N)	Charge Density, ρ (g/cm ³) [Ref. 17]	Initial Volume, V (cm ³)	Charge Geometry	Block Element length, l_b (cm)	Stair Element length, l_s (cm)
TNT	266.9	1.63	16690	Block	17.45/ 18.27	N/A
TNT	266.9	1.63	16690	Stair	N/A	10.60

Table 1. TNT Charge Modeling Characteristics

Charge	Detonation Velocity, D (cm/ μ s)	Chapman-Jouget Pressure, P_{cj} (Mbar)
TNT	0.693	0.210

Table 2. TNT Charge Characteristics (Ref. 17)

Charge	A (Mbar)	B (Mbar)	R_1	R_2	ω	E_0 Mbar-cm ³ /cm ³	V_0 (cm ³ /cm ³)
TNT	3.71	3.23×10^{-2}	4.15	0.95	0.30	4.30×10^{-2}	1.0

Table 3. TNT Equation of State Parameters (Ref. 17)

2. Fluid Model

Upon completion of the explosive model, the fluid mesh was designed next. Appendices C and D provide the TrueGrid commands for the fluid mesh. The fluid mesh was primarily designed around the respective explosive meshes. Upon initial fluid mesh construction, several fluid solid element blocks were deleted to fit the explosive mesh adjacently to the fluid. Furthermore, additional fluid solid element blocks were deleted on the water and air surface boundary. These fluid blocks were removed to make room for the barge placement and air solid element blocks within the barge. Fluid nodes would serve as an "interface" which prevents the fluid nodes from merging with the structural surface (Figure 18). As with the explosive charge, axis-symmetric boundaries were required along the fluid's X-Y and X-Z planes. The nodes along the X-Y and X-Z planes were translationally and rotationally constrained in the Z and Y directions, respectively. Along three of the fluid model sides, non-reflective boundaries were placed to prevent unwanted reflected "noise" from those sides during the simulation runs. Figures 16 and 17 illustrate the fluid mesh's boundary constraints. Along the sixth fluid side, namely the fluid-air medium interaction, no constraints were placed.

LS-DYNA's NULL_MAT is used to model the fluid material. A water density of 1.0 g/cm^3 was used. The Gruneisen equation of state (Equation 2.15) is also incorporated to model the water. The shock Hugoniot parameters for water were obtained from the HULL code [Ref. 16] where

$$\begin{aligned} C &= 0.148 \text{ cm}/\mu\text{s} \\ S_1 &= 1.75 \\ S_2 &= S_3 = 0 \\ \gamma_0 &= 0.4934 \end{aligned}$$

The overall dimensions for the fluid mesh are 1036.32 cm x 731.52 cm x 670.56 cm. The fluid mesh density was primarily based on the explosive element length size for each scenario. In the TNT rectangular block explosive model, the fluid model possessed 100474 nodes, which composed 93961 eight-noded solid elements. In the stair model,

the fluid model consisted of 1573224 nodes, which composed 148518 eight-noded elements.

3. Air Model

After the fluid mesh was completed, the air mesh was constructed. Appendices C and D show the TrueGrid commands for the air meshes. After initial construction of the air mesh, air solid element blocks were deleted to fit the fluid mesh adjacently with the air mesh. Additionally, an axis symmetric boundary was placed along the X-Y plane requiring the nodes along the X-Y plane to be translationally and rotationally constrained along the Z direction. Along three of the air model sides, non-reflective boundaries were placed. Figures 20 and 21 describe the air mesh's boundary conditions. On top of the air model and on the fluid-air medium interaction surface, no boundary constraints were placed.

LS-DYNA's NULL_MAT is used to model the fluid material. An air density of $1.28 \times 10^{-3} \text{ g/cm}^3$ was used. The linear polynomial EOS (Equation 2.13) is used to model the air. The air was modeled as a near perfect gas such that the constants for Equation (2.13) were

$$\begin{array}{lll} C_0 & = & 0 \\ C_1 & = & 0 \\ C_2 & = & 0 \\ C_3 & = & 0 \\ C_4 & = & 0.4 \\ C_5 & = & 0.4 \\ C_6 & = & 0 \end{array}$$

The overall general dimensions for the air mesh are 1036.32 cm x 182.88 cm x 670.56 cm. The air mesh density was also based on the explosive element length size for each scenario. In the rectangular block explosive case, the air model possessed 26000

nodes, which composed 22620 eight-noded solid elements. For stair explosive case, the air model consisted of 41250 nodes, which composed 36664 eight-noded elements.

4. Structural Model

Finally, a ship-like box model, barge, was constructed for ship shock simulation. The barge's overall dimensions are 426.72 cm x 60.96 cm x 60.96 cm (Figure 24). The barge possessed two athwartships bulkheads (Figure 25). The barge was weighted with three lumped masses (1.163×10^8 g) evenly spaced along the barge's keel ensuring the center of gravity remained along the centerline (Figure 26). The barge's shell plating consisted of 0.635 cm thick steel, 0.2% C hardened, having a weight density 7.87 g/cm^3 , a Young's modulus of 210 GPa, a Poisson's ratio of 0.3, and a yield strength of 430 MPa [Ref. 24]. Furthermore, an "interface" was developed along the barge's outer structural nodes in order to prevent the nodes from merging with the fluid nodes. The overall structural finite element mesh consisted of 443 nodes, which composed 432 four-noded thin shell elements. Appendices C and D provide the TrueGrid commands for the structural model inputs.

B. ANALYSIS AND SOLUTION

1. Analysis Code Description

TrueGrid translates the generated finite element model into an LS-DYNA keyword format in order to perform the numerical analysis. LS-DYNA's arbitrary Lagrangian-Eulerian (ALE) numerical technique was incorporated in the shock analysis. Utilizing LS-DYNA's *CONSTRAINED_LAGRANGE_IN_SOLID command couples the independent Lagrangian mesh (structure shells) with the independent Eulerian mesh (fluid and air solid elements). A penalty-coupling factor of 0.1 is used for the simulation runs. Chapter II discusses the analysis and solution for the finite element mesh. The two different models were set to run for 10 msec. The finite element models used a time step scale factor of 0.67 because high explosives were used [Ref. 25]. Appendices E and F

provide the LS-DYNA input decks for the rectangular block and stair explosive cases, respectively. Appendix G provides useful LS-DYNA commands. Lastly, the units used in LS-DYNA were in centimeters, grams, and microseconds.

2. Test Description

Two different charge models, rectangular block and stair, were used in the shock simulation runs for this study. The explosive consisted of a 266.9 N charge. The attack geometry placed the charge offset from the side of the barge model by 304.8 cm. The charge depth was 731.52 cm, with a standoff distance of 792.48 cm. Figure 27 shows the attack geometry for this offset charge scenario. Using Appendix A, the bulk cavitation zone was computed and is shown in Figure 28.

C. POST-PROCESSING

The solution data output is placed into two formats for analysis: binary and ASCII. The binary data files created by the LS-DYNA simulations contain the model's finite element response information. The binary data files recorded data every 200 μsec . Thus, the simulation runs produced 50 states during the 10000 μsec time interval. LS-POST [Ref. 26] is used for three-dimensional response visualization. The powerful animation and image generation features produced by LS-POST include displacement, velocity, acceleration, and element pressure data display. Furthermore, LS-POST enabled the user to observe the shock wave propagation through the fluid or air medium. LS-POST also has the capability of extracting ASCII solution data and writing it to a separate ASCII file for later evaluation. The barge's nodal velocities were of primary importance. Eight specific nodes on the barge were recorded using the DATABASE_HISTORY_NODE command in LS-DYNA. This feature was crucial in obtaining the structural velocity and fluid pressure response and converting the data into a usable form for data interpretation. Appendix H provides some useful LS-POST commands for model post-processing. The extracted ASCII data by the LS-POST post-

processor was plotted and manipulated using MATLAB [Ref. 23]. The graphical output was converted from metric to English units while using MATLAB.

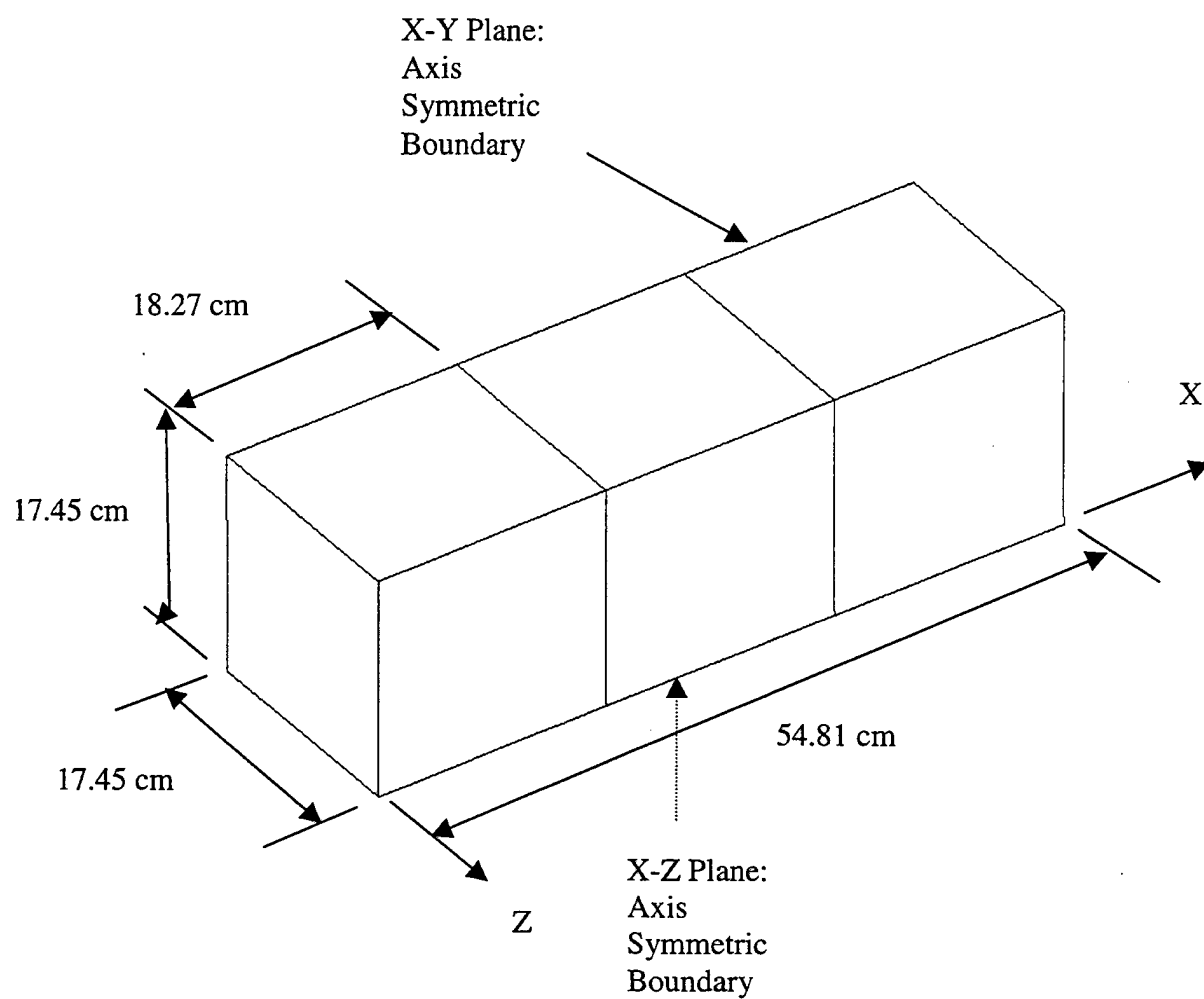


Figure 12. TNT Rectangular Block Explosive Model

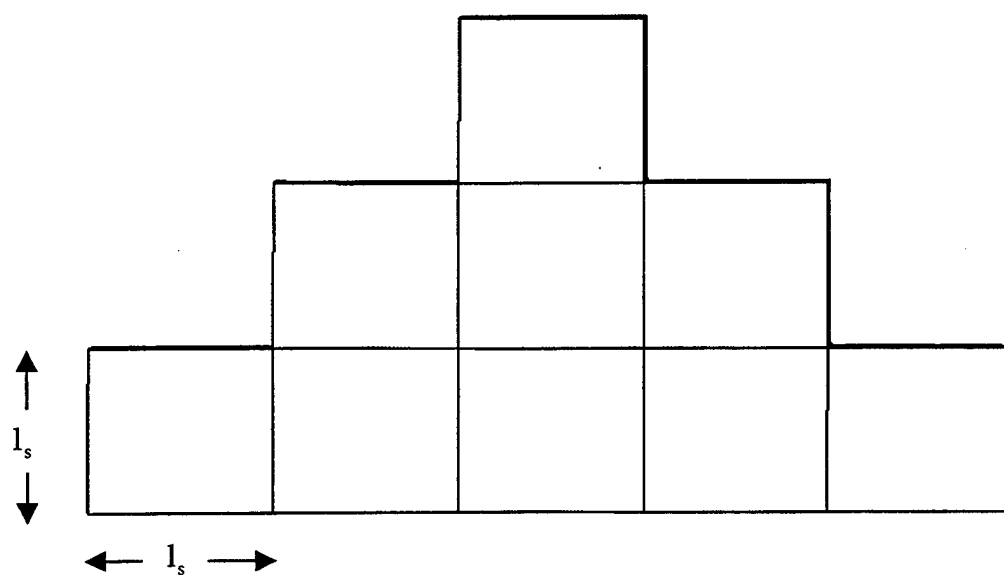


Figure 13. Stair-Cased Explosive Model for TNT (Back View)

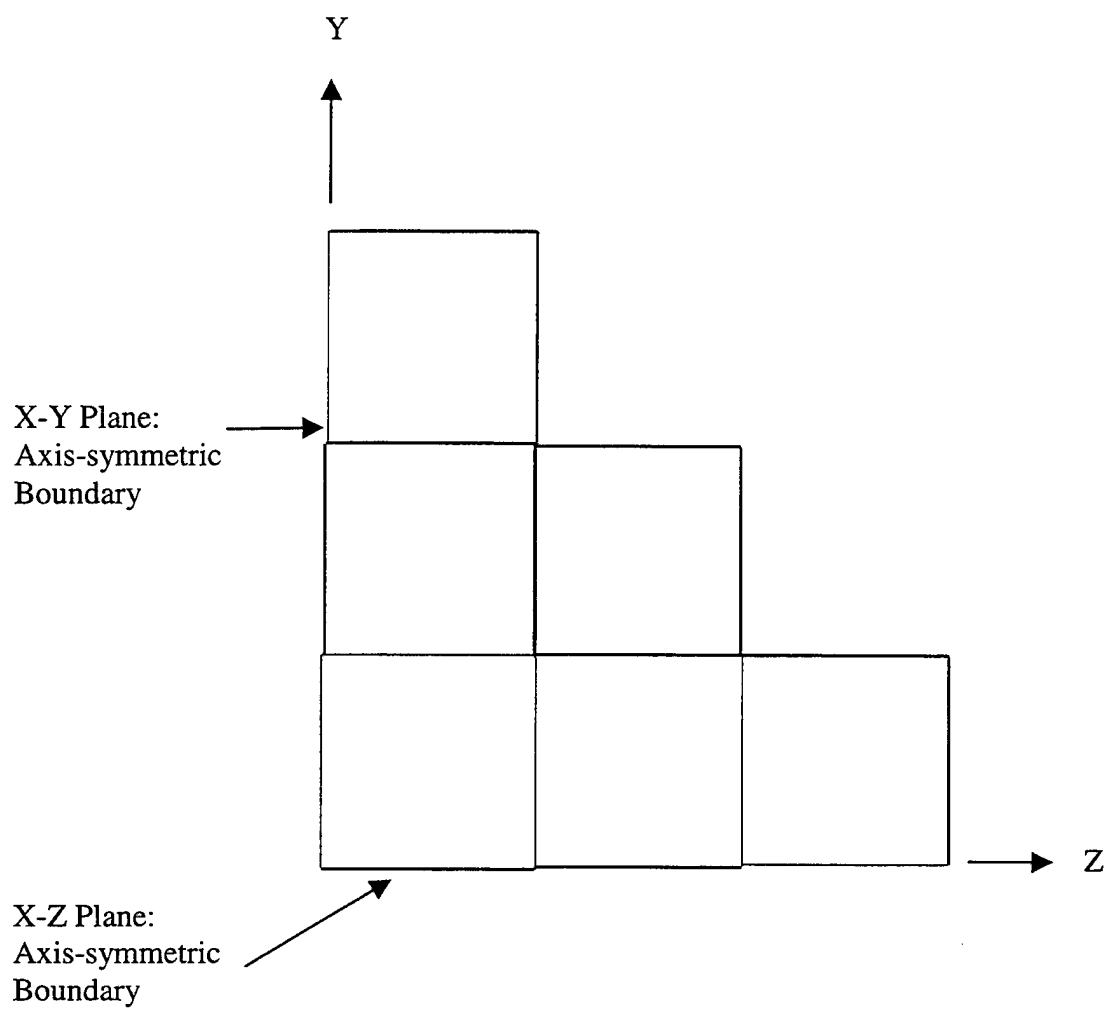


Figure 14. Stair-Cased Explosive Model for TNT (Side View)

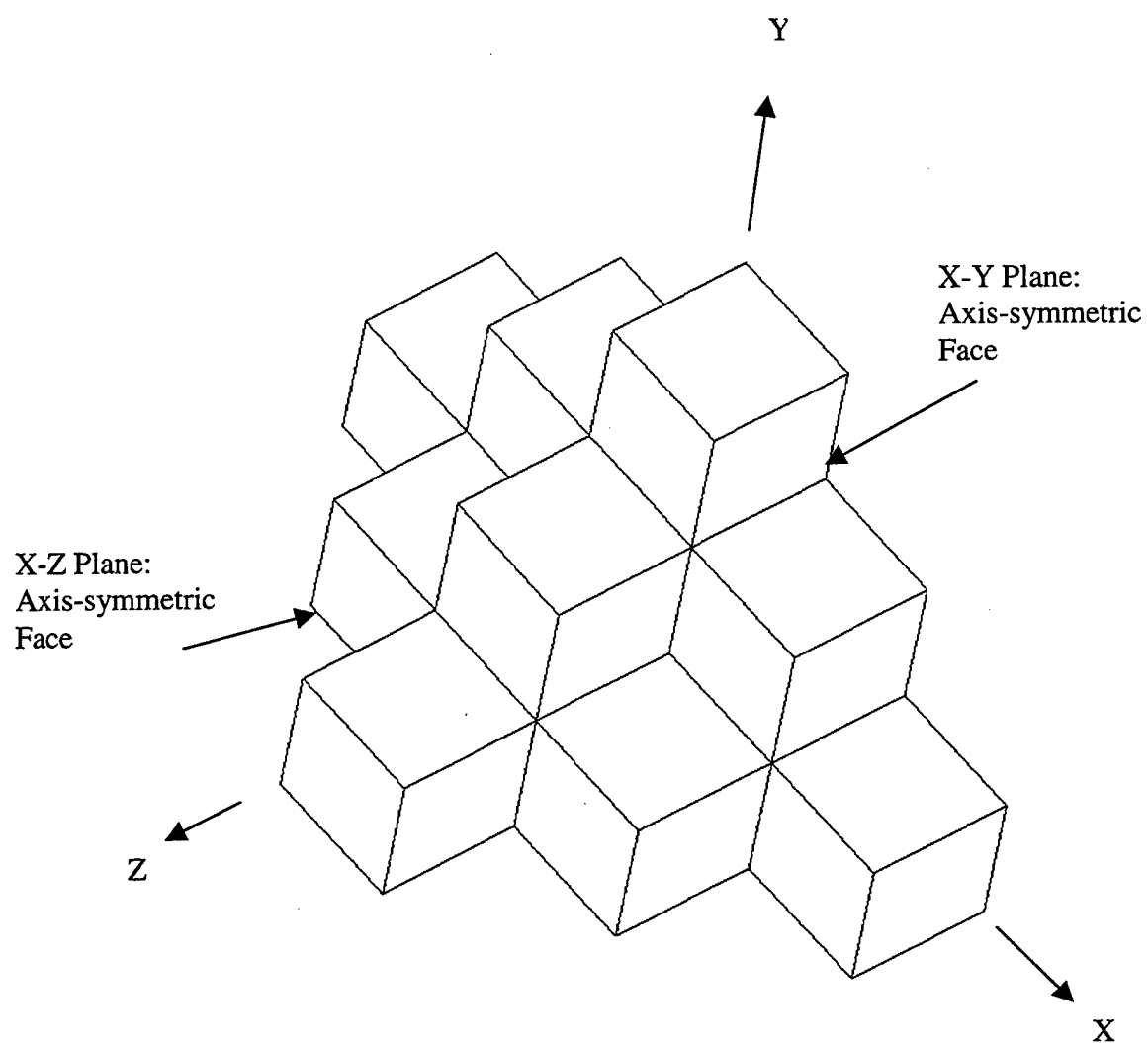


Figure 15. Stair-Cased Explosive Model for TNT (Angle View)

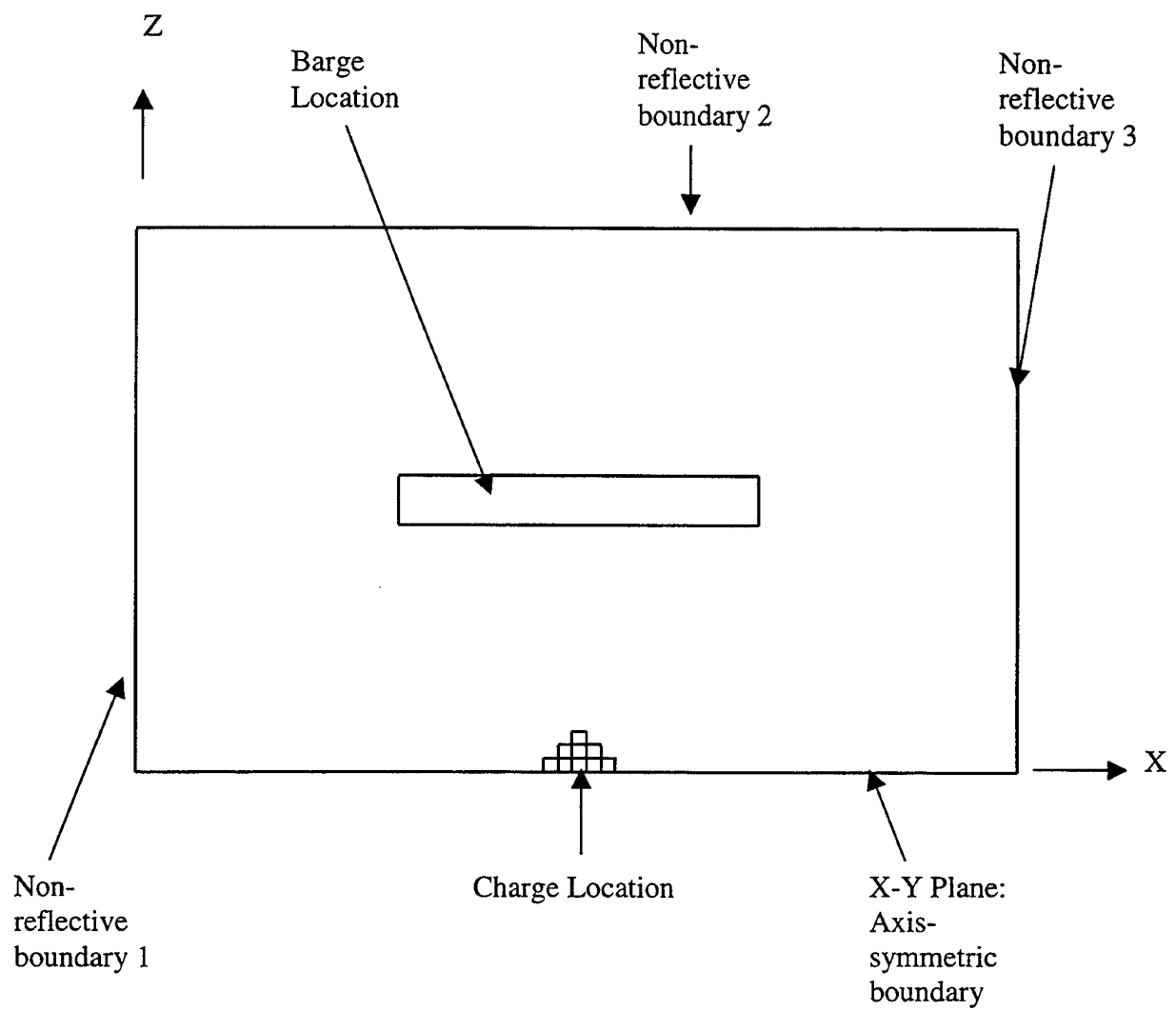


Figure 16. Fluid Mesh (Top View)

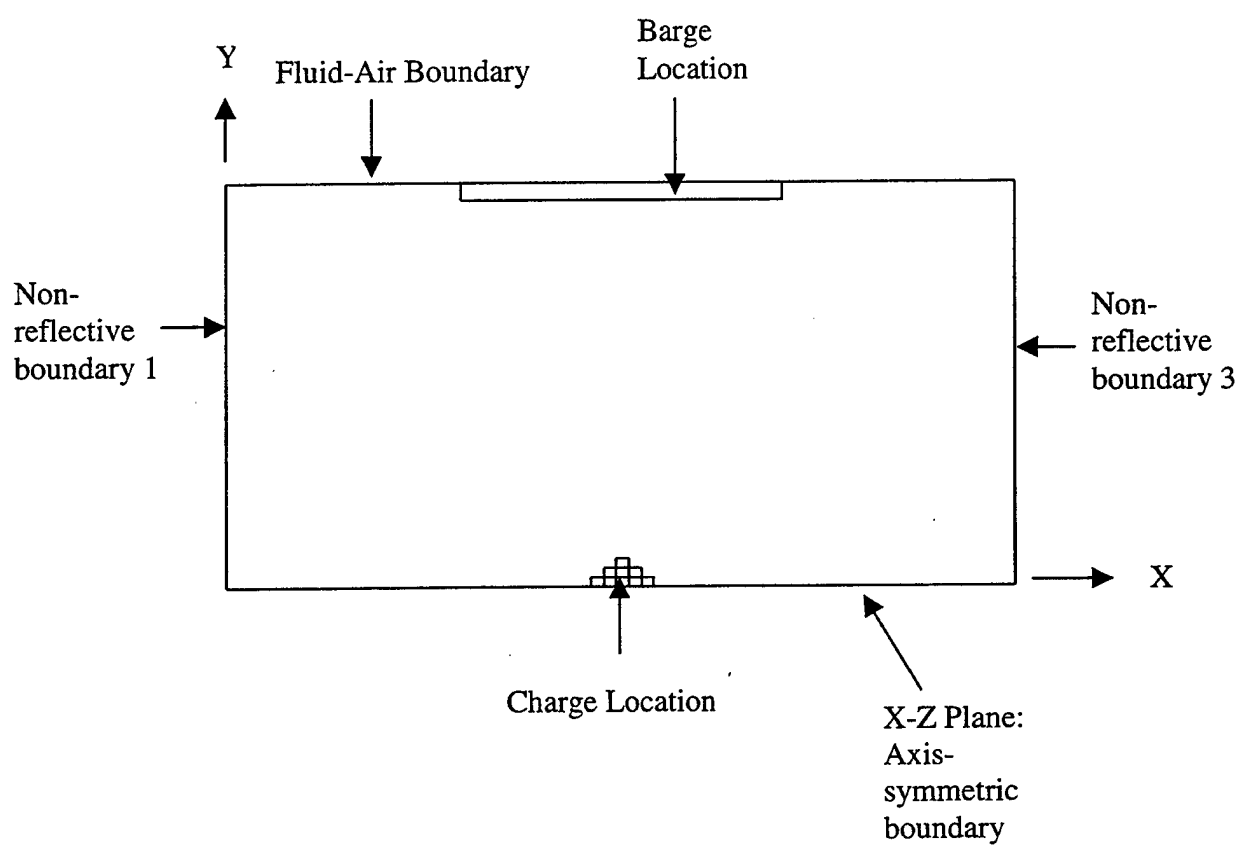


Figure 17. Fluid Mesh (Side View)

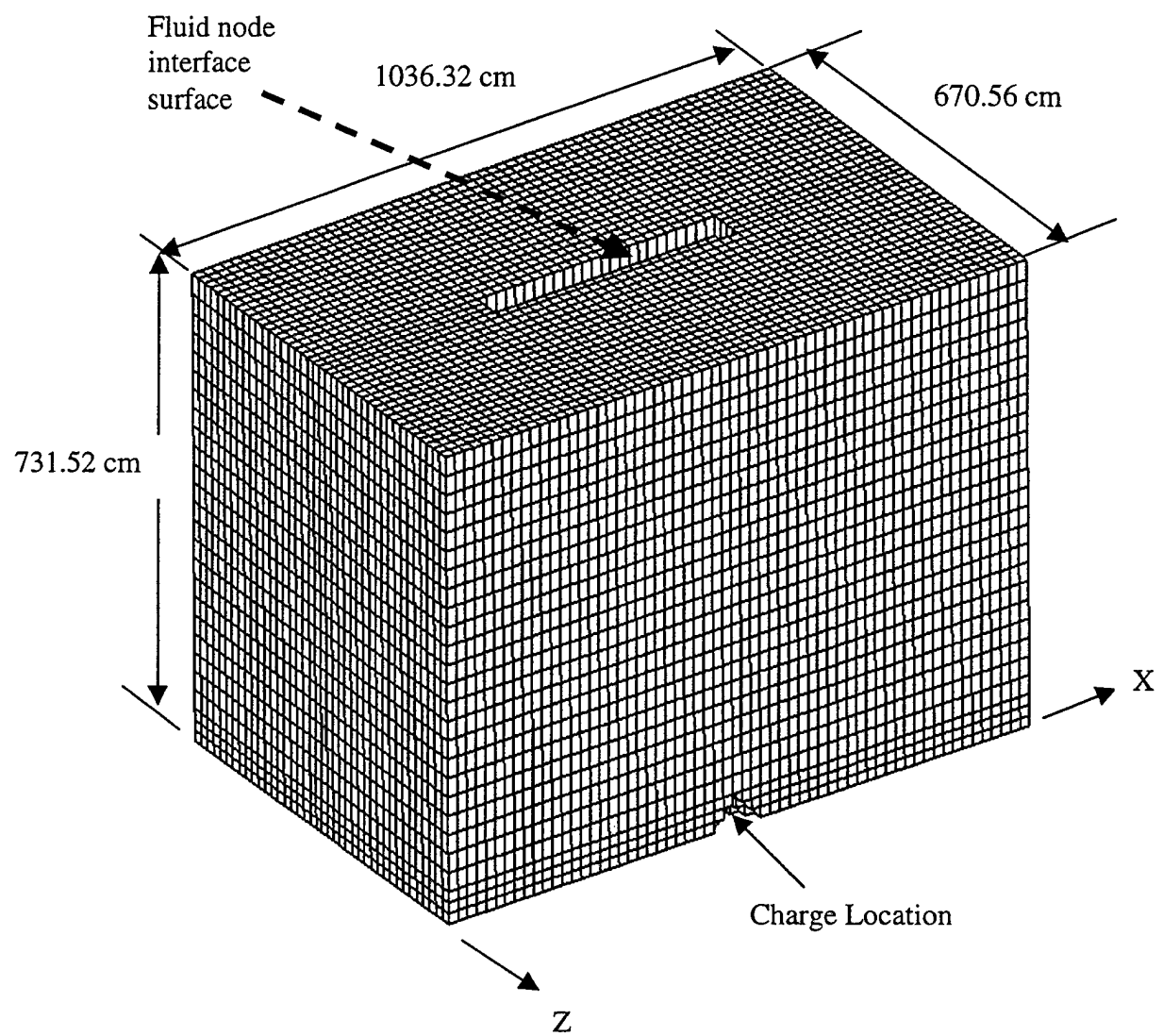


Figure 18. Three-Dimensional Fluid Mesh

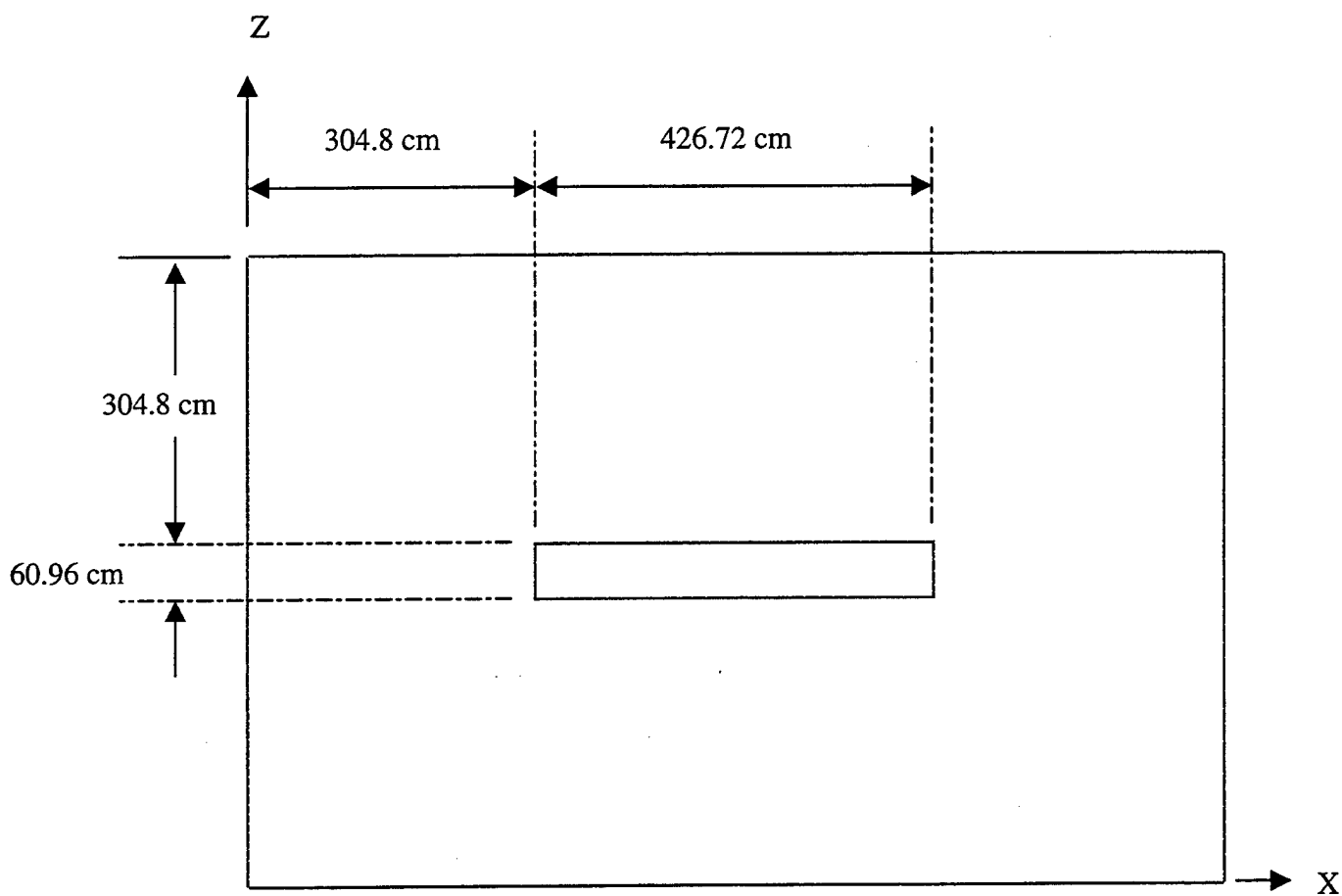


Figure 19. Three-Dimensional Fluid Mesh Parameters (Top View)

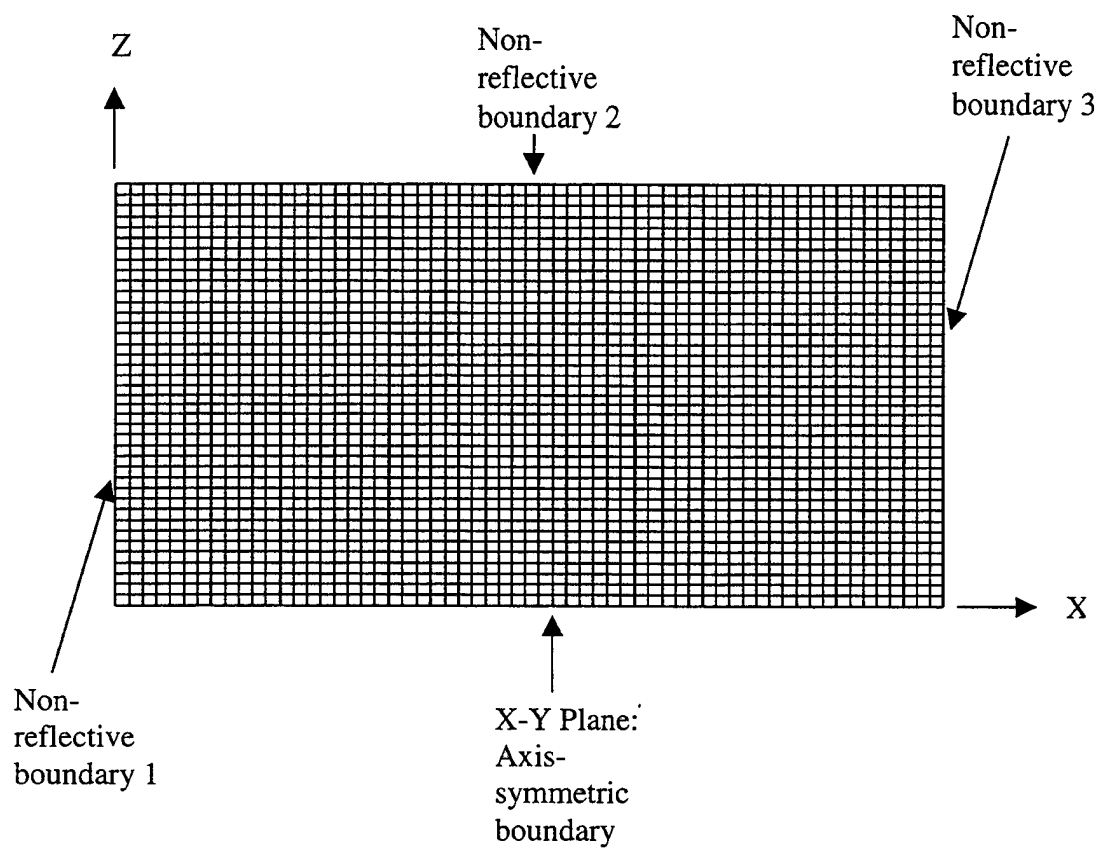


Figure 20. Air Model (Top View)

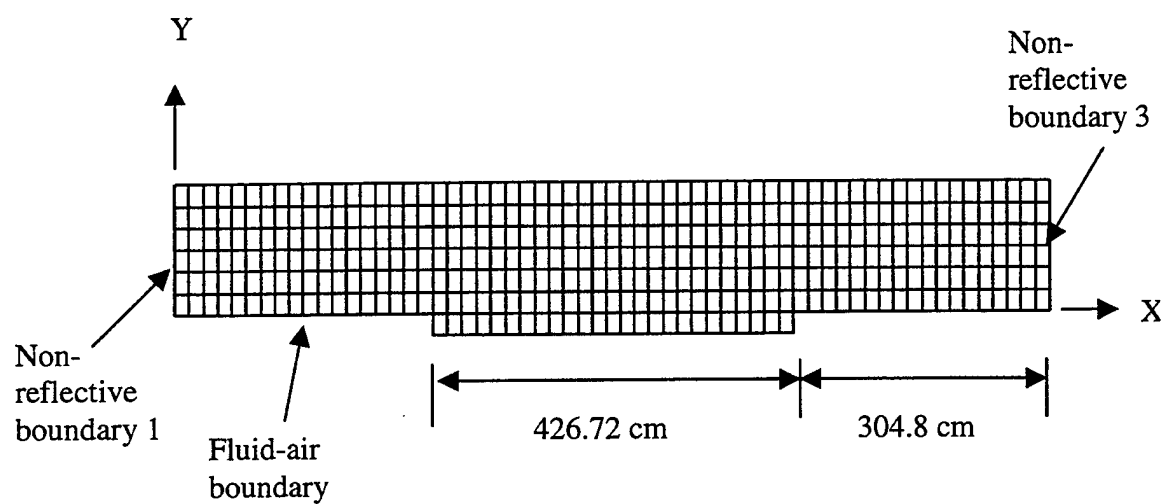


Figure 21. Air Model (Side View)

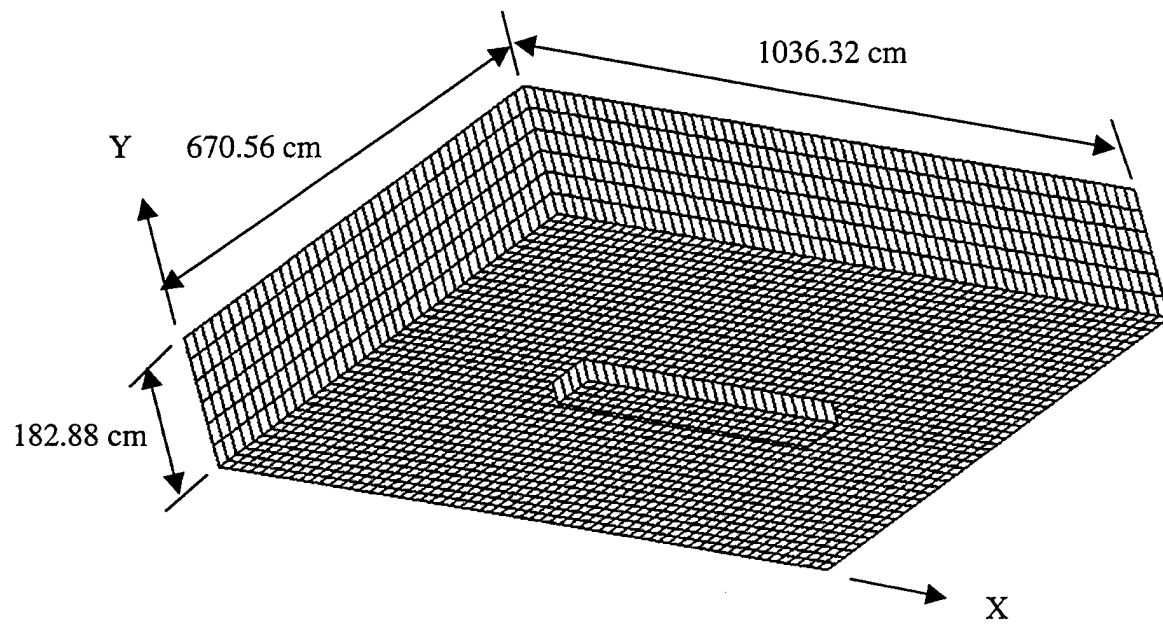


Figure 22. Three-Dimensional Air Mesh

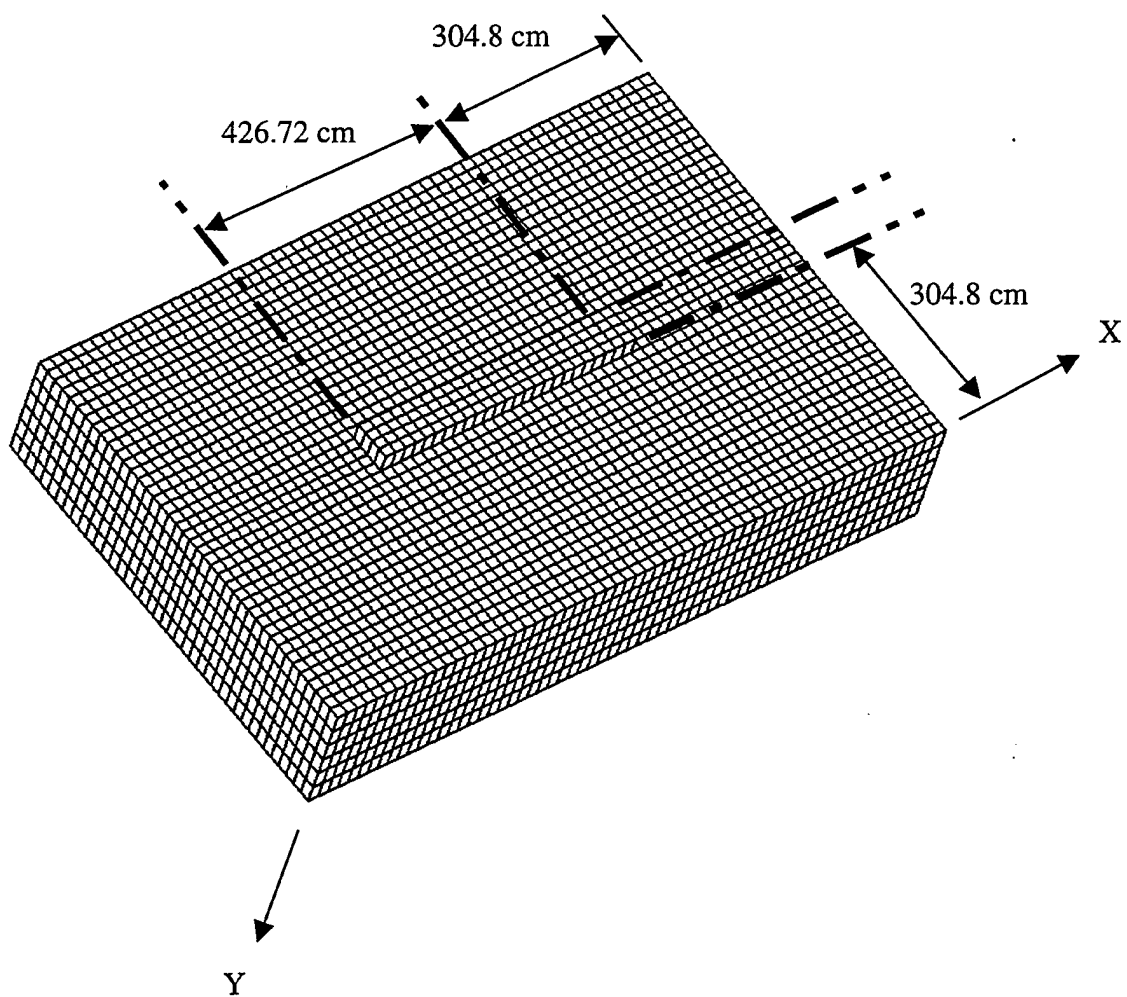


Figure 23. Three-Dimensional Air Mesh Parameters

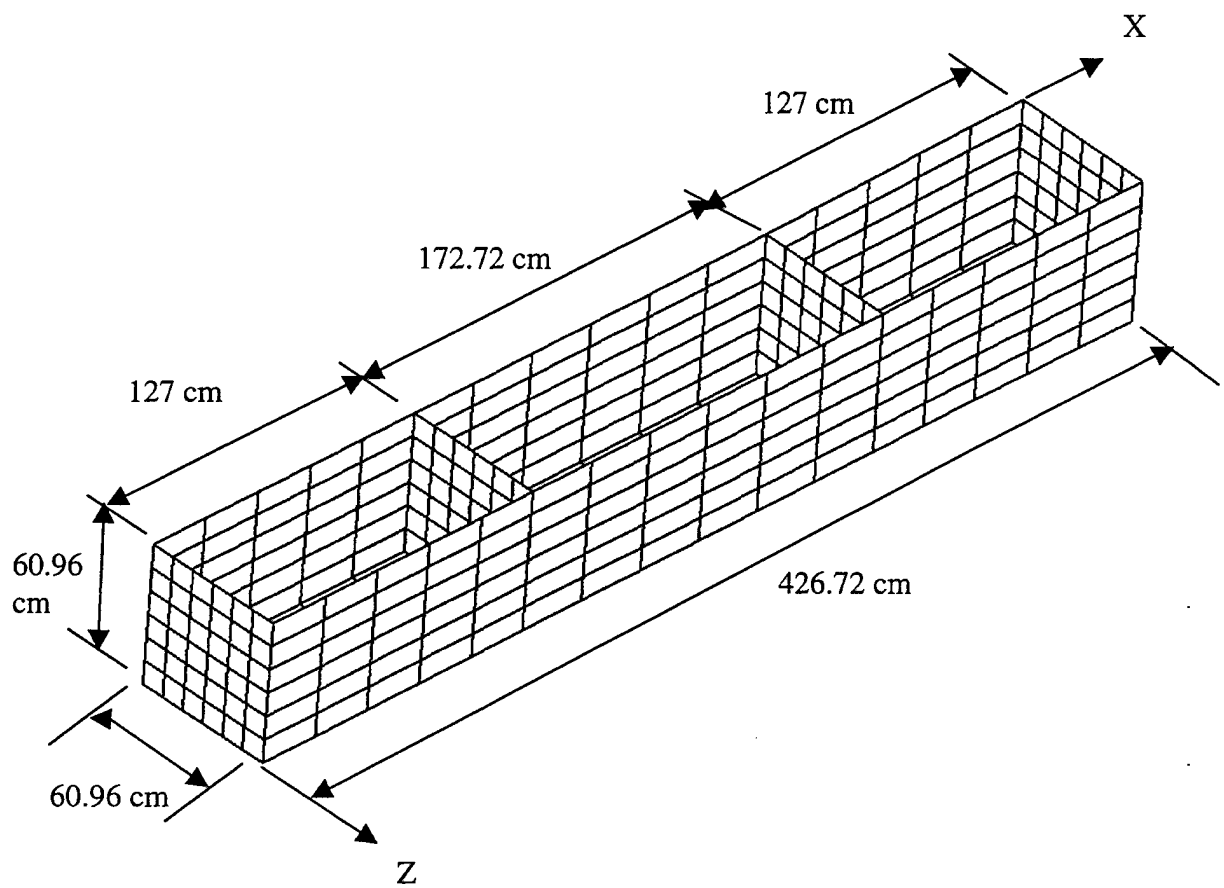


Figure 24. Three-Dimensional Barge

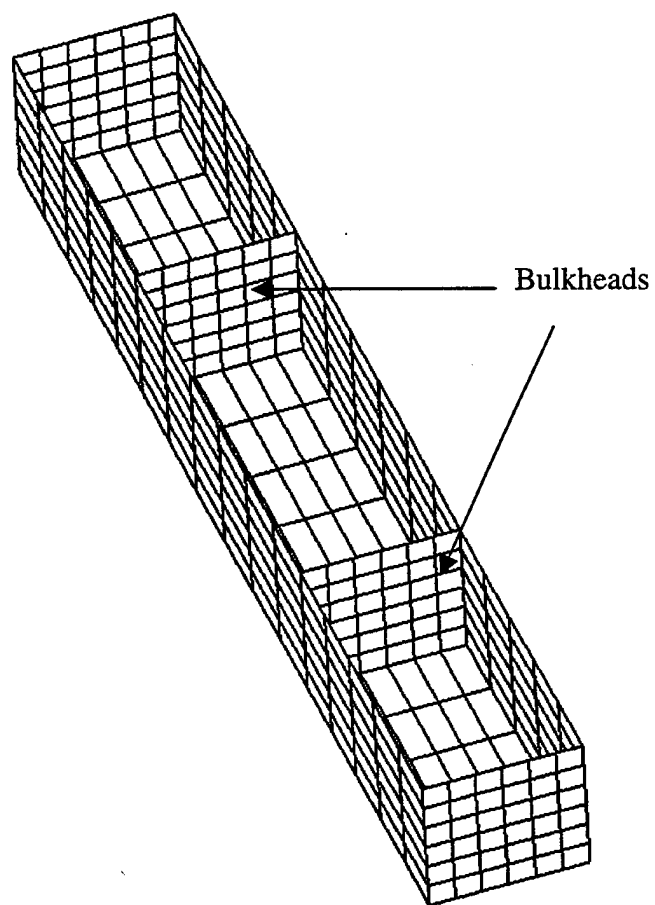
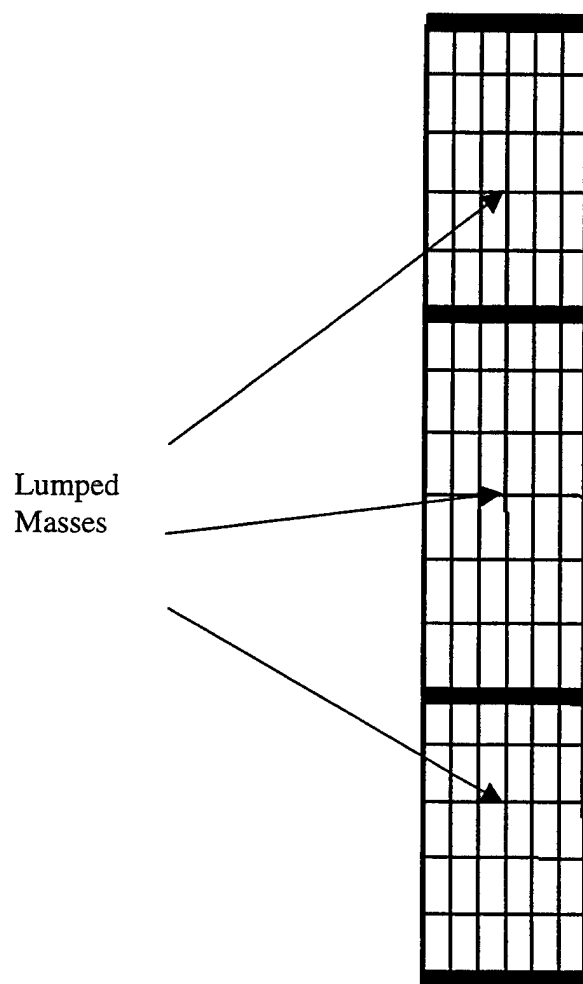


Figure 25. Three-Dimensional Barge (Bulkheads)



**Figure 26. Three-Dimensional Barge with Lumped Mass Locations
(Top View)**

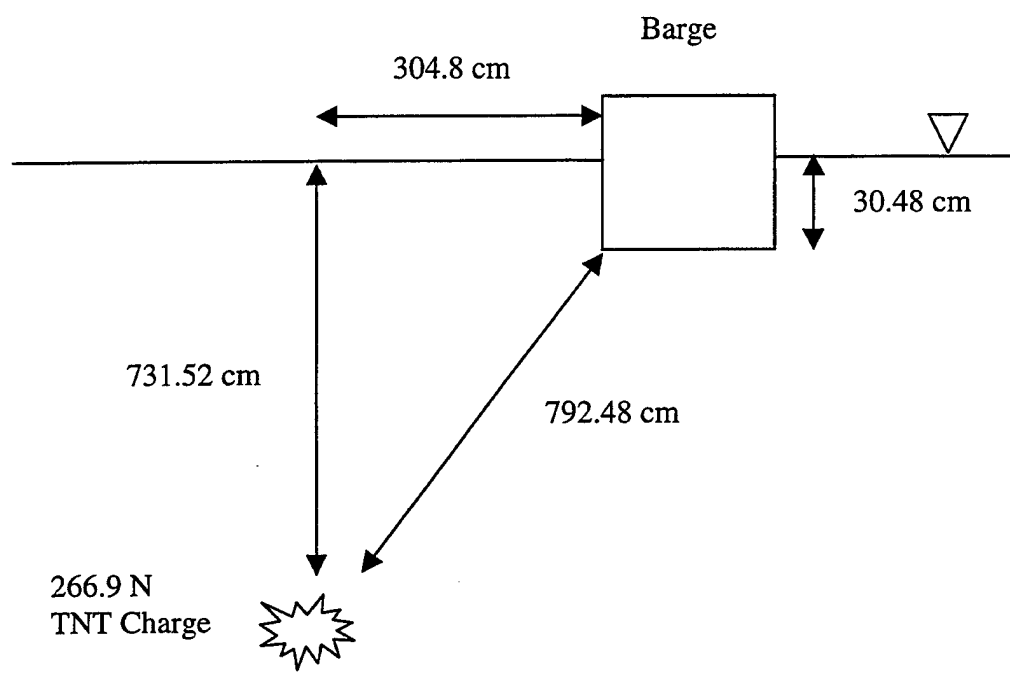


Figure 27. Offset Charge Test Geometry

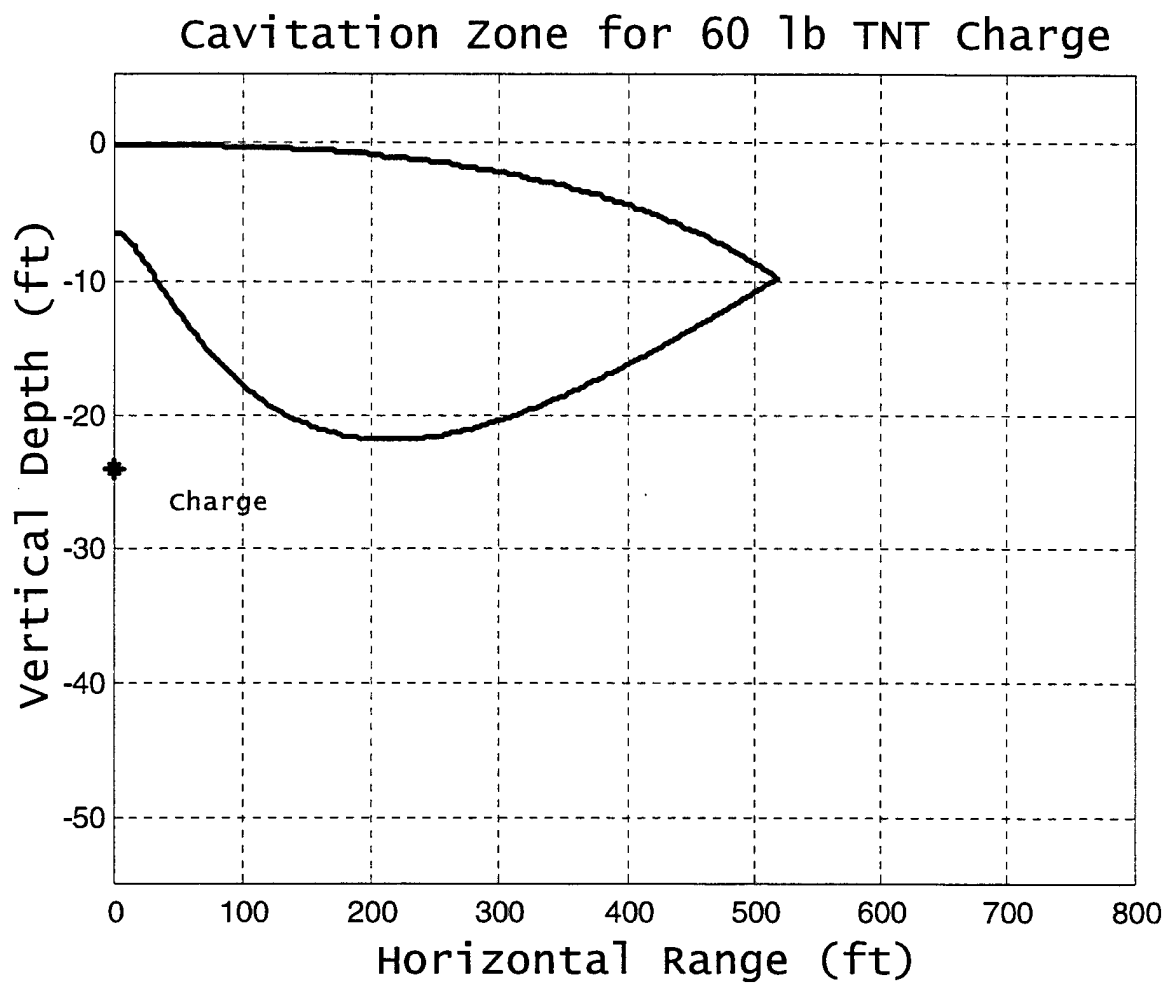


Figure 28. Bulk Cavitation Zones for 60-lbf TNT Charge at 24 ft

V. AIR EXPLOSION

A. MODEL CONSTRUCTION AND DIMENSIONS

The same process and technique applied to the underwater explosion simulations are applied to the air explosion simulations. In this two-dimensional air explosion simulation, one-fourth of a cylindrical TNT explosive is modeled. After modeling the explosive, the surrounding cylindrical air mesh is constructed, and finally a structural shell model is fabricated.

1. Explosive Model

As previously mentioned in Chapter IV, a similar methodology is approached to determine the explosive's modeling dimensions. In this two-dimensional air explosion, the simulation runs involved a 0.5 lbf or 2.22 N TNT cylindrical charge. Utilizing Equations (4.1) and (4.2), the TNT's initial volume, V , was calculated. One-fourth of the cylindrical explosive was modeled in order to save computational time and cost. The explosive's radial element length, r , was determined from the initial volume, V . Additionally, the radial element length was kept the same as the cylindrical height. So Equation (5.1) provides the radial element length such that

$$r = \sqrt[3]{\frac{V}{\pi}} \quad (5.1)$$

Therefore, in this case the explosive's radial and height dimensions were 3.54 cm (Figures 29 and 30). See Appendix I for TrueGrid command inputs.

The TNT explosive model consisted of 124 nodes, which composed 61 solid elements. LS-DYNA's MAT_HIGH_EXPLOSIVE_BURN and JWL EOS were used in conjunction for modeling the explosive material. TNT's material properties are listed in Tables 1 through 2. Figure 30 shows two boundary constraints at the extremes of the explosive's radial arm faces in order to maintain the physics of the scenario.

2. Air Model

After the fabricated explosive model, the air model was built next. The air model's dimensions were 311.52 cm from the explosive's center and a depth of 3.54 cm (Figure 31). LS-DYNA's NULL-MAT and the linear polynomial equation of state (Equation 2.13) were used to model the air. An air density of $1.28 \times 10^{-3} \text{ g/cm}^3$ was used. Since perfect gas law assumptions were used, the linear polynomial equations of state constants were $C_0 = C_1 = C_2 = C_3 = C_6 = 0$ and $C_4 = C_5 = 0.4$. As in the explosive model, the two boundary constraints were placed at the extremes of the radial arms. A non-reflecting boundary was placed on the outer-most radial curvature. Figure 32 illustrates the boundary conditions of the air model. The air model possessed 10952 nodes, which composed 5307 eight-noded solid elements. Appendix I furnishes the TrueGrid command inputs.

3. Structural Model

A cylindrical structural plate was constructed for shock simulation testing. Three different material sizes or thicknesses were modeled. The same material type used in Chapter IV is studied in this air explosion. Table 4 provides the steel material's characteristics [Ref. 24]. The three structural thicknesses investigated were 0.635 cm, 1.27 cm and 2.54 cm (Figure 33). An air gap of 2.54 cm existed between the explosive and cylindrical steel plate (Figure 34). The plate was not weighted and none of the steel's nodes were constrained. The overall structural finite element mesh consisted of 60 nodes, which composed 29 four-noded thin shell elements. Appendix I provides the TrueGrid command inputs.

Material Type	Density (g/cm ³)	Young's Modulus (GPa)	Poisson's Ratio	Yield Strength (MPa)	Ultimate Strength (MPa)
Structural Steel	7.87	250	0.30	430	620

Table 4. Material Property Characteristics

B. ANALYSIS AND SOLUTION

1. Analysis Code Description

The finite element model was translated into LS-DYNA keyword format in order to perform the numerical analysis. LS-DYNA's arbitrary Lagrangian-Eulerian (ALE) numerical technique was instituted in the air shock analysis. Utilizing LS-DYNA's *CONSTRAINED_LAGRANGE_IN_SOLID command coupled the Lagrangian mesh (structure shells) with the Eulerian mesh (air solid elements). The penalty-coupling factor remained at 0.10 for all simulation runs. Chapter II discusses the analysis and solution for the finite element mesh. The three simulation runs were set for 4 msec. The finite element models used a time step scale factor of 0.67 or less because high explosives were used [Ref. 25]. Appendices J through L provide the LS-DYNA input decks for each of the simulation runs. Appendix K shows useful LS-DYNA commands. The units of the data obtained from LS-DYNA are in centimeters, grams, and microseconds.

2. Test Description

Three different structural thicknesses were used in the air shock simulation runs. The explosive consisted of a 2.22 N (0.5 lbf) charge. The attack geometry places an air gap of 2.54 cm exists between the charge and the cylindrical structural plate. Figure 34 provides the attack geometry for the simulations with varying shell thicknesses.

C. POST-PROCESSING

The solution data output was placed into two formats for analysis: binary and ASCII. The binary data files created by the LS-DYNA simulations contained the model's finite element response information. The binary data files recorded every 50 μ sec. LS-POST was used for three-dimensional response visualization in displacements, velocities, accelerations and pressures [Ref. 26]. Furthermore, LS-POST enabled the user to observe and record the shock wave propagation the air medium. Animation sequences of the structural response and shock wave pressure propagation were created using the movie dialog and saving as an AVI (rle) format. LS-POST also extracted ASCII solution data and wrote the data to a separate ASCII file for later evaluation. Appendix L provides some useful LS-POST commands for model post-processing. The extracted ASCII data by the LS-POST post-processor was plotted and manipulated using MATLAB [Ref. 23]. The graphical output was converted from metric to English units while using MATLAB.

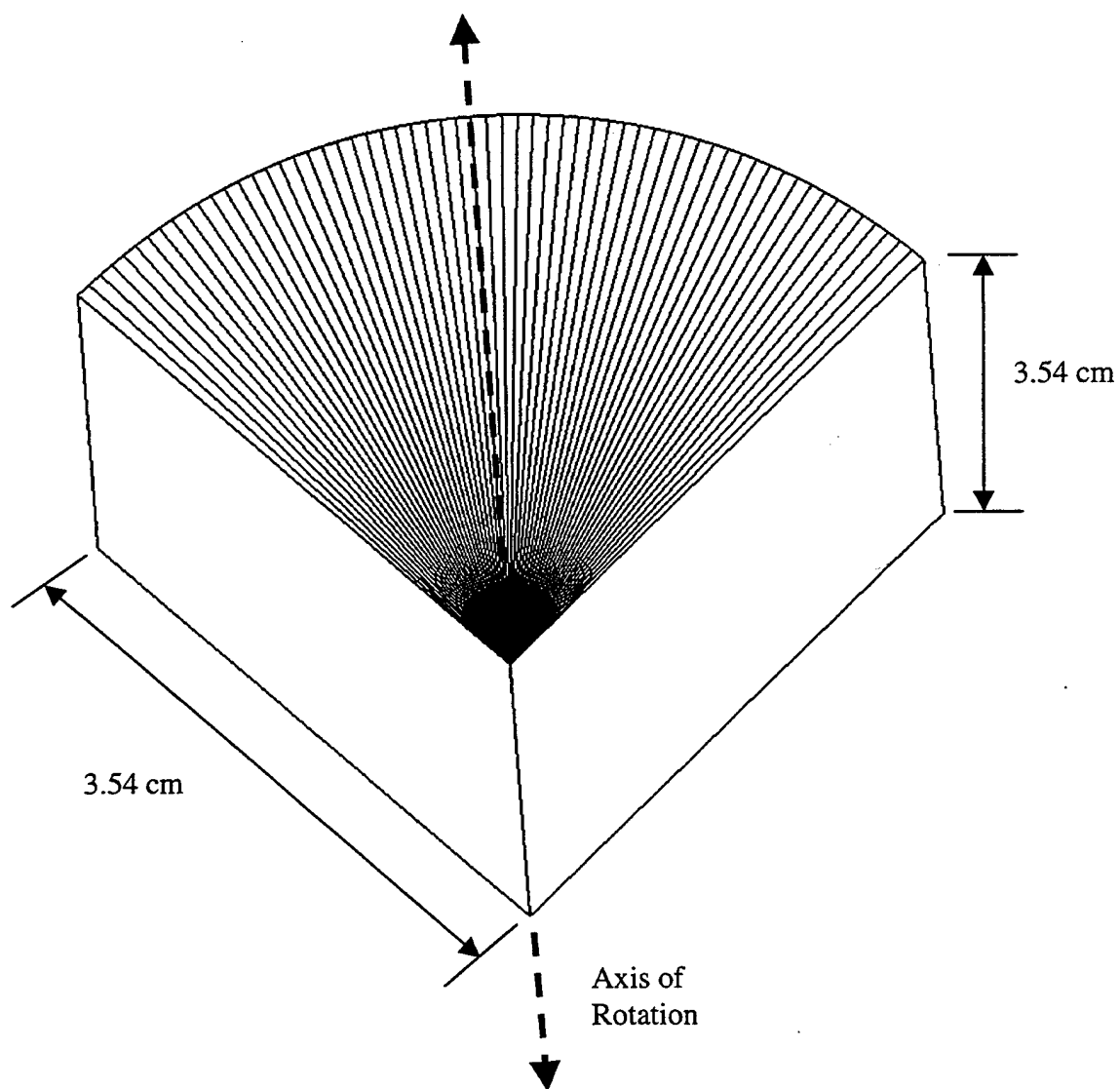


Figure 29. Explosive Model (Angle View)

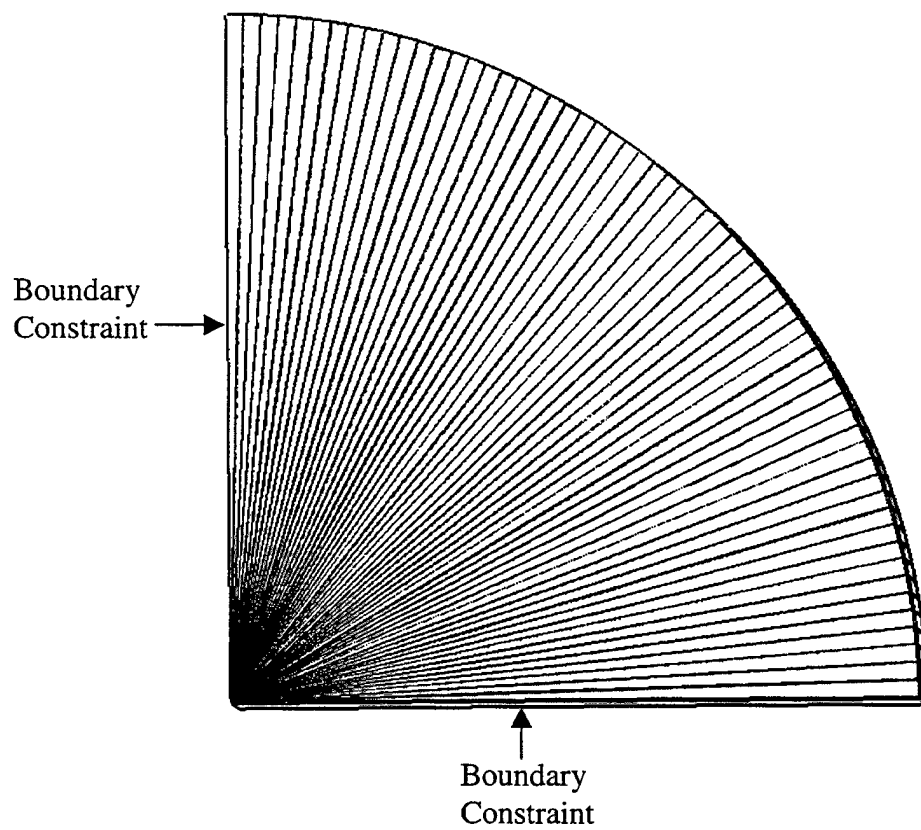


Figure 30. Explosive Model (Top View)

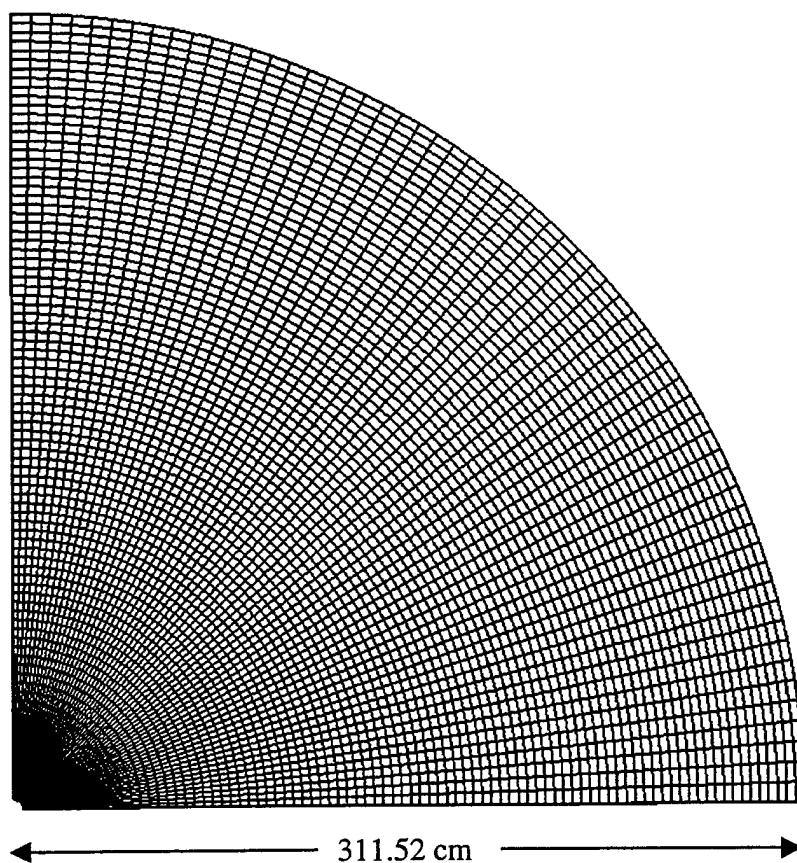


Figure 31. Air Model (Top View)

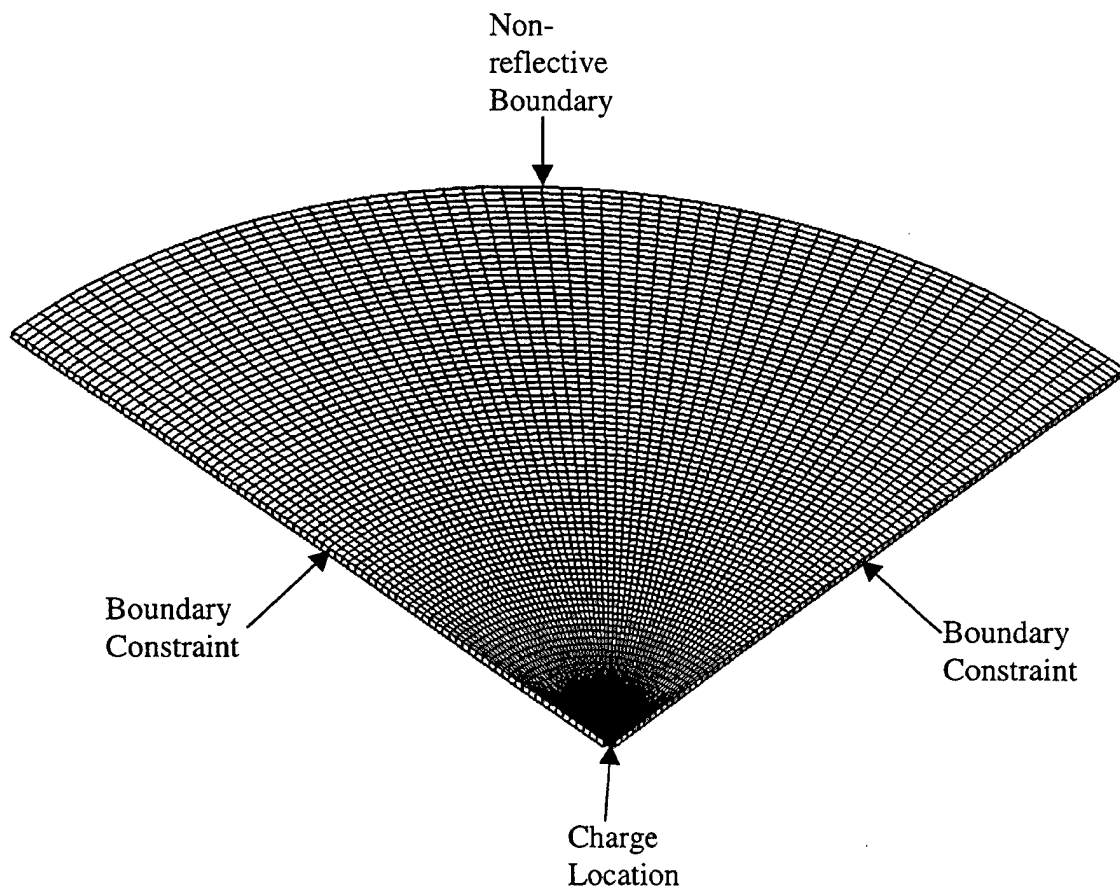


Figure 32. Air Model (Angle View)

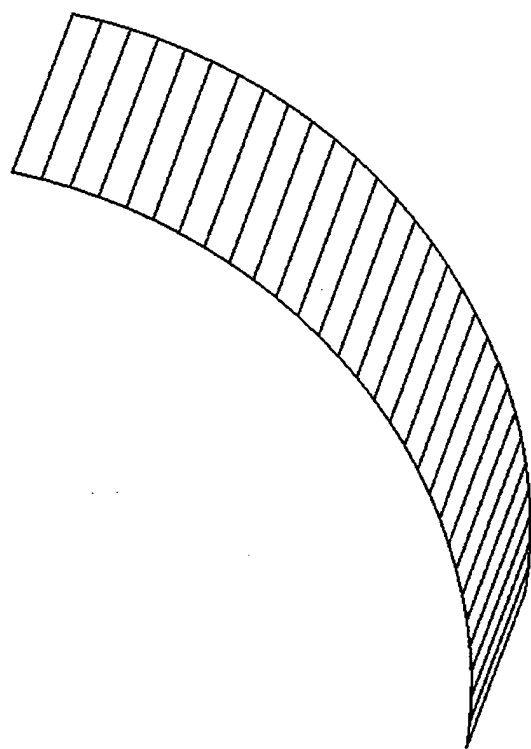


Figure 33. Steel Shell Plating

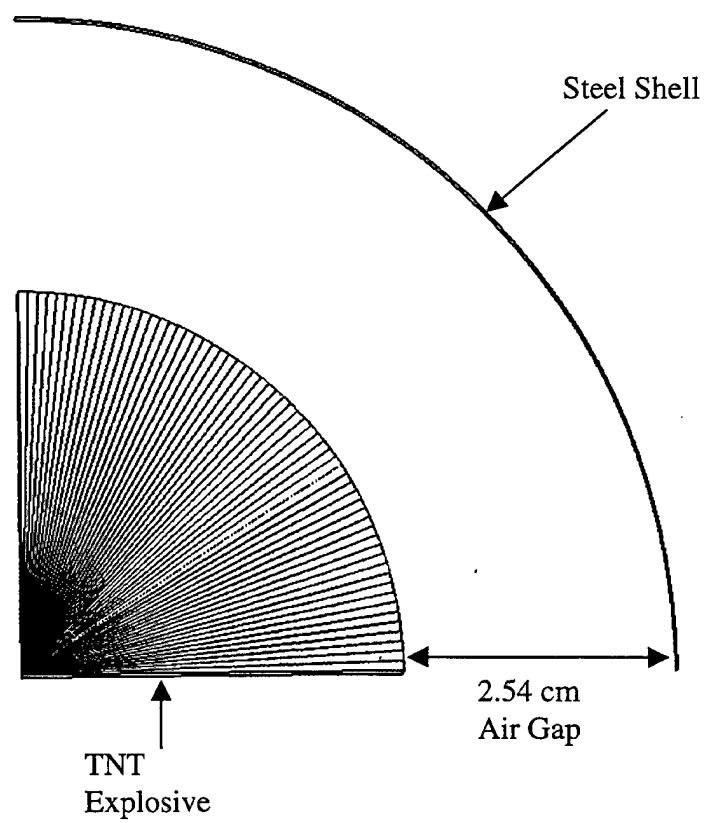


Figure 34. TNT Explosive and Steel Shell Plating

VI. SHOCK SIMULATION RESULTS

All simulations were run on an SGI Octane with a 195 MHz processor, 1.344 Gigabytes of RAM, and 23 Gigabytes of hard drive storage capacity. LS-DYNA version 960 (alpha) revision 1.174 was the numerical processing simulation codes used for the three-dimensional underwater and two-dimensional air explosions.

A. UNDERWATER EXPLOSION

Two simulations were observed for comparison, namely, the difference in explosive charge modeling. One simulation involved the use of a rectangular box explosive model. The other simulation encompassed the use of a stair-cased shape explosive model. In the fluid medium, sixteen solid fluid elements were used for comparison in the simulation, specifically five fluid elements on three different faces of the fluid mesh (X-Y axis symmetric boundary, non-reflective boundary 1, and non-reflective boundary 2) and one fluid element adjacent to the barge. Figure 16 illustrates the locations of the three faces or planes in the fluid mesh. The pressure profiles were analyzed and compared to the empirical formulations discussed in Chapter III. All of the elements exhibited a typical exponential decay waveform. When the shock pressure wave arrived at an element at a certain time, the pressure ascended quickly to a maximum pressure, P_{max} . Then, the pressure waveform exponentially decayed until the end of the simulation run. Furthermore, eight nodal points on the barge (four nodes) and the fluid mesh (four nodes) were used for comparison. Due to the bulk cavitation, the vertical velocity response, kickoff velocity, was analyzed at the structural and corresponding fluid nodes. Figures 35 and 36 illustrate the barge nodal locations for both the rectangular box and stair shape cases. The corresponding fluid nodal locations are shown in Figures 37 and 38.

1. Rectangular Block Explosive Simulation

Exploring the water's pressure response within the fluid model, sixteen solid fluid elements were used for comparison. Along the X-Y plane, nodes 1128, 1139, 46247, 46256, and 46256 were used for comparison to the underwater explosion empirical equations. Along the non-reflective boundary (NRB) 1 plane, nodes 67155, 69178, 79616, 79786, and 89068 were compared to the empirical formulations. And along the NRB 2 plane, nodes 25576, 43680, 46087, 47694, and 47706 were used for comparison. The last fluid element involved 46968 was located underneath the barge's centerline approximately. Figures 39 through 54 present the numerical and empirical pressure results. The empirical and numerical pressure profiles exhibit similar contour agreement. Tables 5 through 7 compare the results in maximum peak pressure, P_{\max} , between the empirical and numerical formulations. In comparison to the empirical P_{\max} , the numerical results show relatively good agreement at close locations and less agreement at farther locations. Three things may have a numerical effect on the water pressure profiles: (1) the explosive charge may need more refinement (as will be seen in the next section), (2) the time scale factor may require further reduction in order to capture the sharp rise in pressure in the short amount of time, or (3) the shock Hugoniot parameters for water may require further investigation. An analysis may be required to compare the linear HULL code constants in the Gruneisen EOS with other shock Hugoniot parameter constants such as Steinberg's non-linear parameters [Ref. 16].

Cavitation can also be observed in several nodes, namely nodes 46264, 47706, and 46968, which were at depths of 2.15 ft, 2.73 ft, and 1.0 ft respectively. The mentioned nodes at their respective depths were well within the cavitation zone and were in agreement with Figure 28. The other nodes were outside of the cavitational region. As expected, the water particle velocities at the fluid-air boundary behaved principally in a vertical manner due to the bulk cavitation. Additionally, the air pressure near the vicinity of the fluid-air boundary experienced little or no relative change in pressure as predicted.

Since the nodes in the fluid mesh exist independently of the structural mesh, a correspondence between the structural nodes and fluid nodes must be established. The structural nodes 124024, 124134, 124173, and 124190 correspond to the following fluid nodes, respectively, 16862, 39870, 39868, and 40492. In some instances, the structural node location did not match up exactly with the fluid node location, so the closest fluid node was chosen. Figures 55 through 58 illustrate the rapidly increasing structural and water particle vertical velocities (approximately 5 to 6 msec) to a peak value and then a rapid decrease and increase in a series of steps until the response settles down. The response does not settle out at a value of zero due to rigid body motion of the structure. The rigid body motion is due to the fact that the barge exists independently from the fluid mesh. The incident shock wave impacts the structure with a very high pressure (approximately 2500-psi at 5 msec) from charge detonation and forces the structure rapidly upward. The structure is then quickly pulled downward as the shock wave reaches the free surface and a rarefaction wave (tensile) is generated. This wave causes the pressure to decrease rapidly to zero psi, and cavitation occurs. Once cavitation occurs, the barge is released from the fluid, and the structural velocity increases at a lower magnitude. The process continues again with the cavitating fluid particles pulling downward on the structure and releasing the structure until this cycle eventually settles out.

Damping effects are present within the fluid and structural nodes as a result from the initial excitation (explosion) into the fluid medium. In LS-DYNA's ***CONTROL_ALE** command, the Rayleigh damping was set to the on position. The Gruneisen EOS takes into account damping effects within the fluid particles. The fluid particle's damping effect is then imparted to the structural nodes and produces an overall smooth velocity response. Similarities exist with previous research conducted concerning Rayleigh damping effects through the use of the LS-DYNA/USA program code [Ref. 9].

Node	Numerical Result P_{\max} (psi)	Empirical Result P_{\max} (psi)	% Error
1128	1682.0	2559.7	34.0
1139	2304.3	3113.2	26.0
46247	4998.4	5284.5	5.4
46256	3387.2	3590.6	5.7
46264	2369.0	2894.1	18.1

Table 5. Rectangular Block Case Results: Nodes Along X-Y Plane

Node	Numerical Result P_{\max} (psi)	Empirical Result P_{\max} (psi)	% Error
67155	2137.9	2694.7	21.0
69178	1793.5	2711.7	33.9
79616	1790.1	2648.5	33.8
79786	1495.9	2416.9	38.1
89068	1105.1	2022.24	45.4

Table 6. Rectangular Block Case Results: Nodes Along NRB 1

Node	Numerical Result P_{\max} (psi)	Empirical Result P_{\max} (psi)	% Error
25576	1086.4	1930.6	43.7
43680	1394.8	2150.1	35.1
46087	2395.8	2453.7	2.4
47694	1481.5	2222.1	33.3
47706	1106.5	1956.8	43.4

Table 7: Rectangular Block Case Results: Nodes Along NRB 2

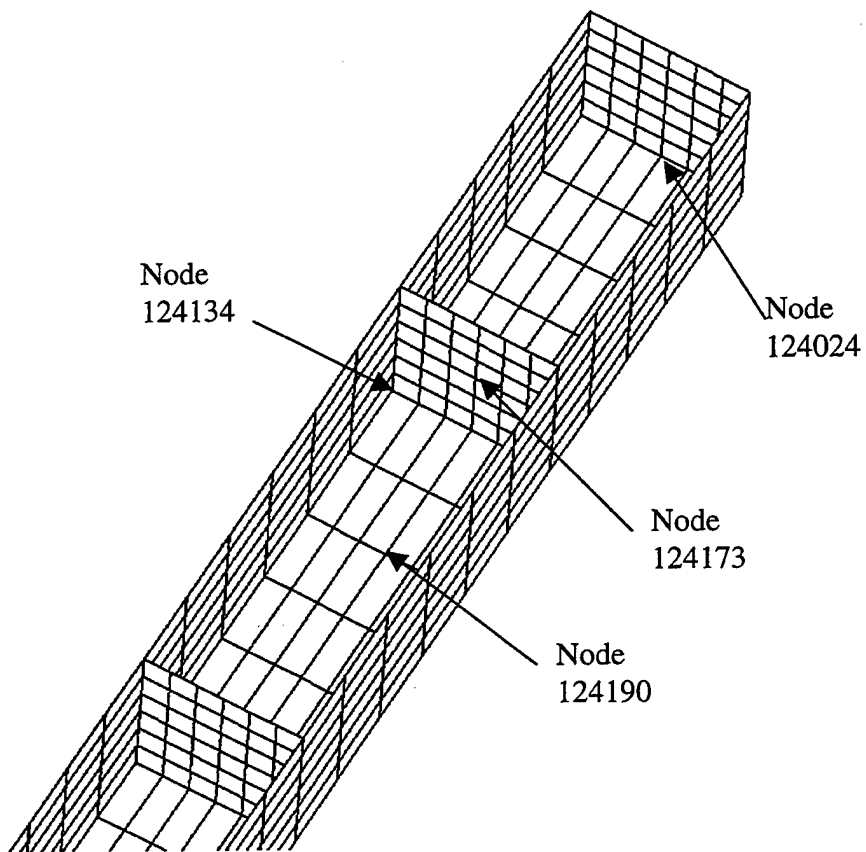


Figure 35. Barge Nodes in Rectangular Box Charge Case

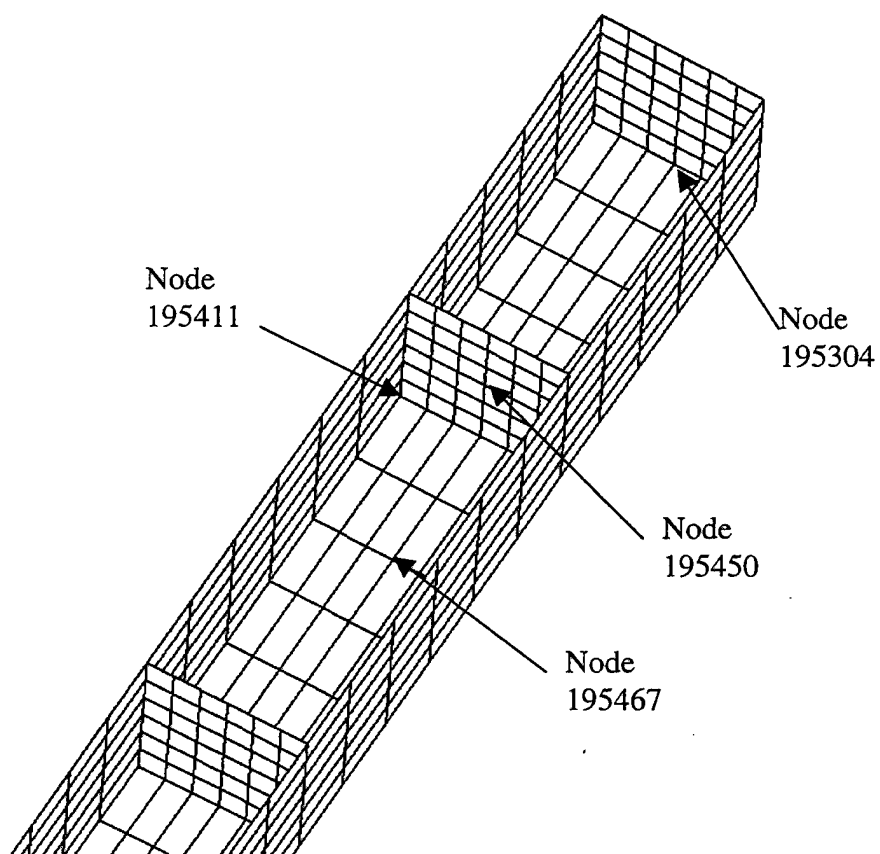


Figure 36. Barge Nodes in Stair Charge Case

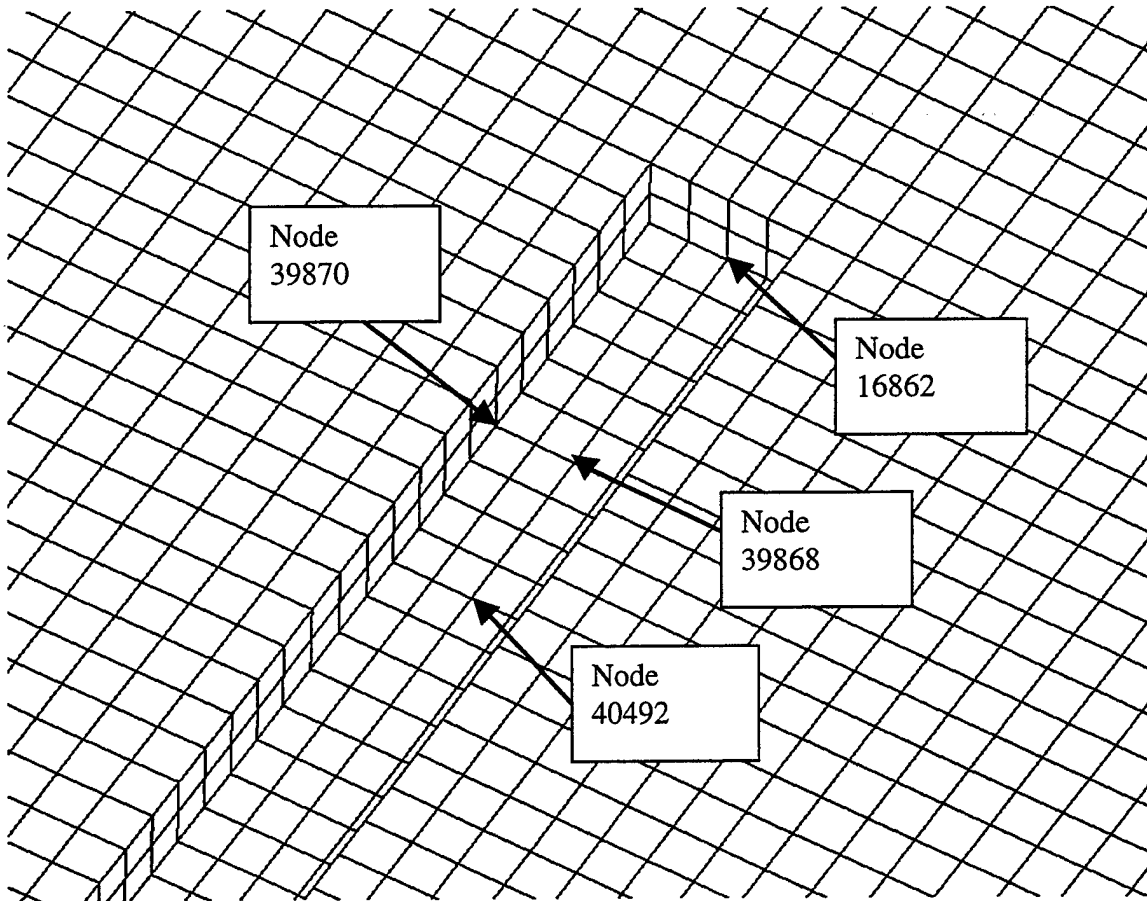


Figure 37. Fluid Nodes in the Rectangular Box Charge Case

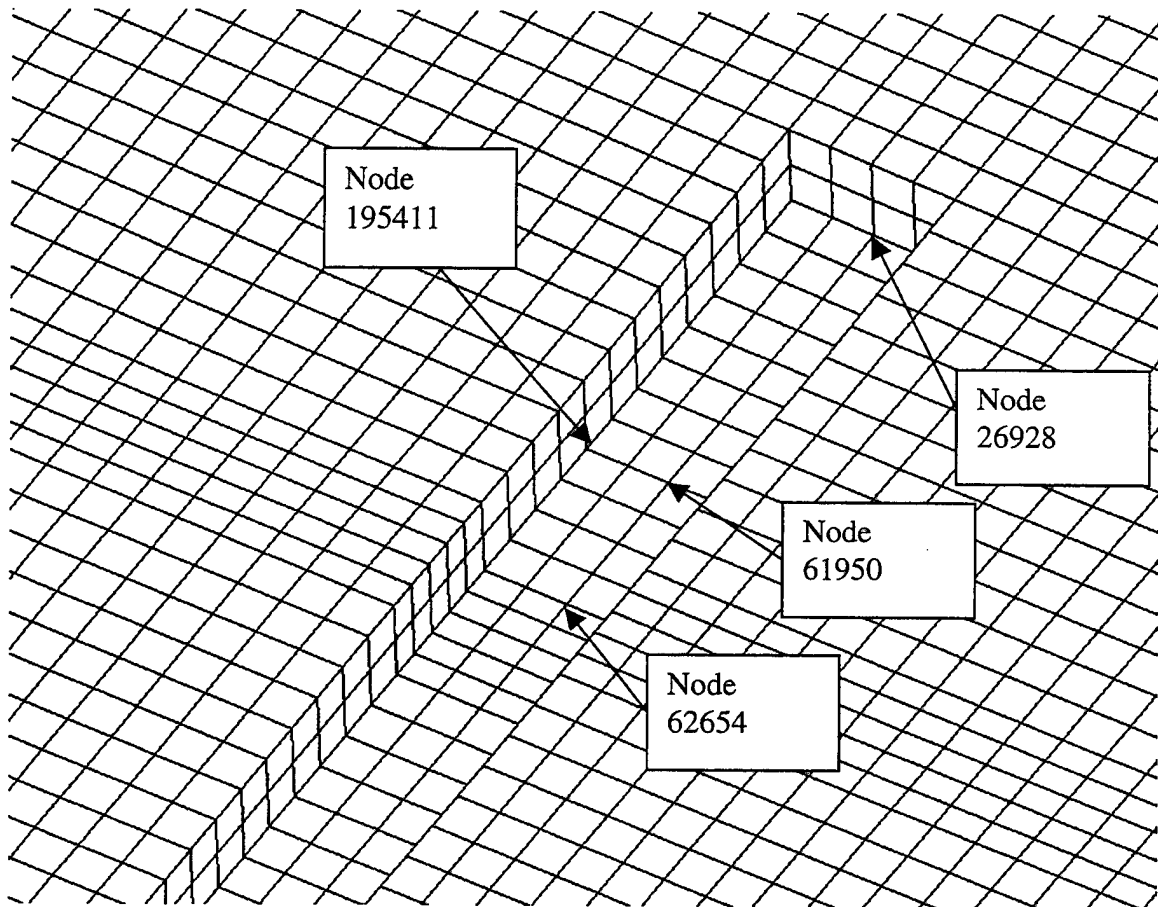


Figure 38. Fluid Nodes in the Stair Charge Case

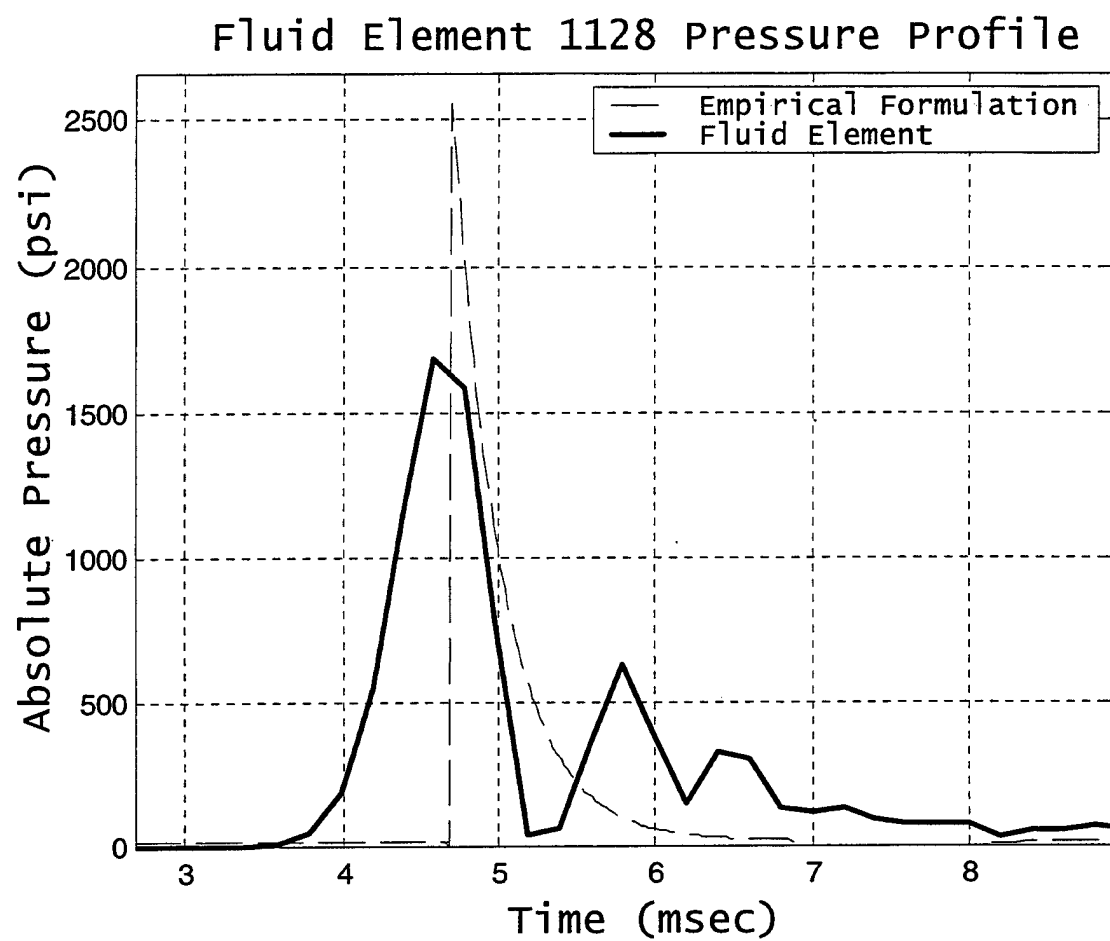
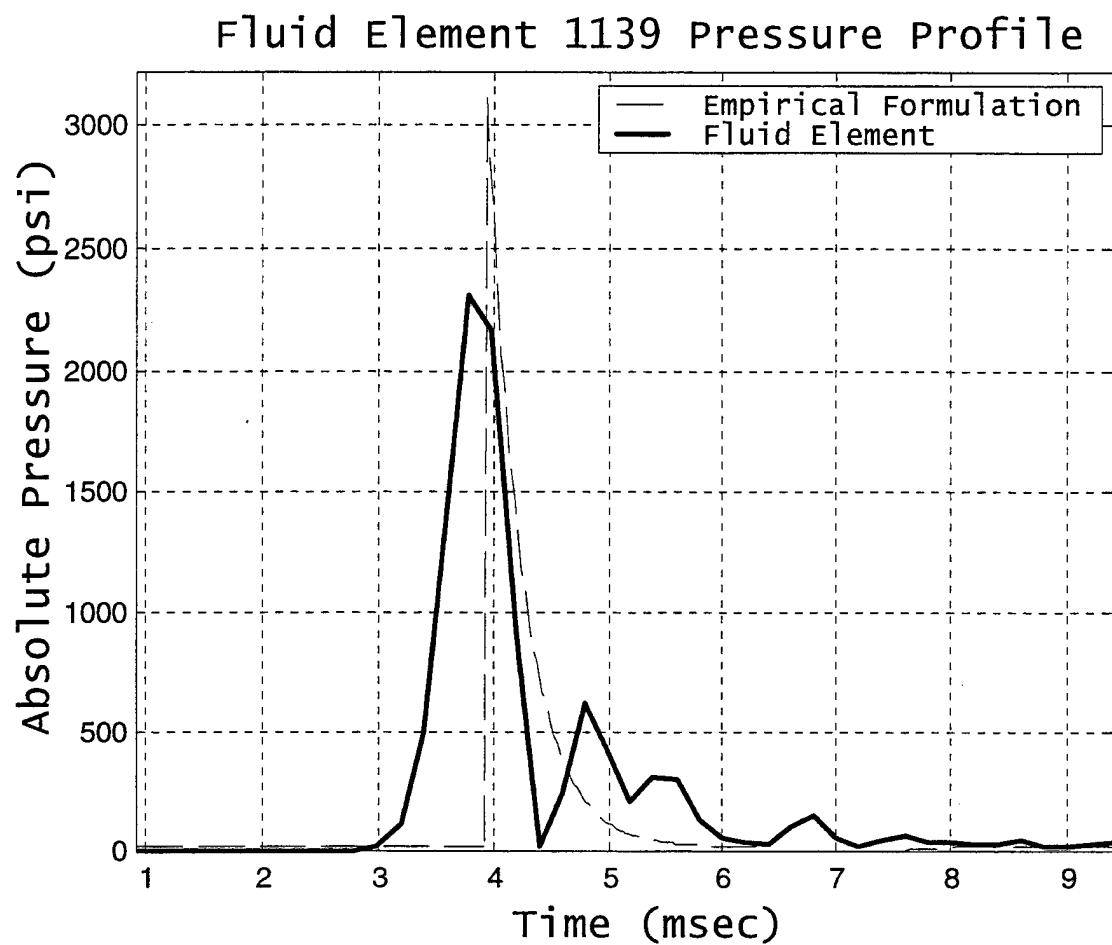
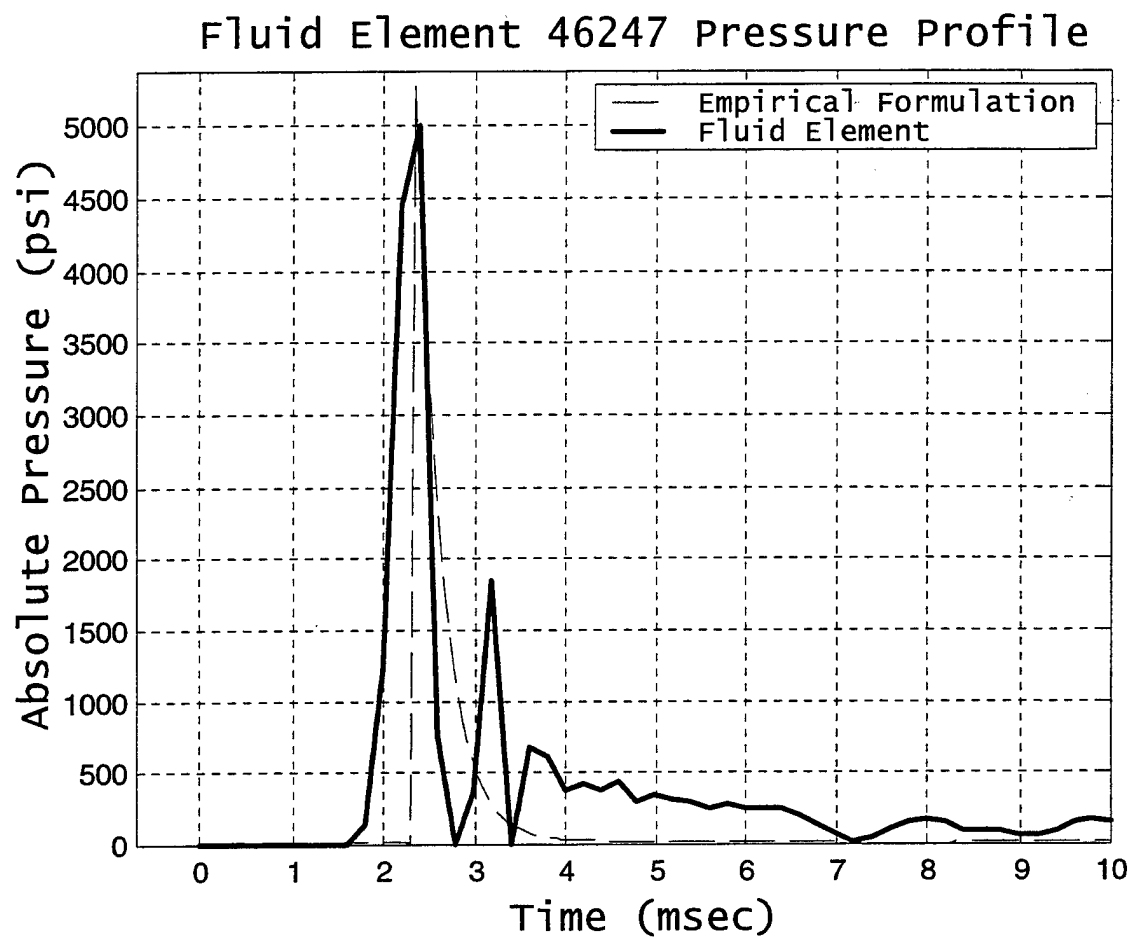


Figure 39. Fluid Element 1128 Pressure Profile
(Rectangular Block Case Along XY Plane)



**Figure 40. Fluid Element 1139 Pressure Profile
(Rectangular Block Case Along XY Plane)**



**Figure 41. Fluid Element 46247 Pressure Profile
(Rectangular Block Case Along XY Plane)**

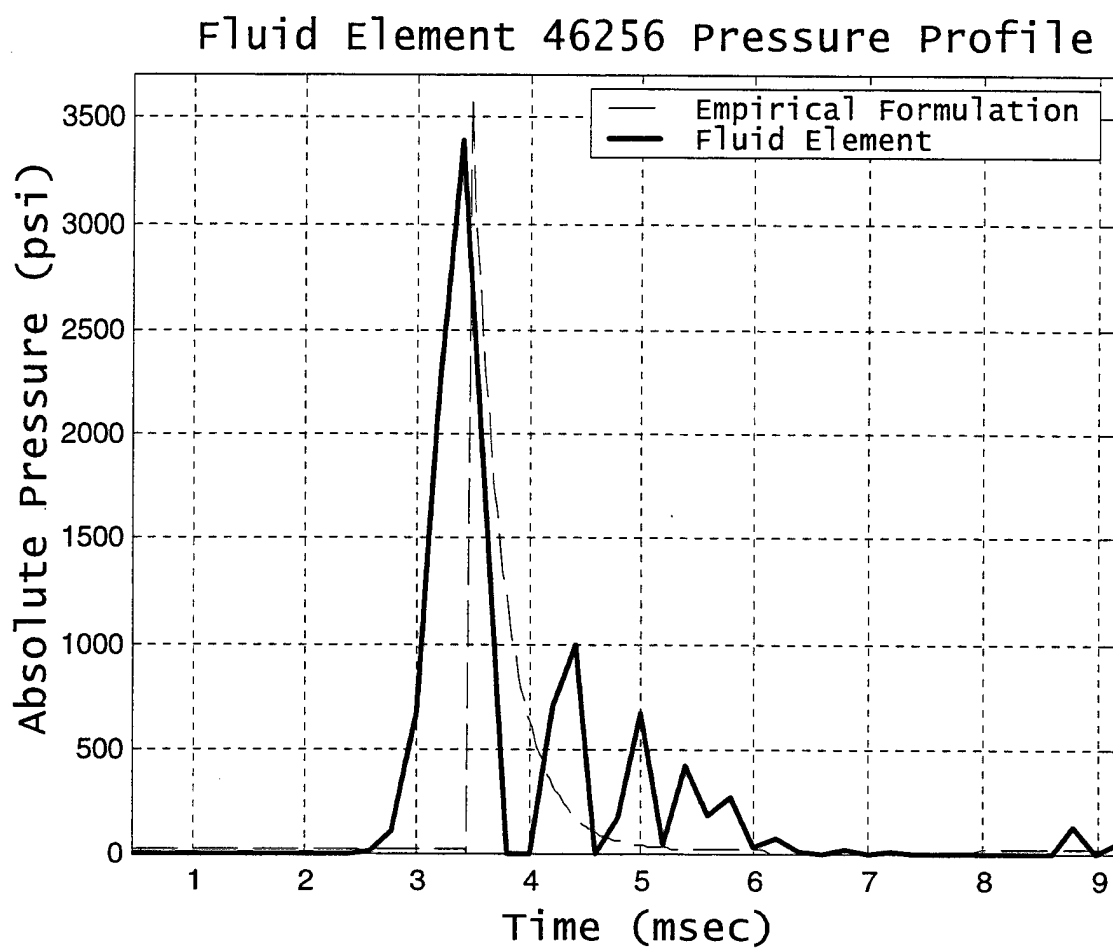


**Figure 42. Fluid Element 46256 Pressure Profile
(Rectangular Block Case Along XY Plane)**

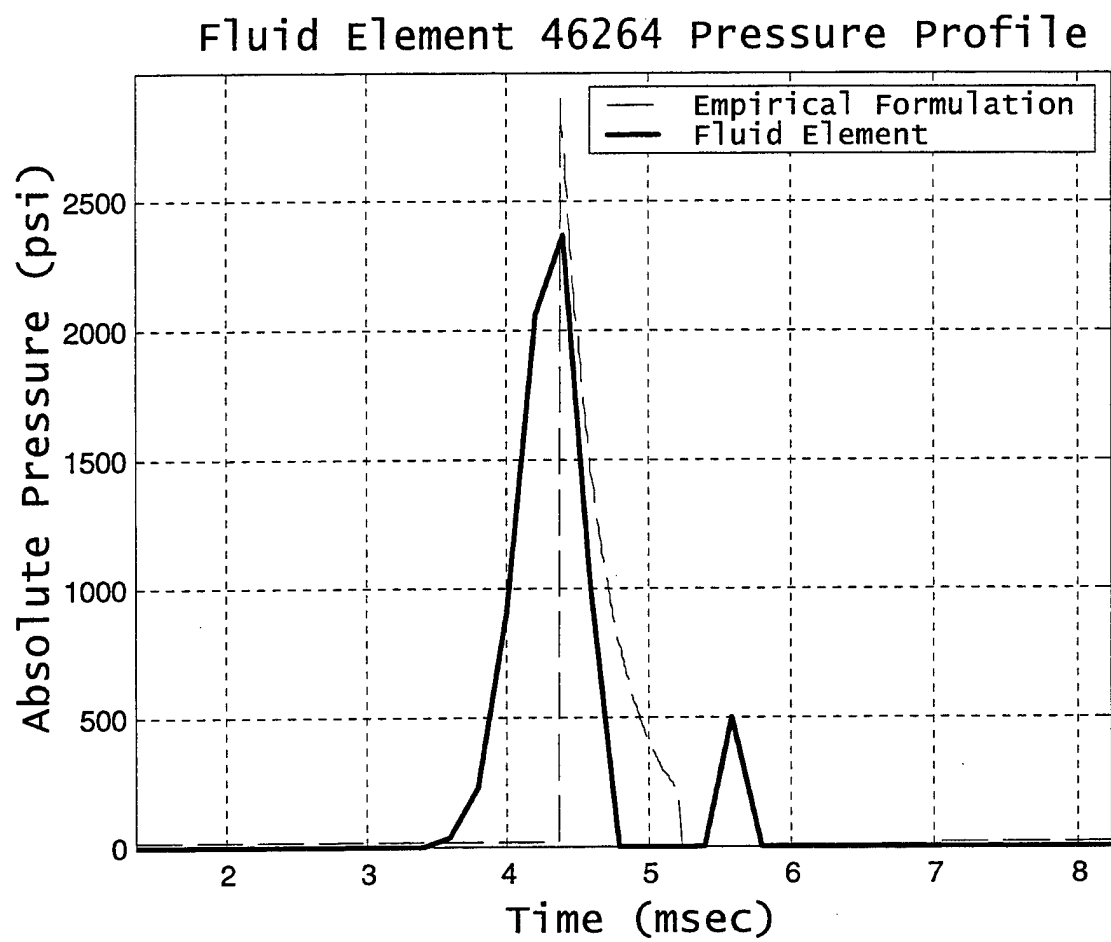
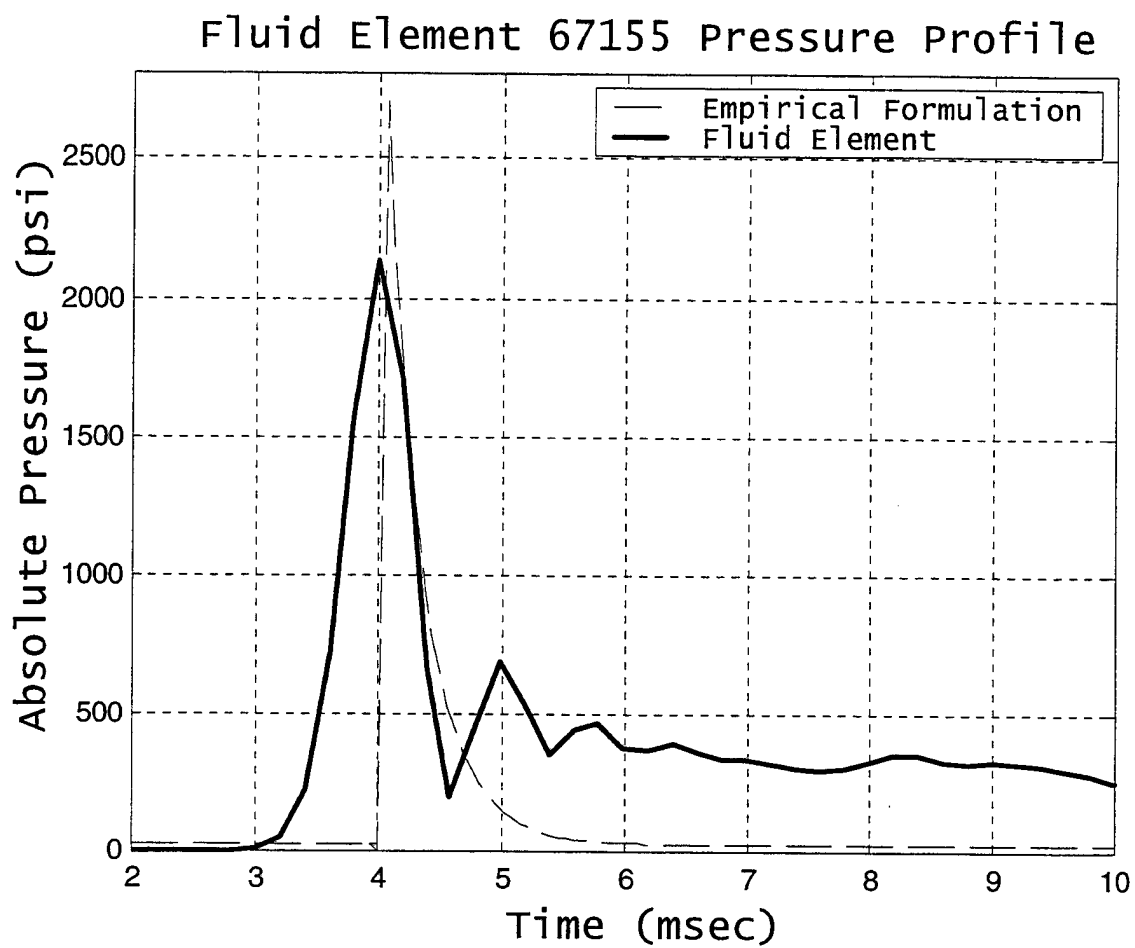


Figure 43. Fluid Element 46264 Pressure Profile
(Rectangular Block Case Along XY Plane)



**Figure 44. Fluid Element 67155 Pressure Profile
(Rectangular Block Case Along NRB 1)**

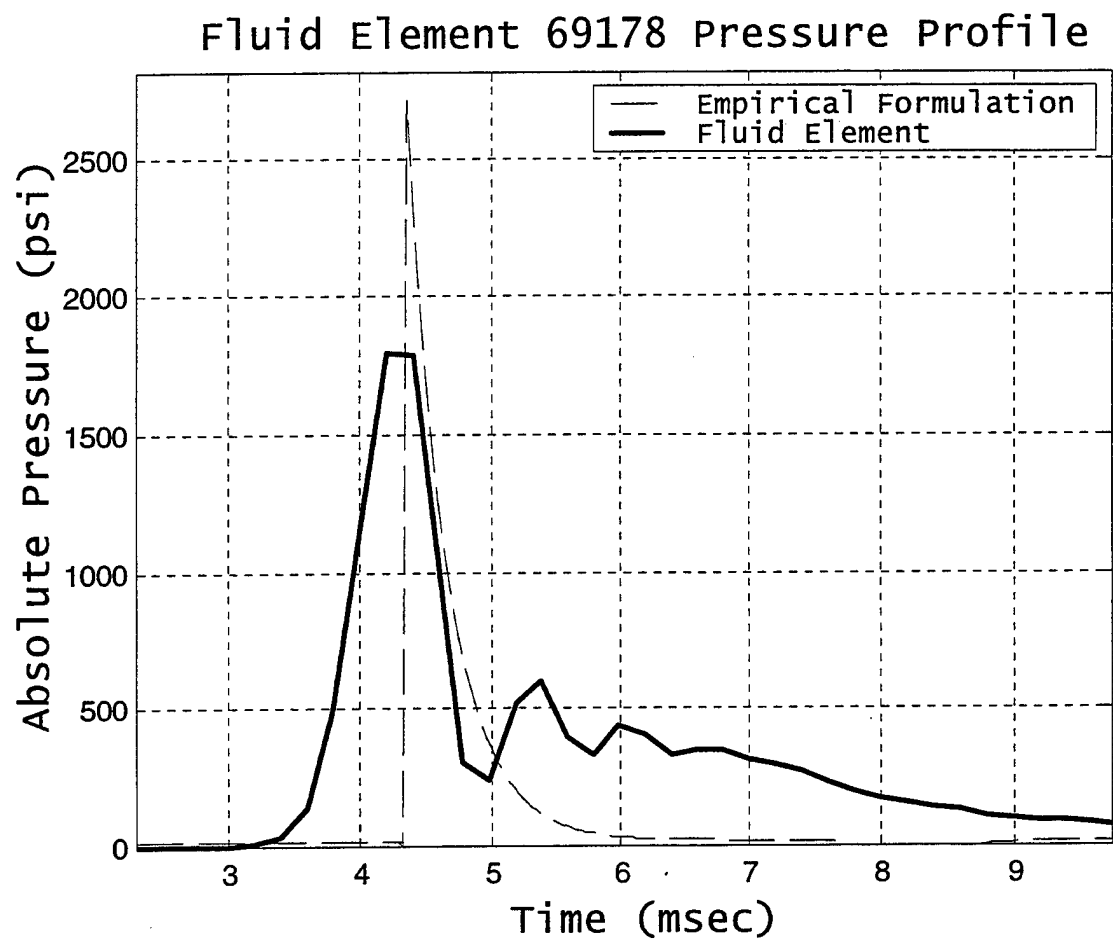


Figure 45. Fluid Element 69178 Pressure Profile
(Rectangular Block Case Along NRB 1)

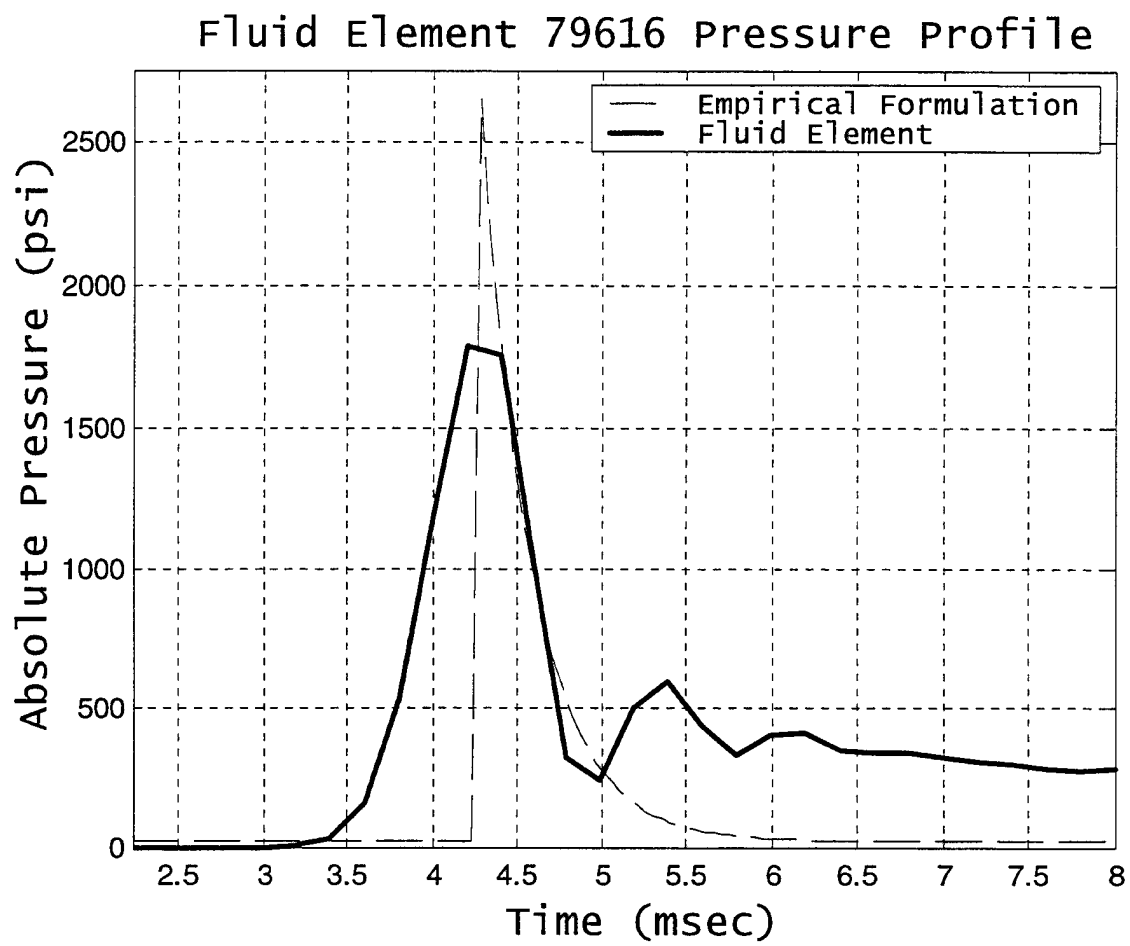


Figure 46. Fluid Element 79616 Pressure Profile
(Rectangular Block Case Along NRB 1)

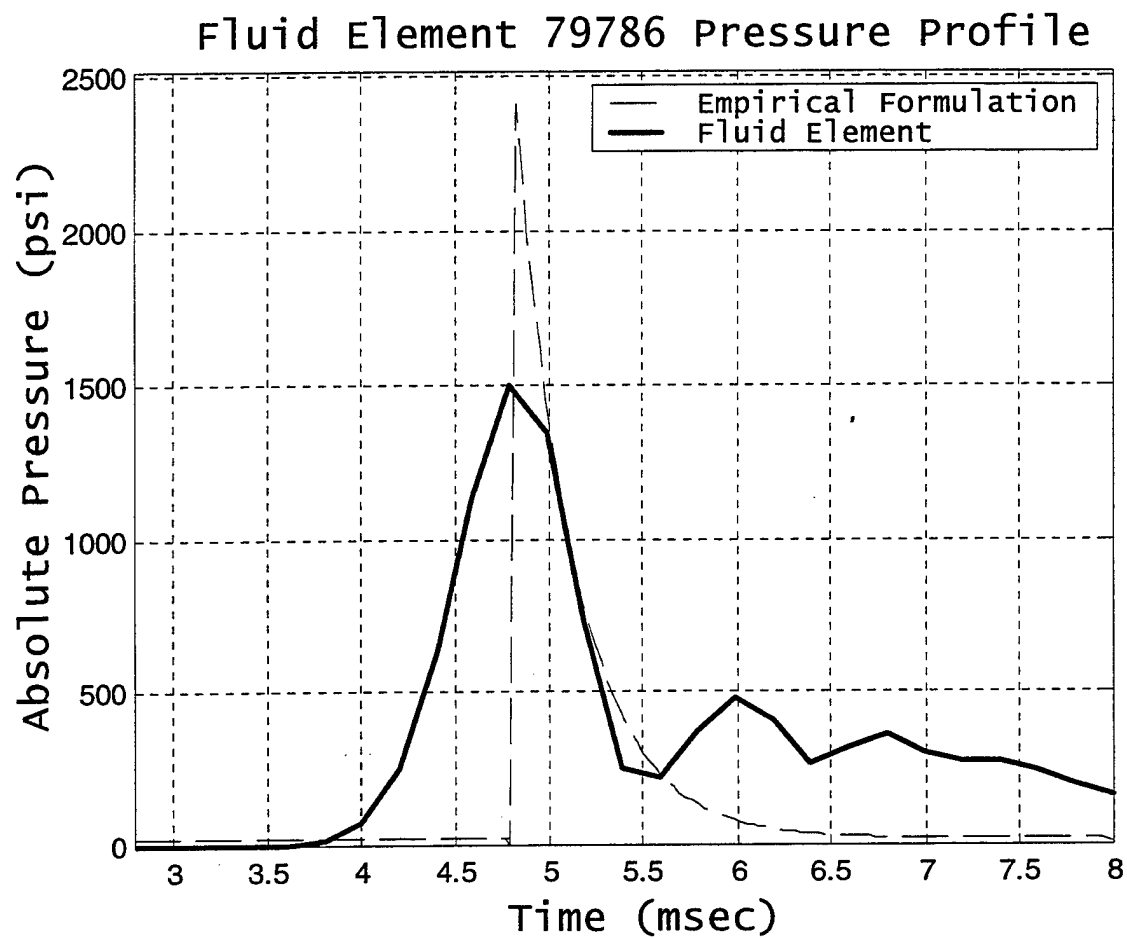


Figure 47. Fluid Element 79786 Pressure Profile
(Rectangular Block Case Along NRB 1)

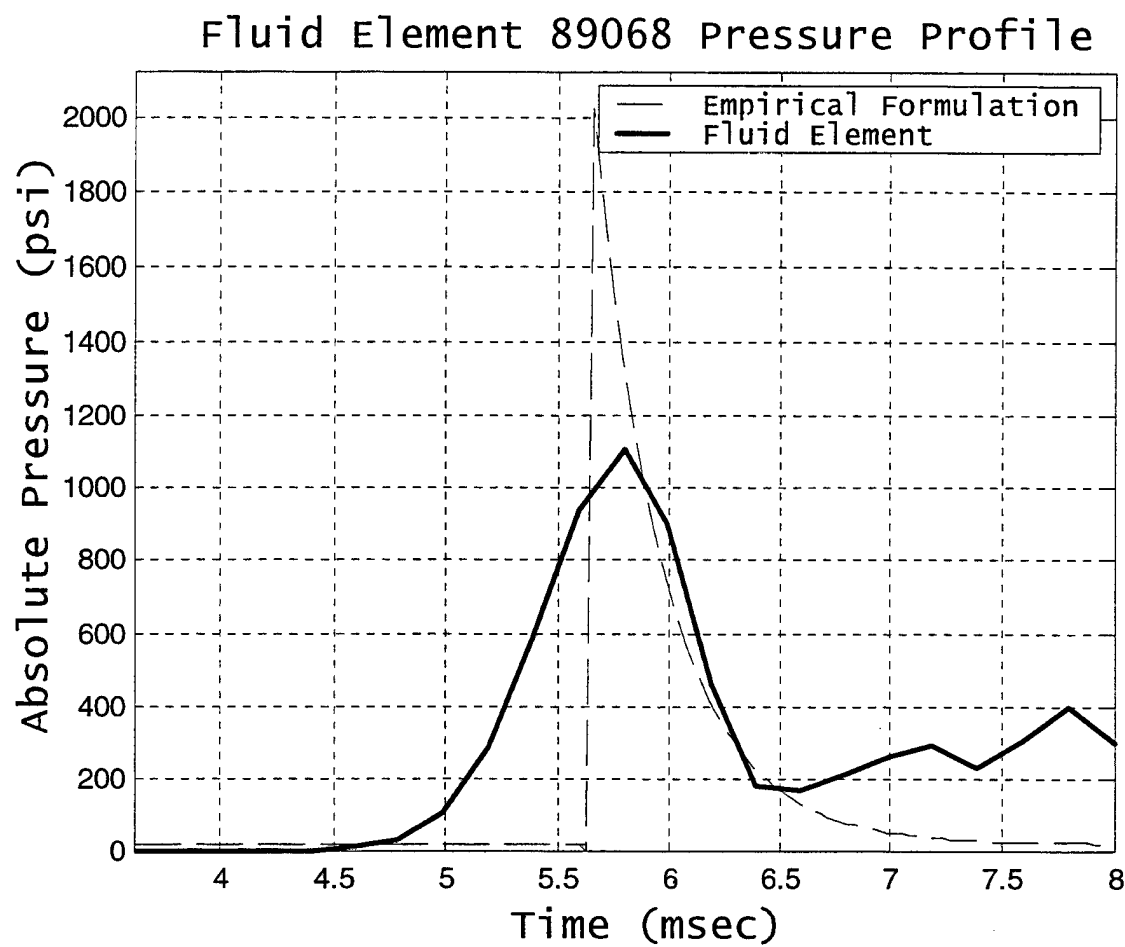


Figure 48. Fluid Element 89068 Pressure Profile
(Rectangular Block Case Along NRB 1)

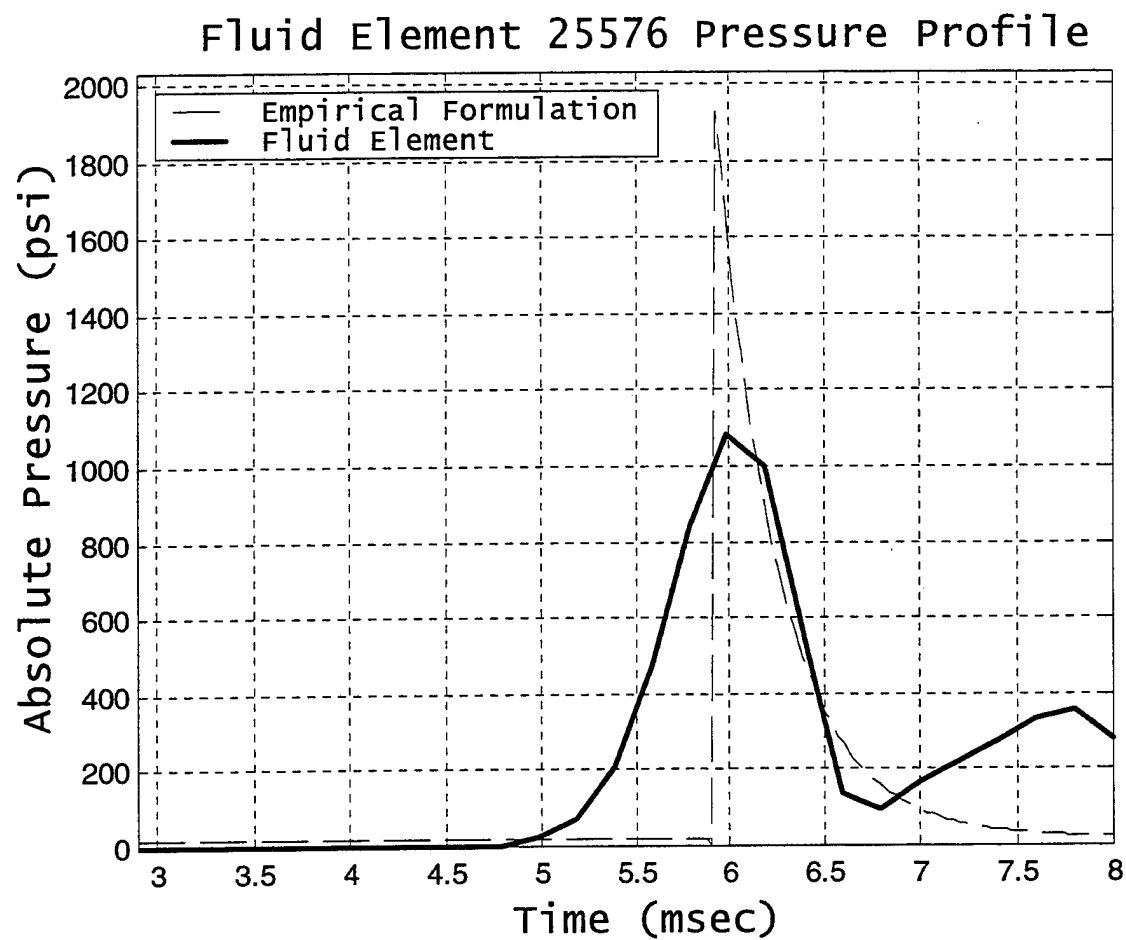
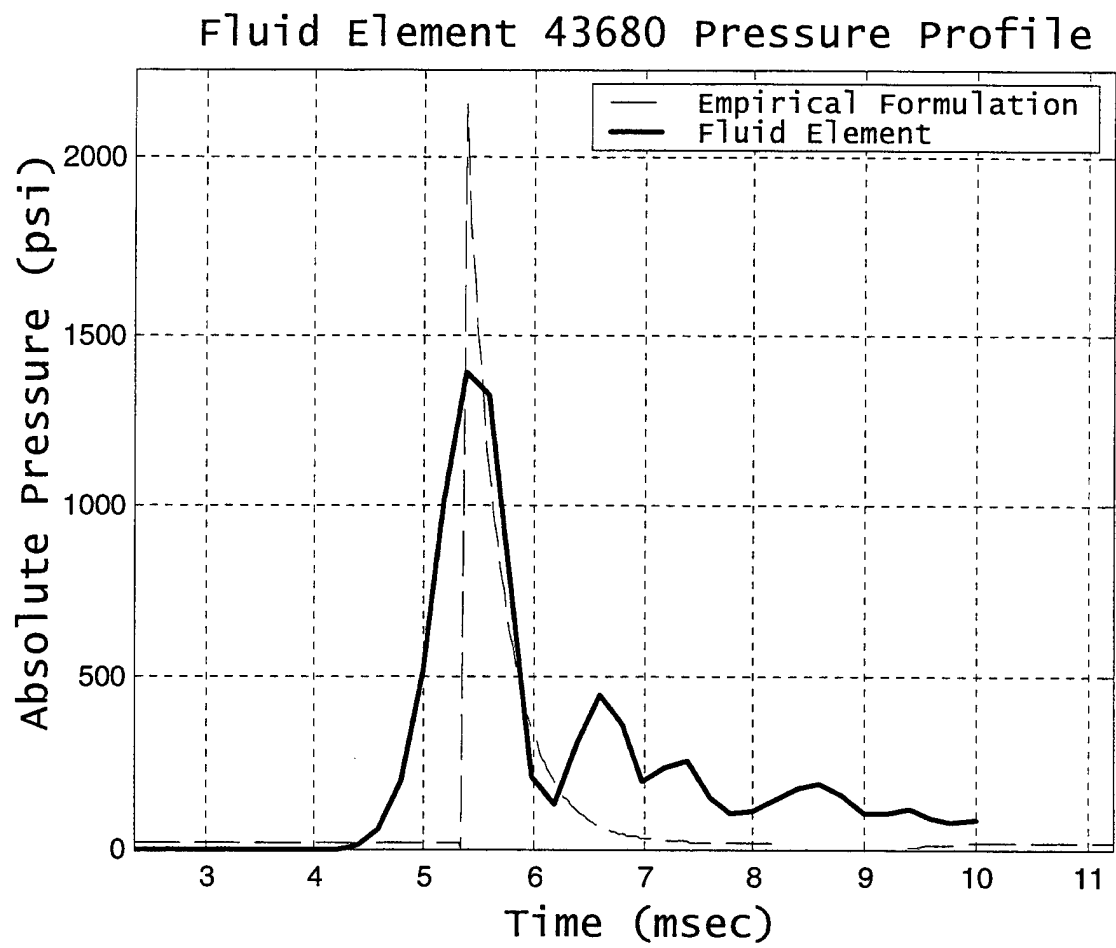
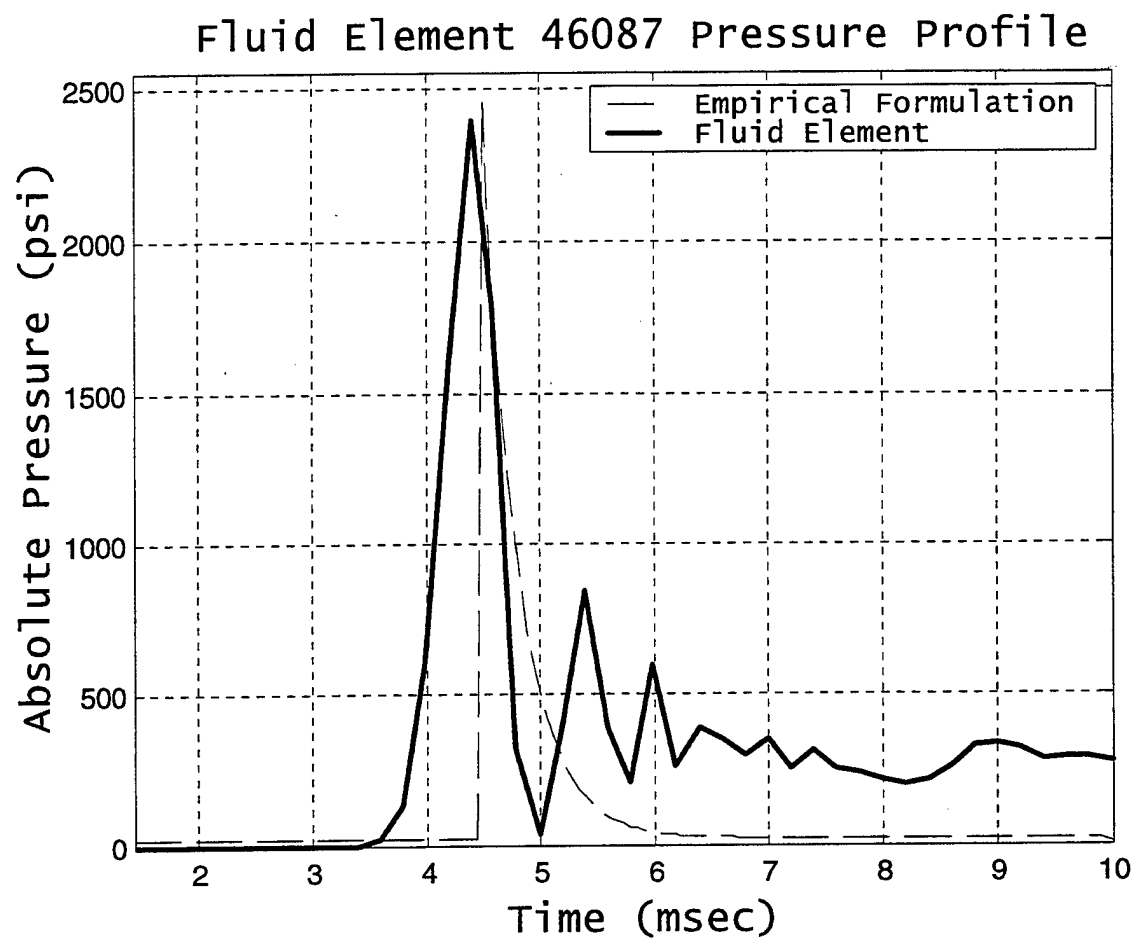


Figure 49. Fluid Element 25576 Pressure Profile
(Rectangular Block Case Along NRB 2)



**Figure 50. Fluid Element 43680 Pressure Profile
(Rectangular Block Case Along NRB 2)**



**Figure 51. Fluid Element 46087 Pressure Profile
(Rectangular Block Case Along NRB 2)**

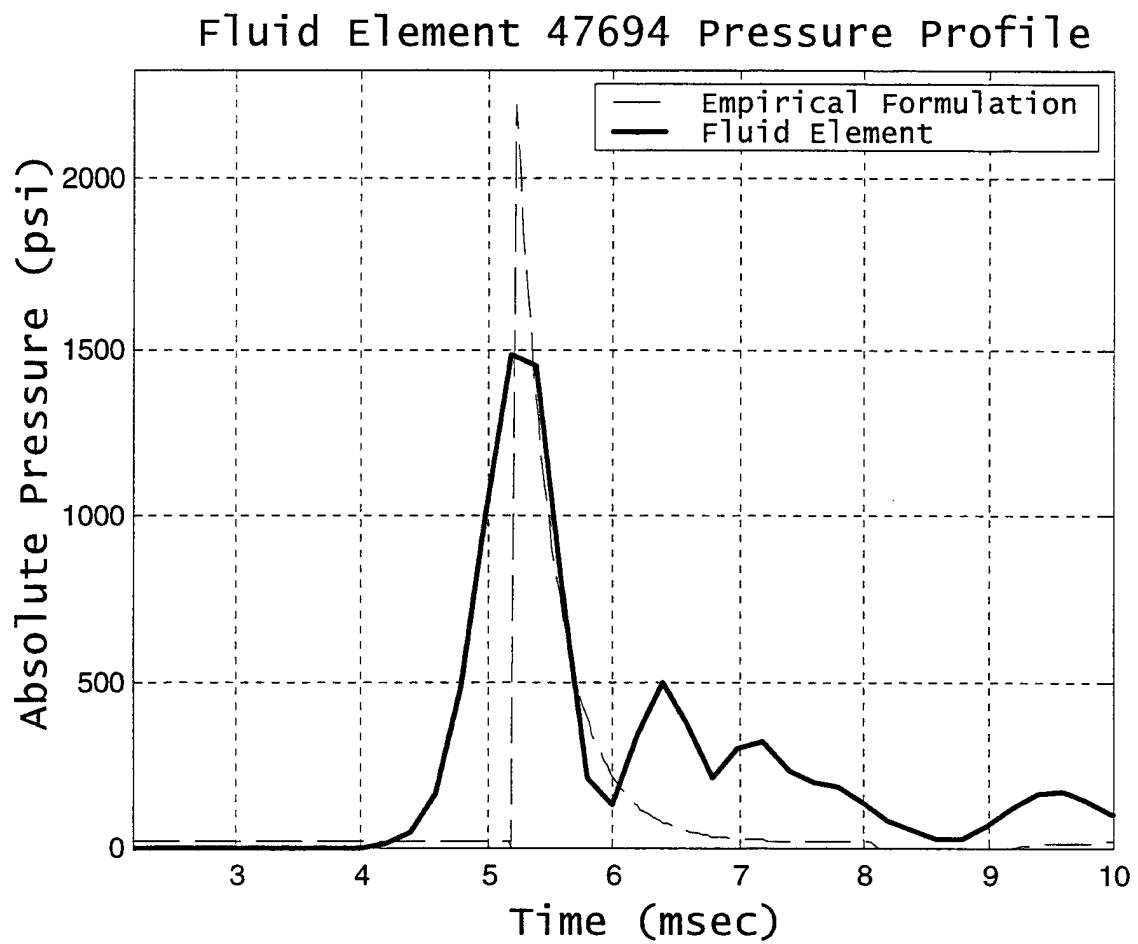


**Figure 52. Fluid Element 47694 Pressure Profile
(Rectangular Block Case Along NRB 2)**

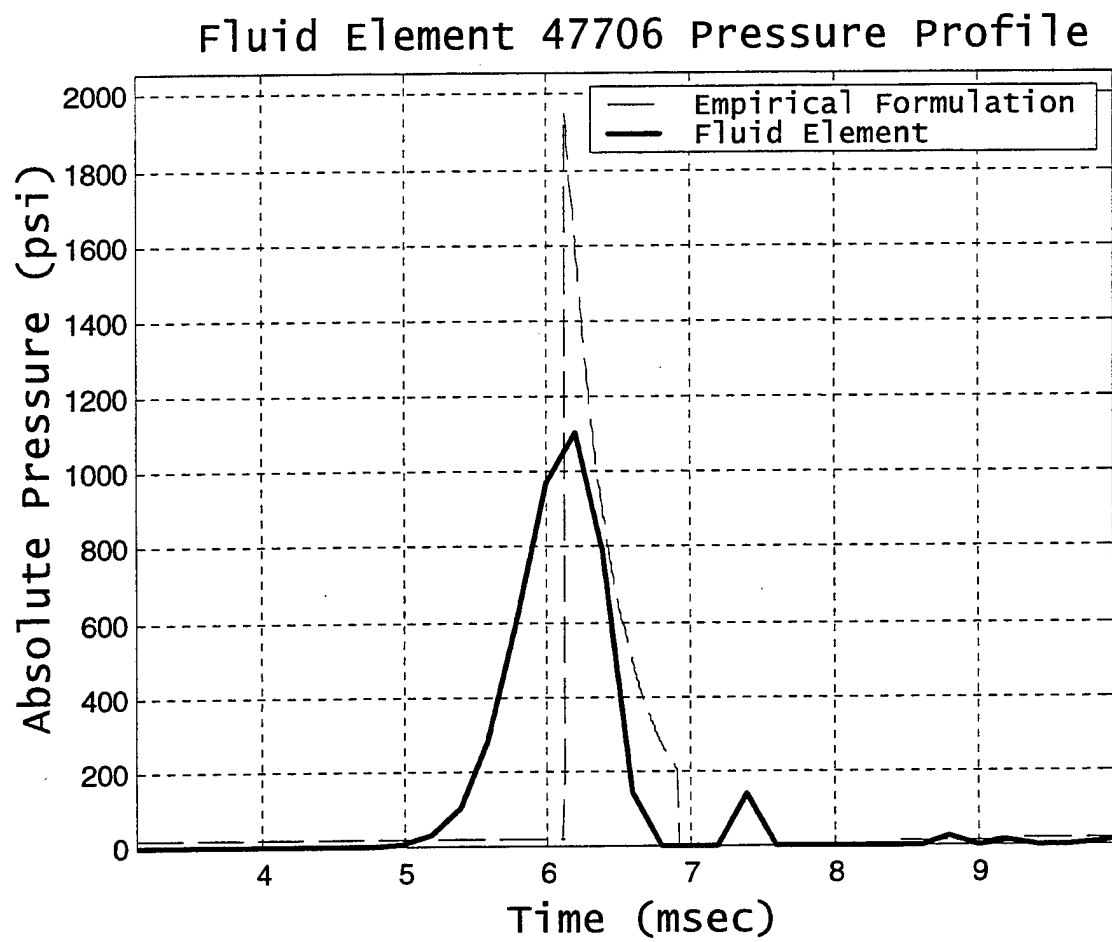
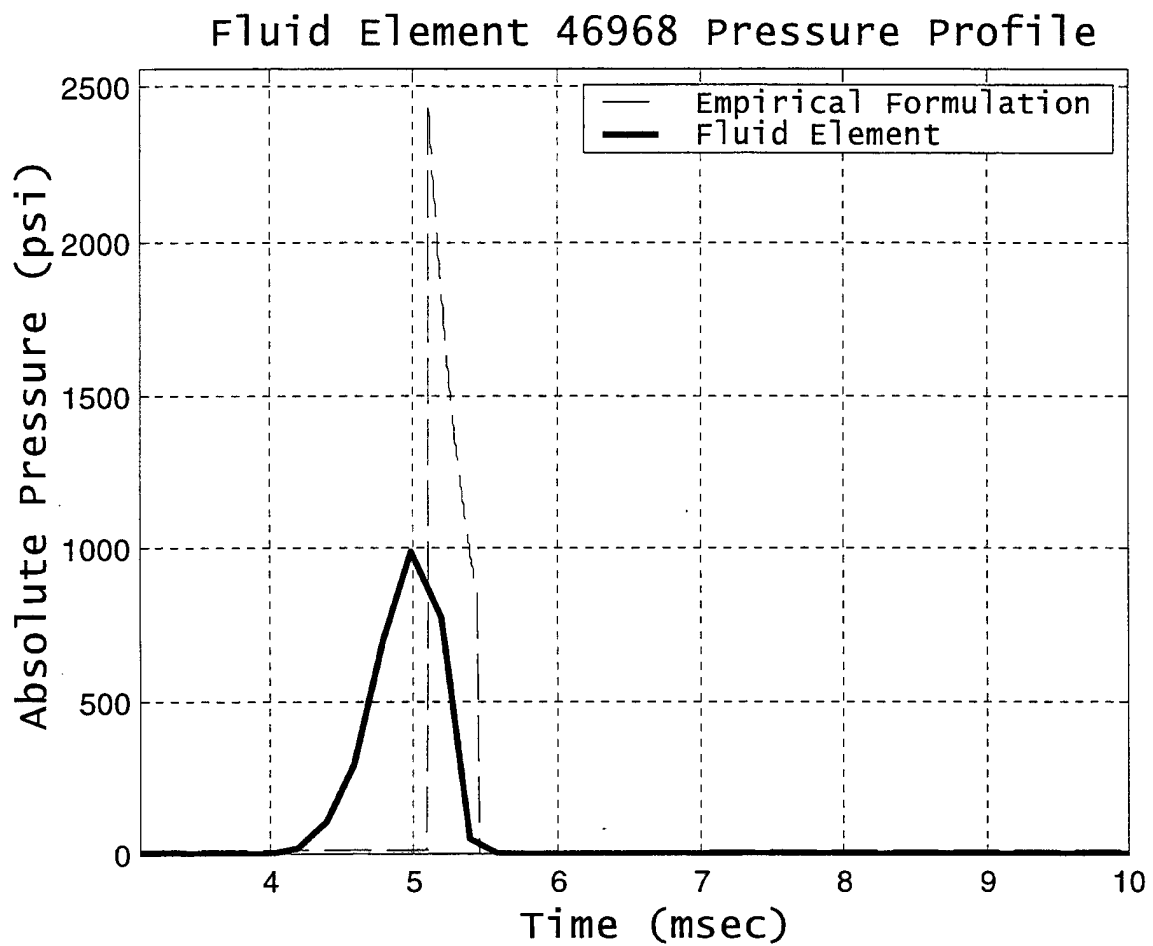


Figure 53. Fluid Element 47706 Pressure Profile
(Rectangular Block Case Along NRB 2)



**Figure 54. Fluid Element 46968 Pressure Profile
(Rectangular Box Case Underneath Barge)**

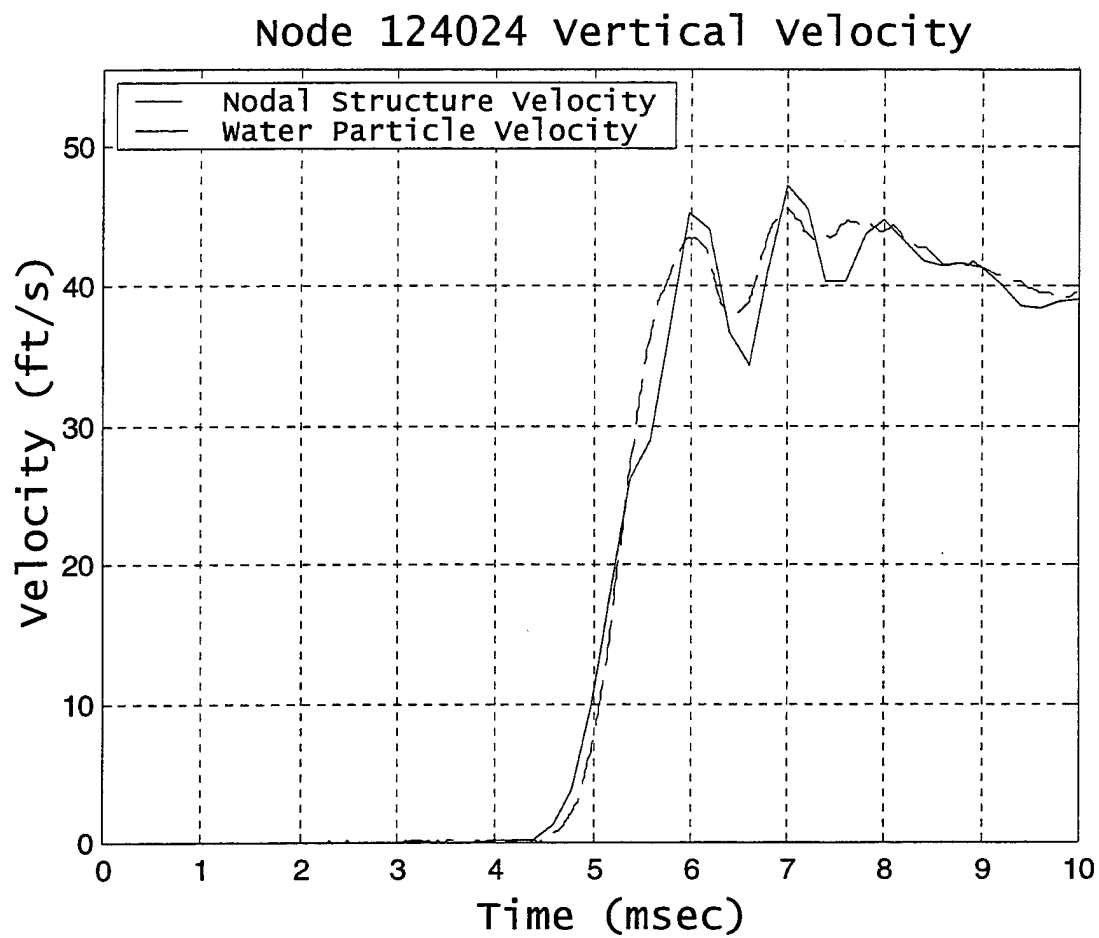


Figure 55. Velocity Response at Nodes 124024/16862

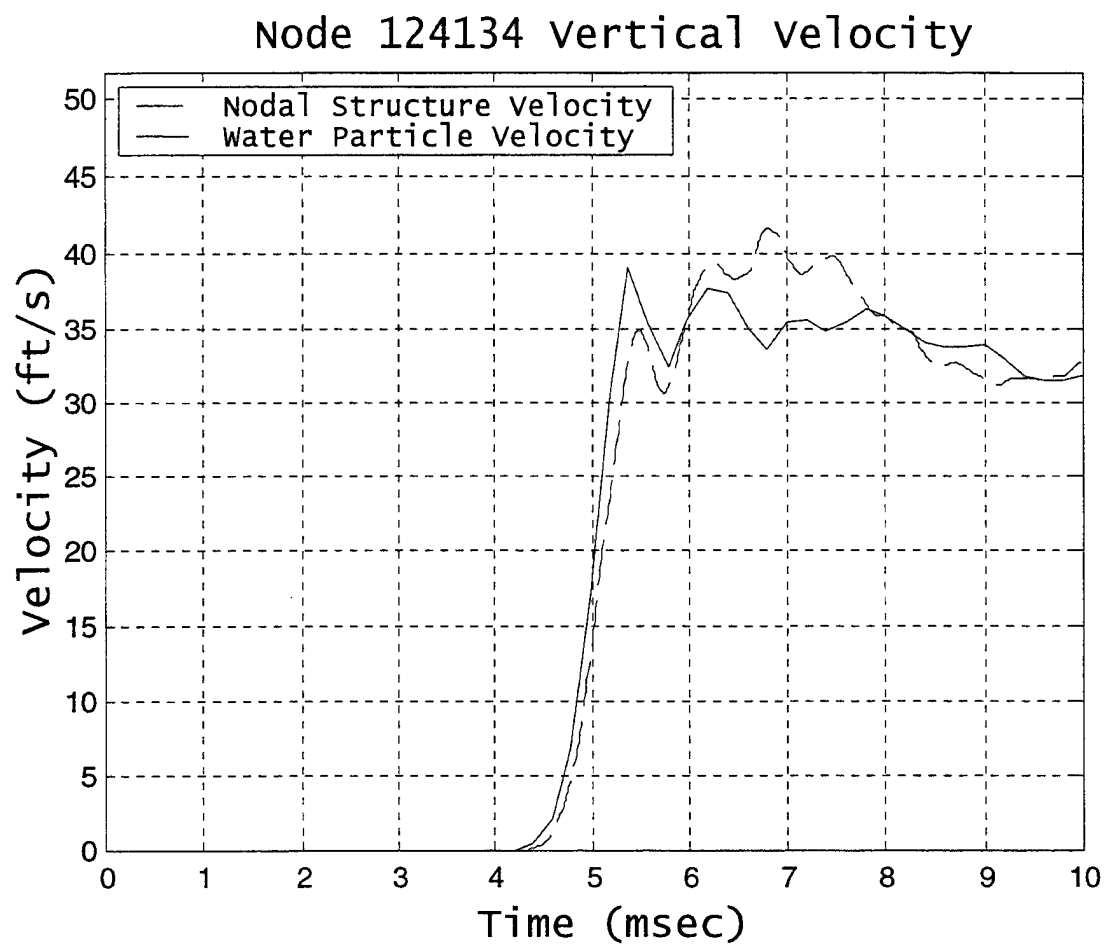


Figure 56. Velocity Response at Nodes 124134/39870

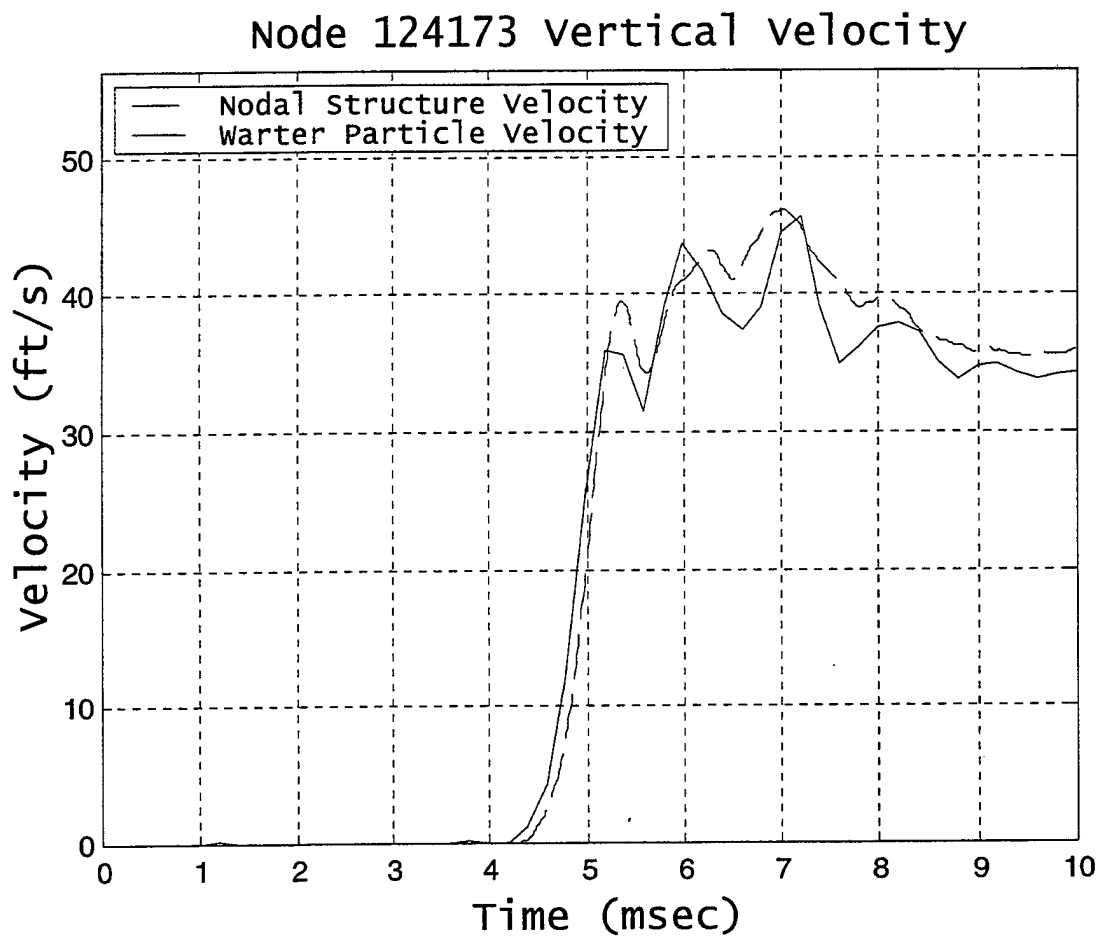


Figure 57. Velocity Response at Nodes 124173/39868

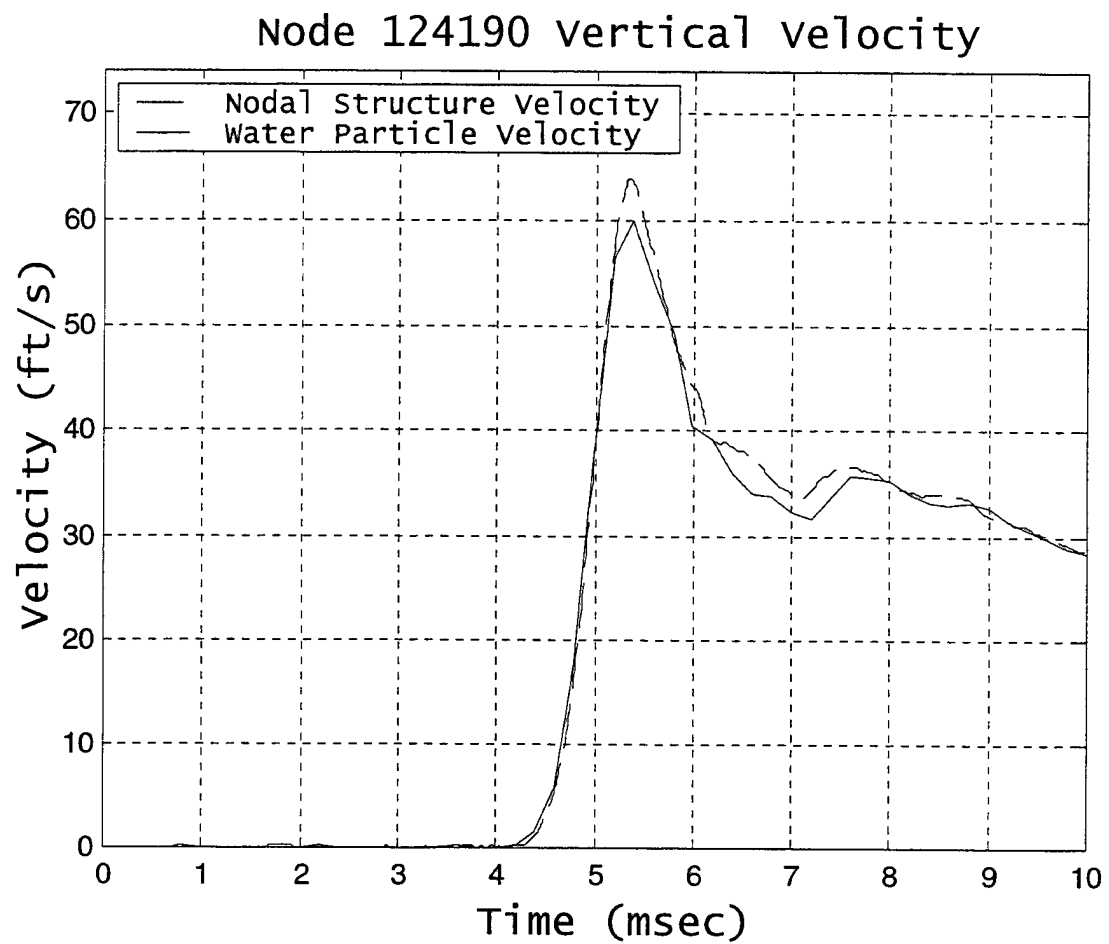


Figure 58. Velocity Response at Nodes 124190/40492

2. Stair Explosive Simulation

In the stair explosive simulation, sixteen solid fluid elements were used for comparison. Along the X-Y plane, nodes 3277, 3290, 73350, 73360, and 73370 were examined. Along NRB 1 plane, nodes 105852, 112932, 126792, 127012, and 141092 were compared to the empirical formulations. And along the NRB 2 plane, nodes 40981, 40981, 75223, 75245, and 75261 were used for comparison. The last fluid element involved 74296 was located underneath the barge's centerline approximately. Figures 59 through 74 illustrate the agreeable numerical and empirical pressure results. Tables 8 through 10 compare the results in maximum peak pressure, P_{\max} , between the empirical and numerical formulations. The maximum pressures in this charge model are more agreeable than in the previous case. This is due to modeling the charge as close to a sphere than in the previous case of the rectangular box. The shock pressure appears to travel more like a spherical wave because of the stair charge geometry.

Cavitation can also be observed in several nodes, namely nodes 73370, 75261, and 74296, which were at depths of 2.3 ft, 2.5 ft, and 1.0 ft respectively. The mentioned nodes at their respective depths were well within the cavitation zone and were in agreement with Figure 28. The other nodes were outside of the cavitation region. As expected, the water particle velocities at the fluid-air boundary behaved principally in a vertical manner due to the bulk cavitation. Additionally, the air pressure near the vicinity of the fluid-air boundary experienced little or no relative change in pressure as predicted.

The structural nodes 195304, 195411, 195450, and 195467 correspond to the following fluid nodes, respectively, 26928, 61952, 61950, and 62654. In some instances, the structural node location did not match up exactly with the fluid node location, so the closest fluid node was chosen. Figures 75 through 78 illustrate the rapidly increasing vertical velocities (approximately 5 to 6 msec) to a peak value and then a rapid decrease and increase in a series of steps until the response settles down. The response does not settle out at a value of zero due to rigid body motion of the structure. Damping effects are also present as in the previous case.

In the rectangular box charge model, a total of 1 hour, 45 minutes was required for the simulation to complete its numerical computations. A time scale factor of 0.67 was used in both simulation runs. The average time step was 12.5 μ sec for 10 msec of data. In the stair charge model, a total of 2 hours, 50 minutes was required to run the simulation. The average time step was 12.5 μ sec for 10 msec of data. Although LS-DYNA has the capability to run parallel processing, the option was not available for this numerical processing technique during the time of the experimentation. Once the parallel processing is fully incorporated in this ALE technique, the processing time will be significantly reduced.

Overall, a good agreement in pressure signature shows the ALE technique is capable of handling the underwater explosion problem. A confidence in the numerical procedure has been established for this underwater explosion problem. A shift in the emphasis will now be focused on the two-dimensional air explosion problem interacting with a structural plate.

Node	Numerical Result P_{\max} (psi)	Empirical Result P_{\max} (psi)	% Error
3277	2147.1	2595.5	17.3
3290	2964.9	3240.4	8.5
73350	6417.0	5280.1	21.5
73360	3798.2	3740.5	1.5
73370	2588.4	2912.0	11.1

Table 8. Stair Case Results: Nodes Along X-Y Plane

Node	Numerical Result P_{\max} (psi)	Empirical Result P_{\max} (psi)	% Error
105852	2565.0	2693.3	4.8
112932	2277.4	2705.7	15.8
126792	2204.1	2643.8	16.6
127012	1790.1	2445.9	26.8
141092	1261.2	2012.5	37.3

Table 9. Stair Case Results: Nodes Along NRB 1

Node	Numerical Result P_{\max} (psi)	Empirical Result P_{\max} (psi)	% Error
40981	1380.2	1937.7	28.8
40993	1700.3	2135.1	20.4
75223	2797.5	2453.7	14.0
75245	1814.2	2231.7	18.8
75261	1275.7	1948.7	34.5

Table 10: Stair Case Results: Nodes Along NRB 2

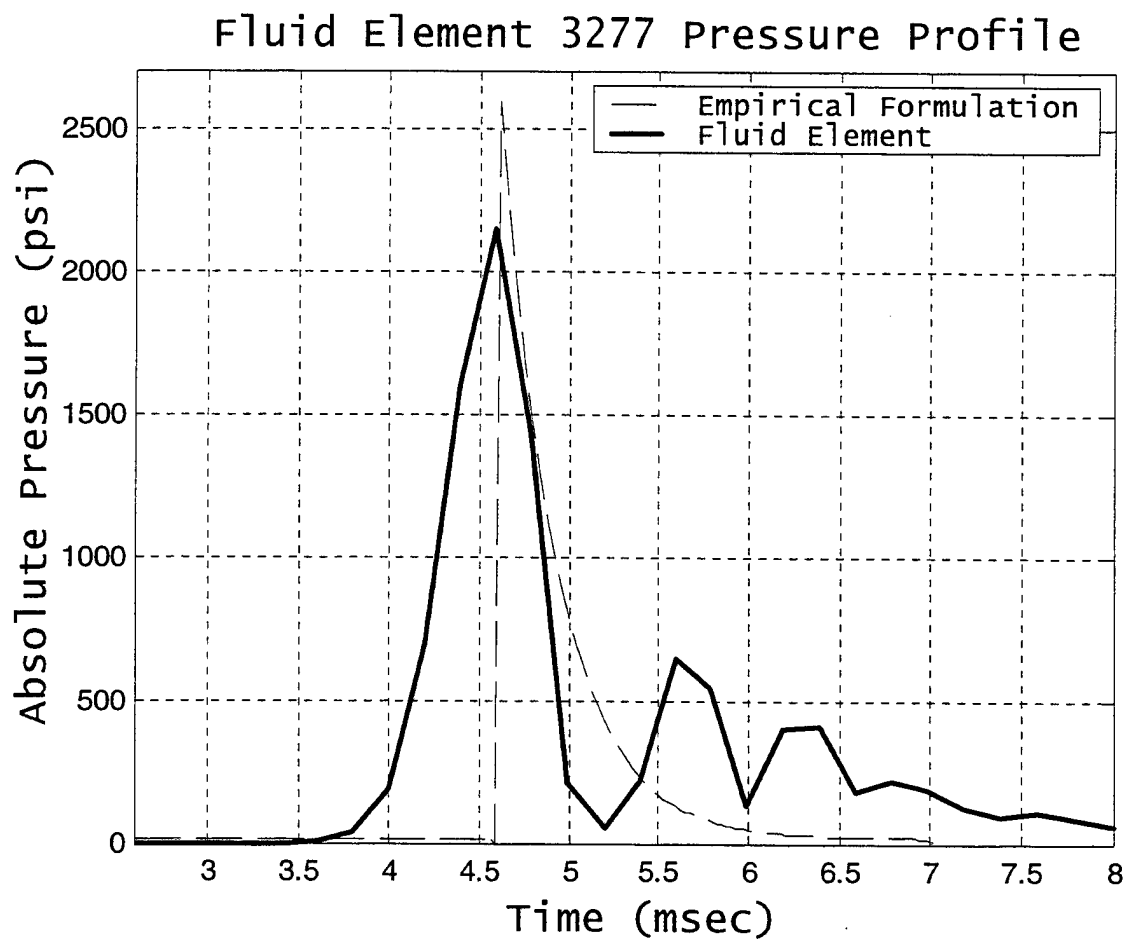


Figure 59. Fluid Element 3277 Pressure Profile
(Stair Case Along XY Plane)

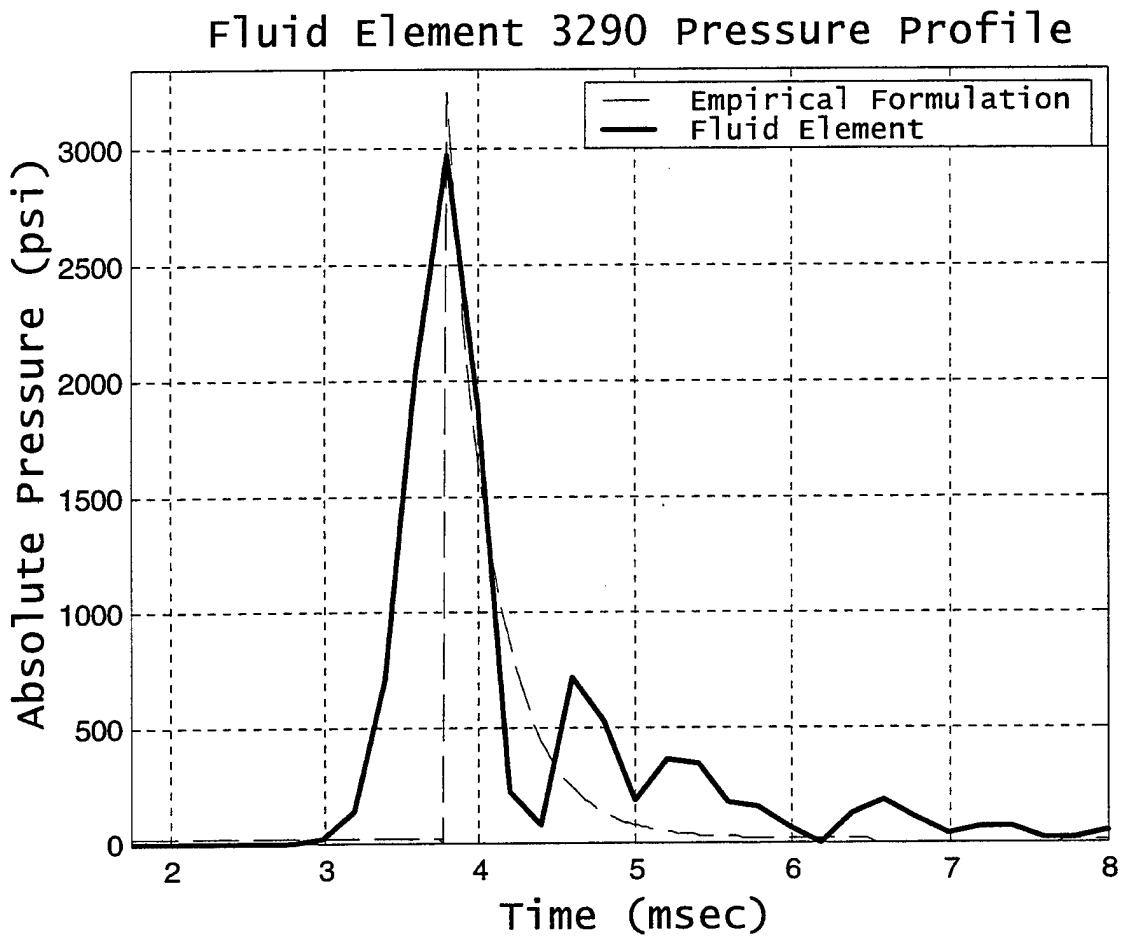
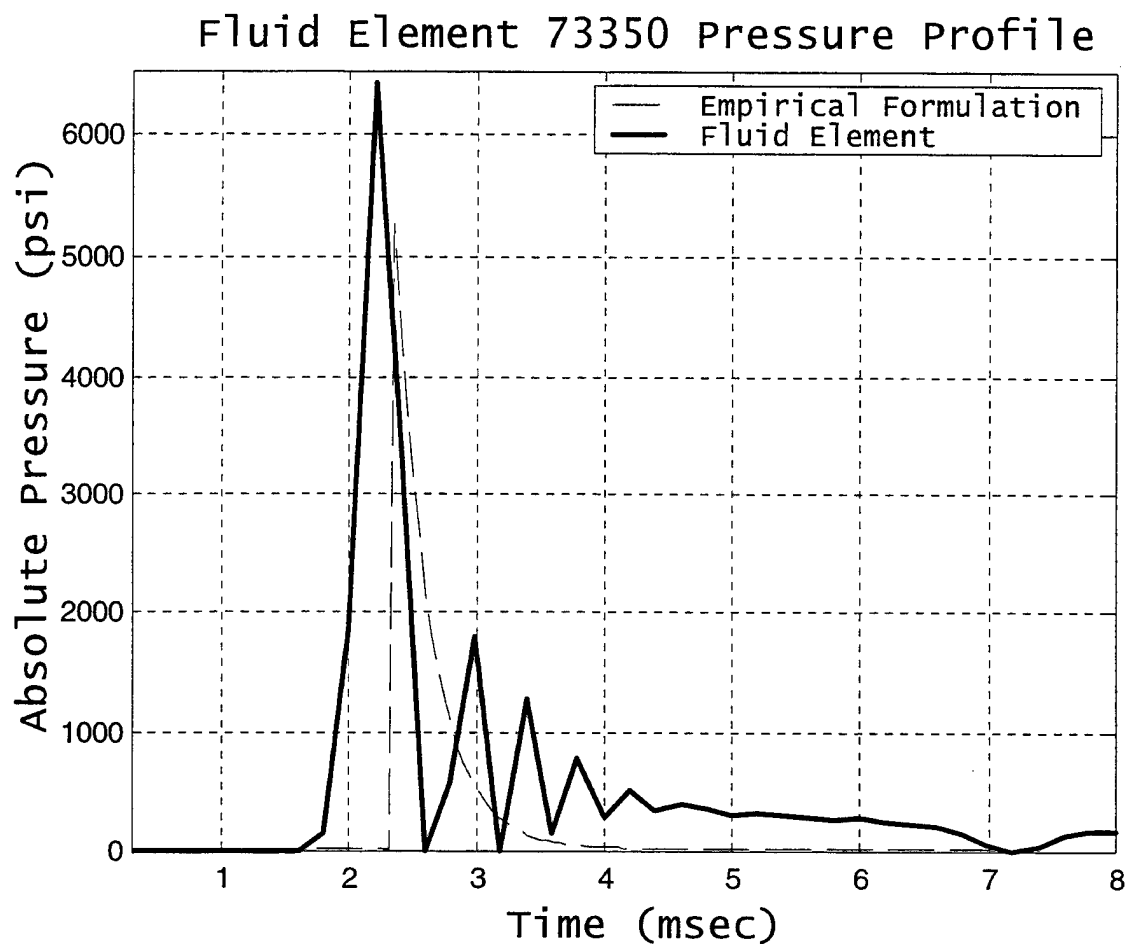


Figure 60. Fluid Element 3290 Pressure Profile
(Stair Case Along XY Plane)



**Figure 61. Fluid Element 73350 Pressure Profile
(Stair Case Along XY Plane)**

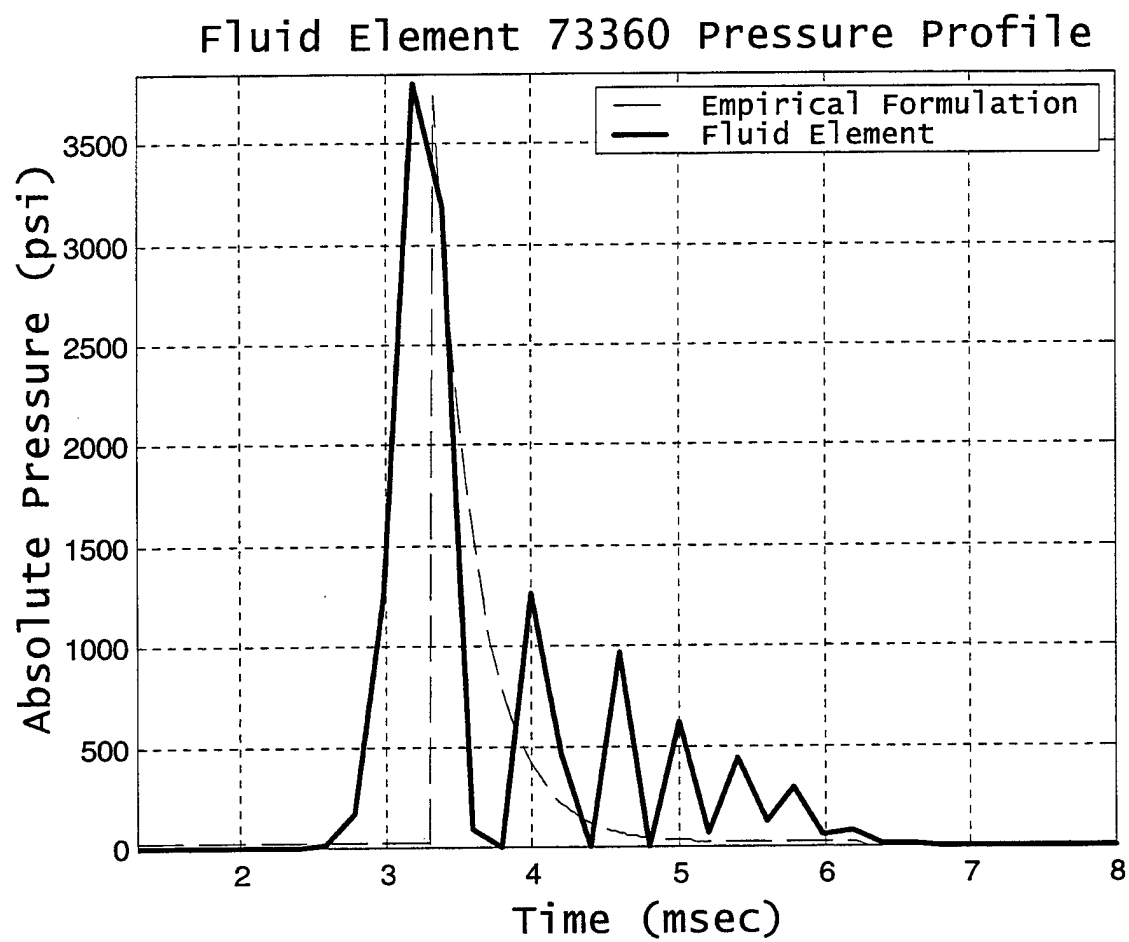


Figure 62. Fluid Element 73360 Pressure Profile
(Stair Case Along XY Plane)

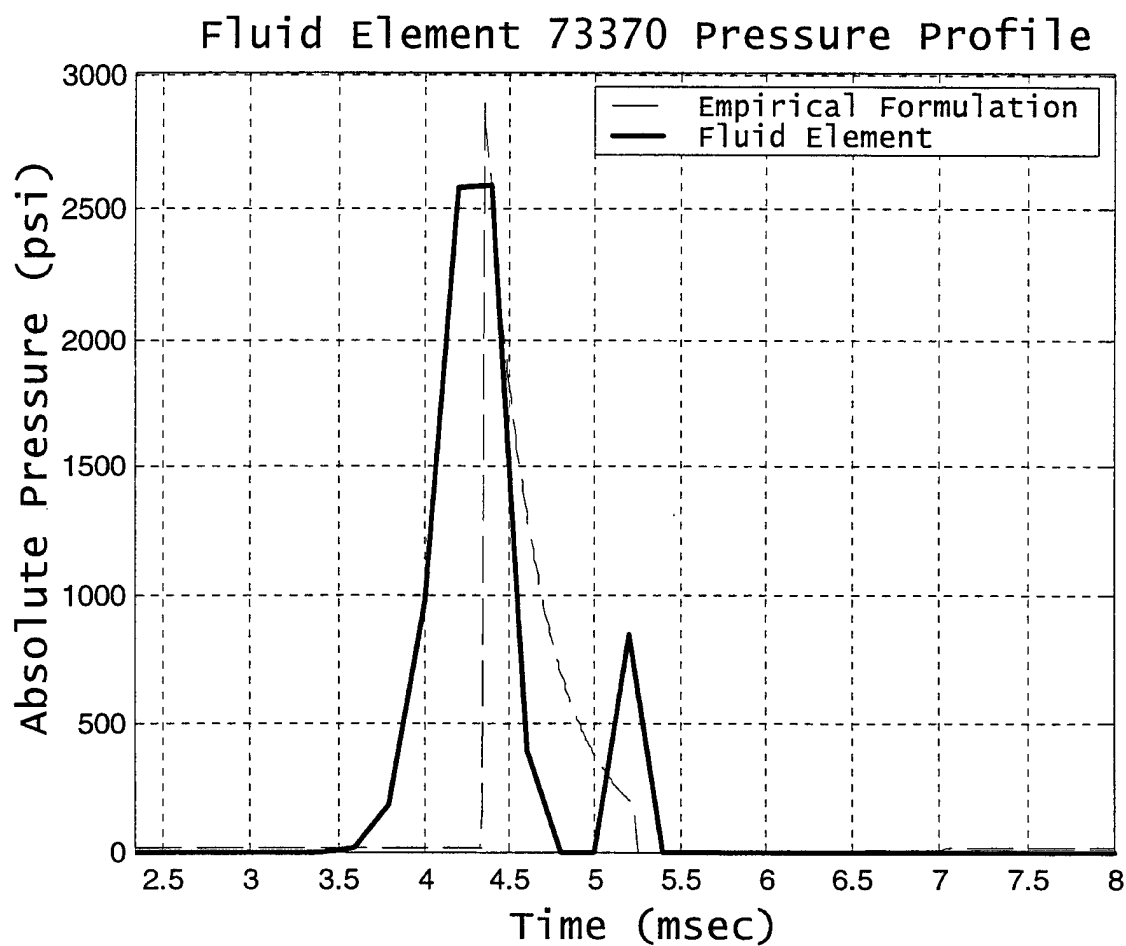


Figure 63. Fluid Element 73370 Pressure Profile
(Stair Case Along XY Plane)

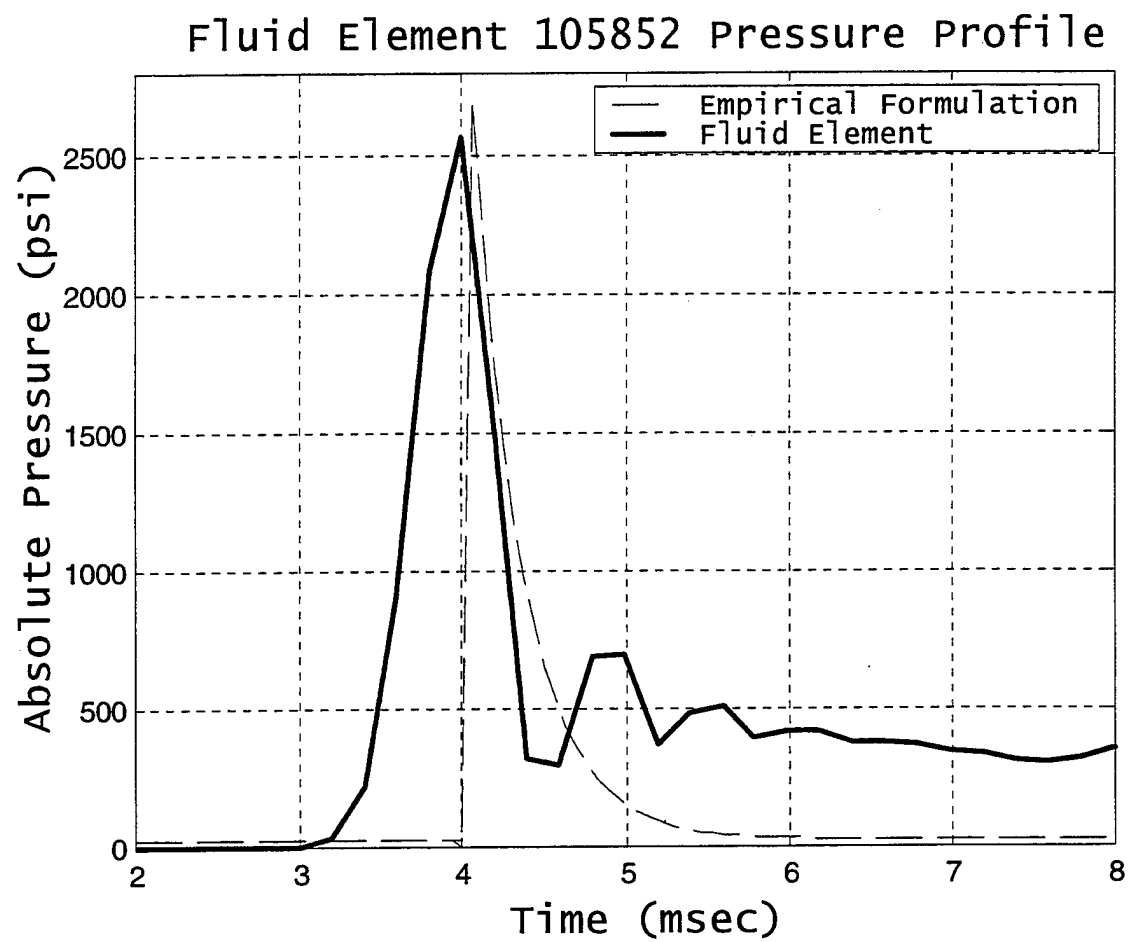


Figure 64. Fluid Element 105852 Pressure Profile
(Stair Case Along NRB 1)

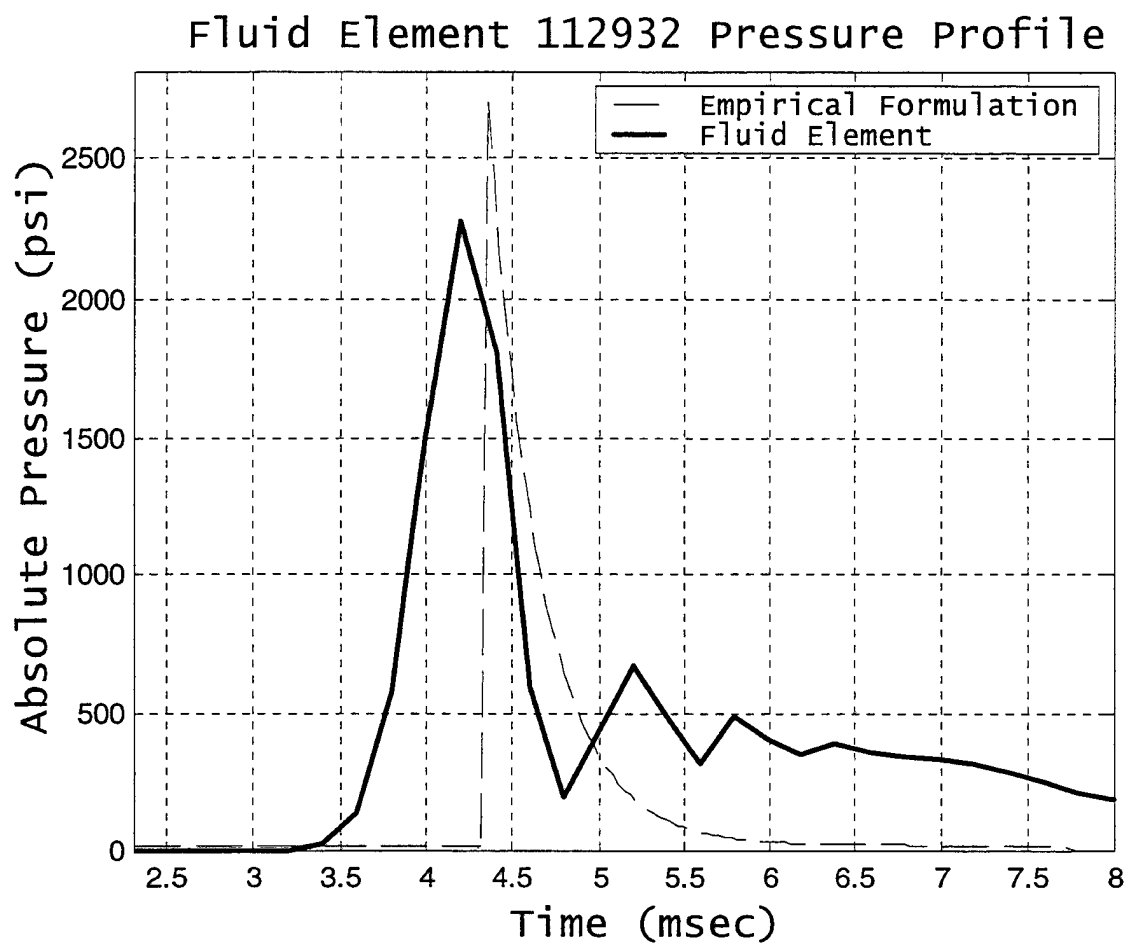


Figure 65. Fluid Element 112932 Pressure Profile
(Stair Case Along NRB 1)

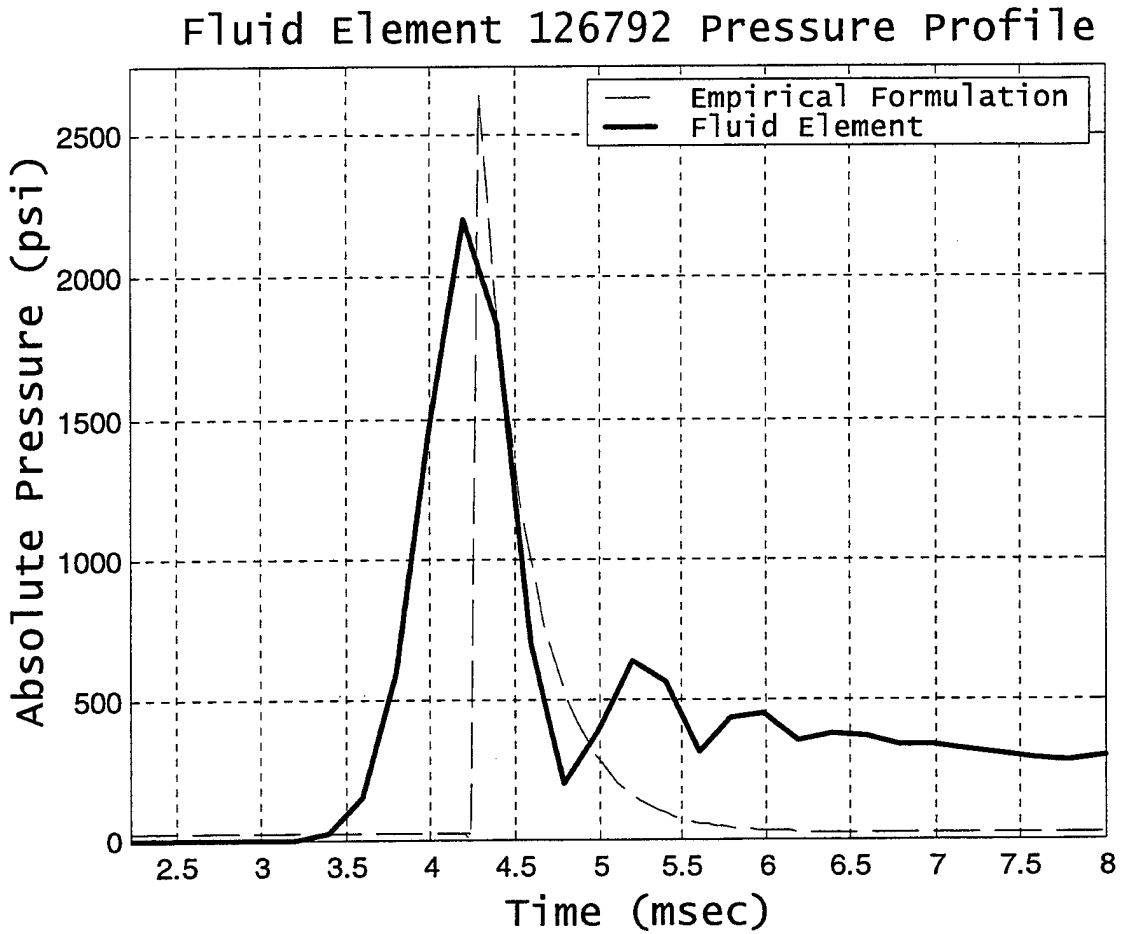


Figure 66. Fluid Element 126792 Pressure Profile
(Stair Case Along NRB 1)

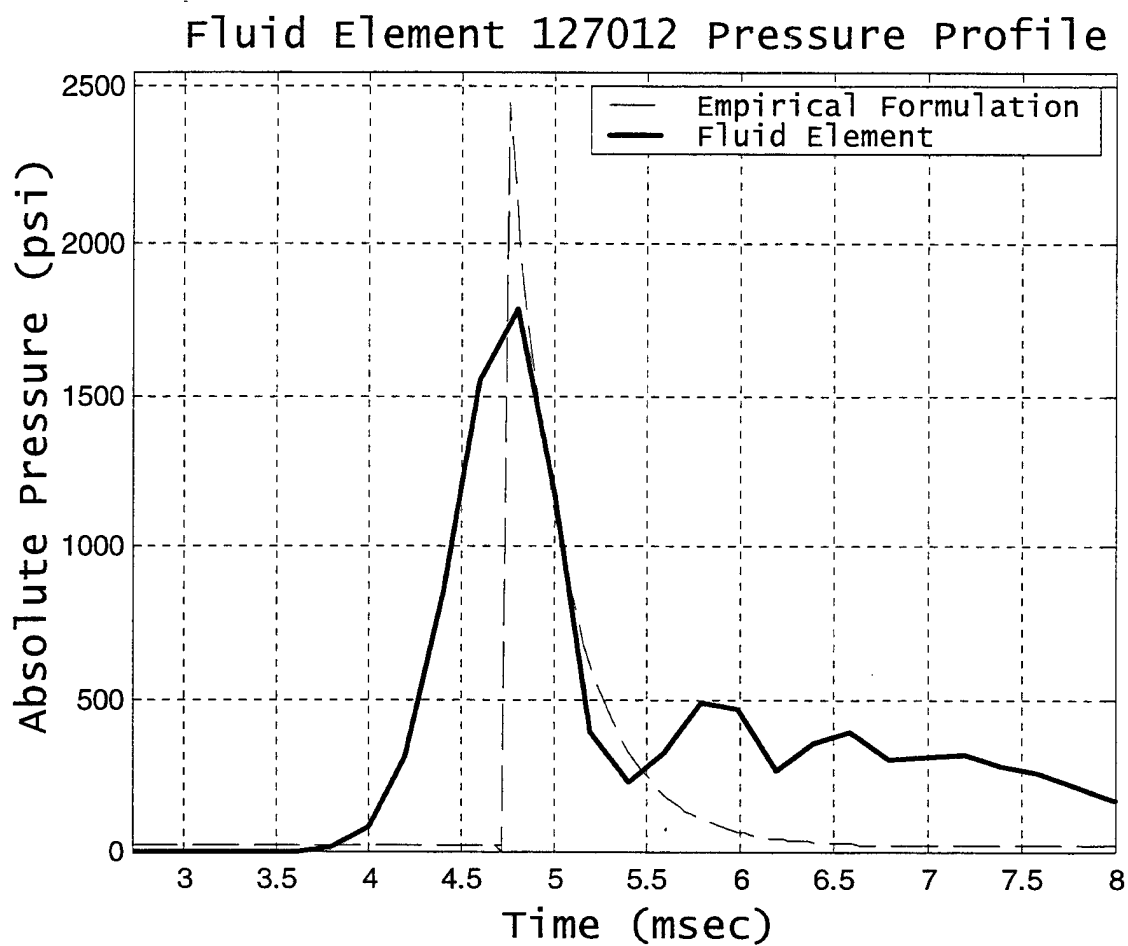


Figure 67. Fluid Element 127012 Pressure Profile
(Stair Case Along NRB 1)

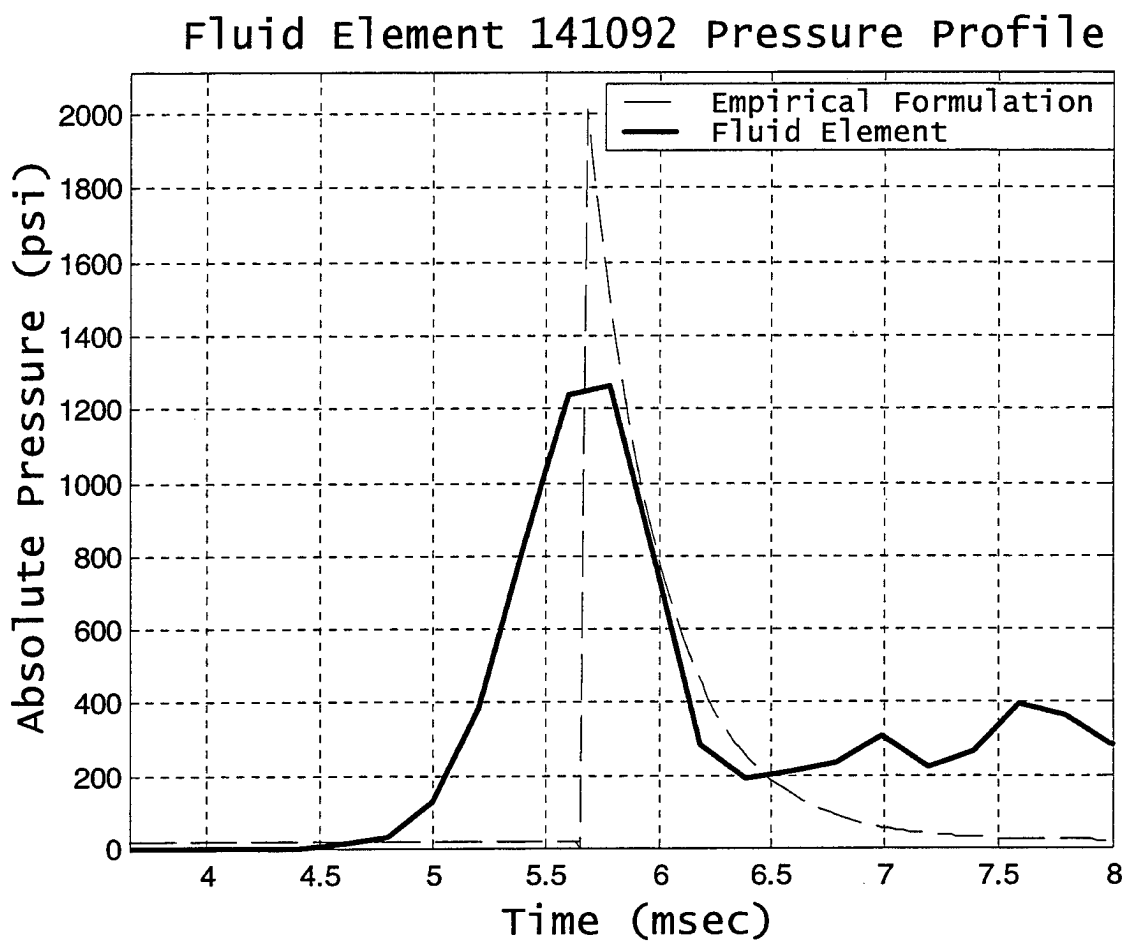


Figure 68. Fluid Element 141092 Pressure Profile
(Stair Case Along NRB 1)

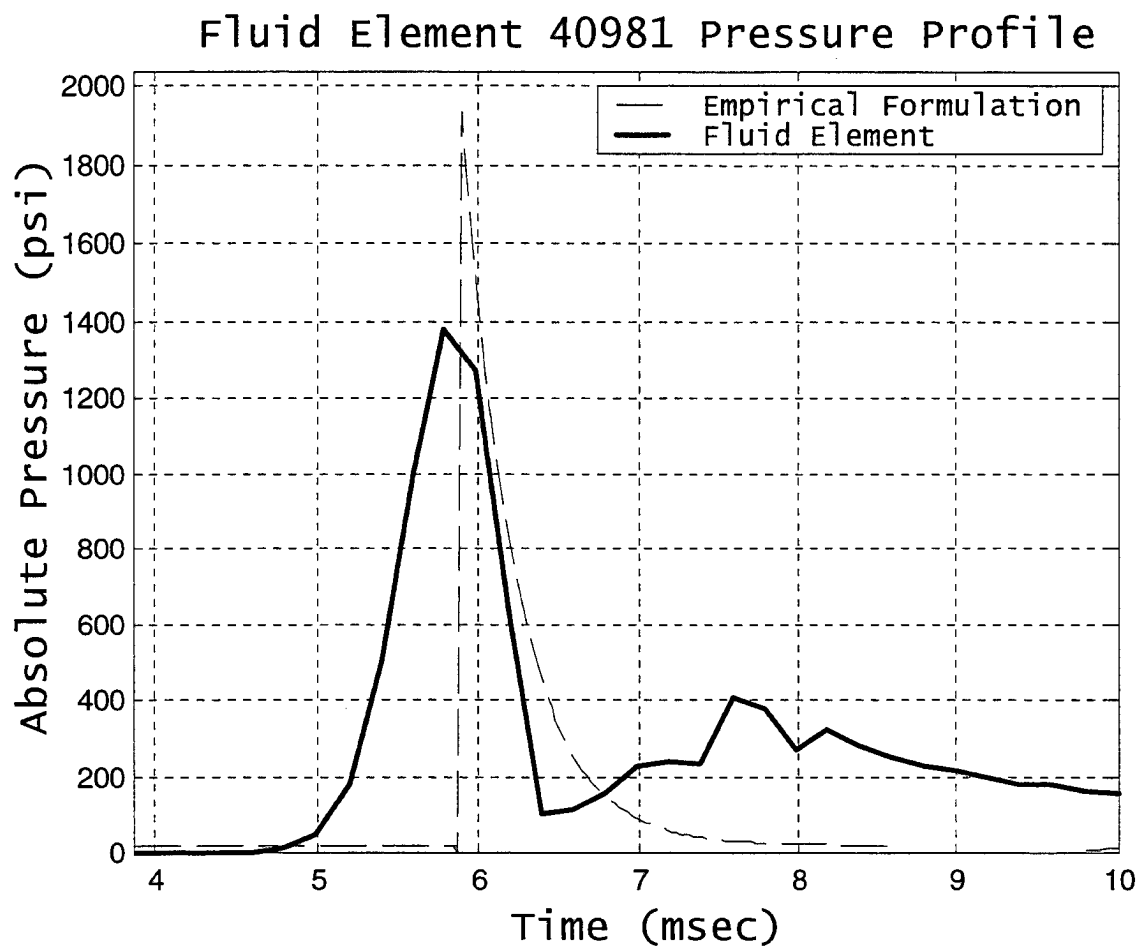


Figure 69. Fluid Element 40981 Pressure Profile
(Stair Case Along NRB 2)

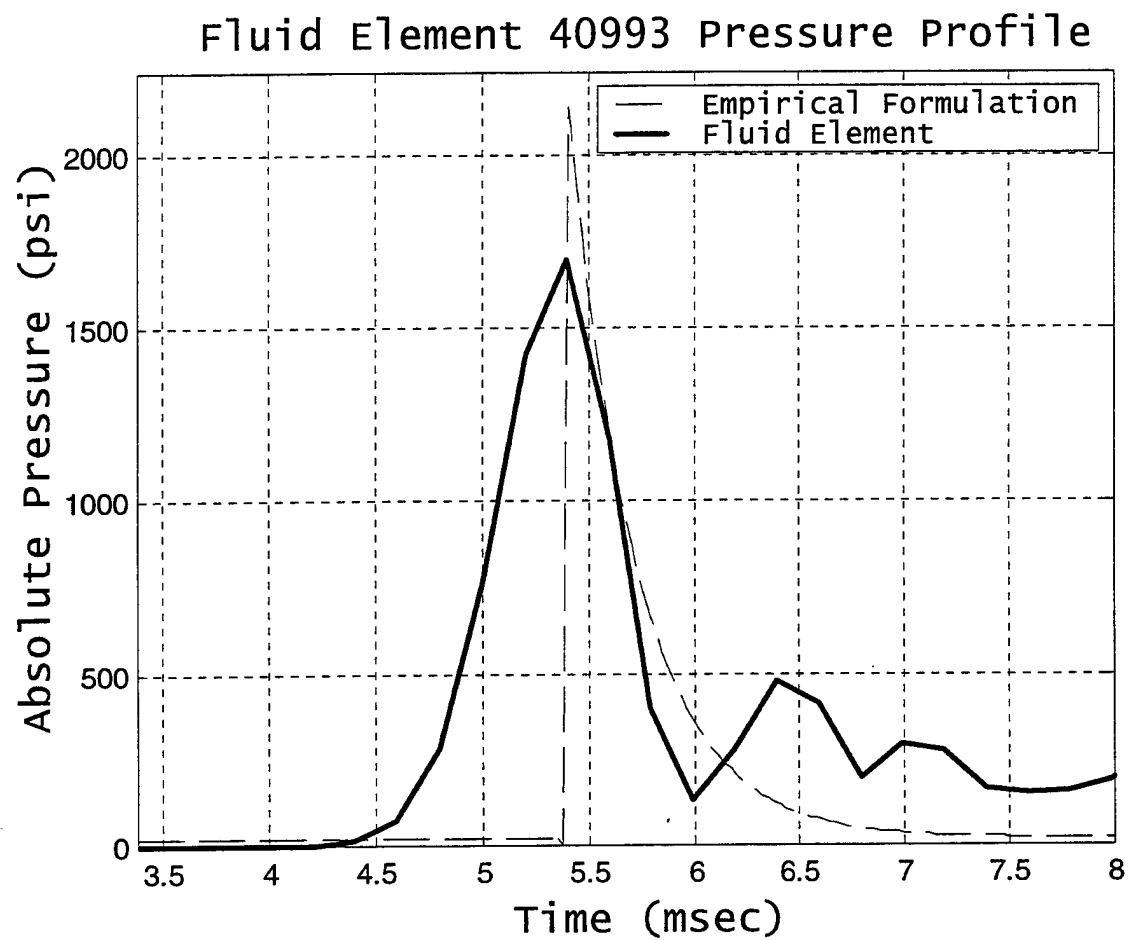


Figure 70. Fluid Element 40993 Pressure Profile
(Stair Case Along NRB 2)

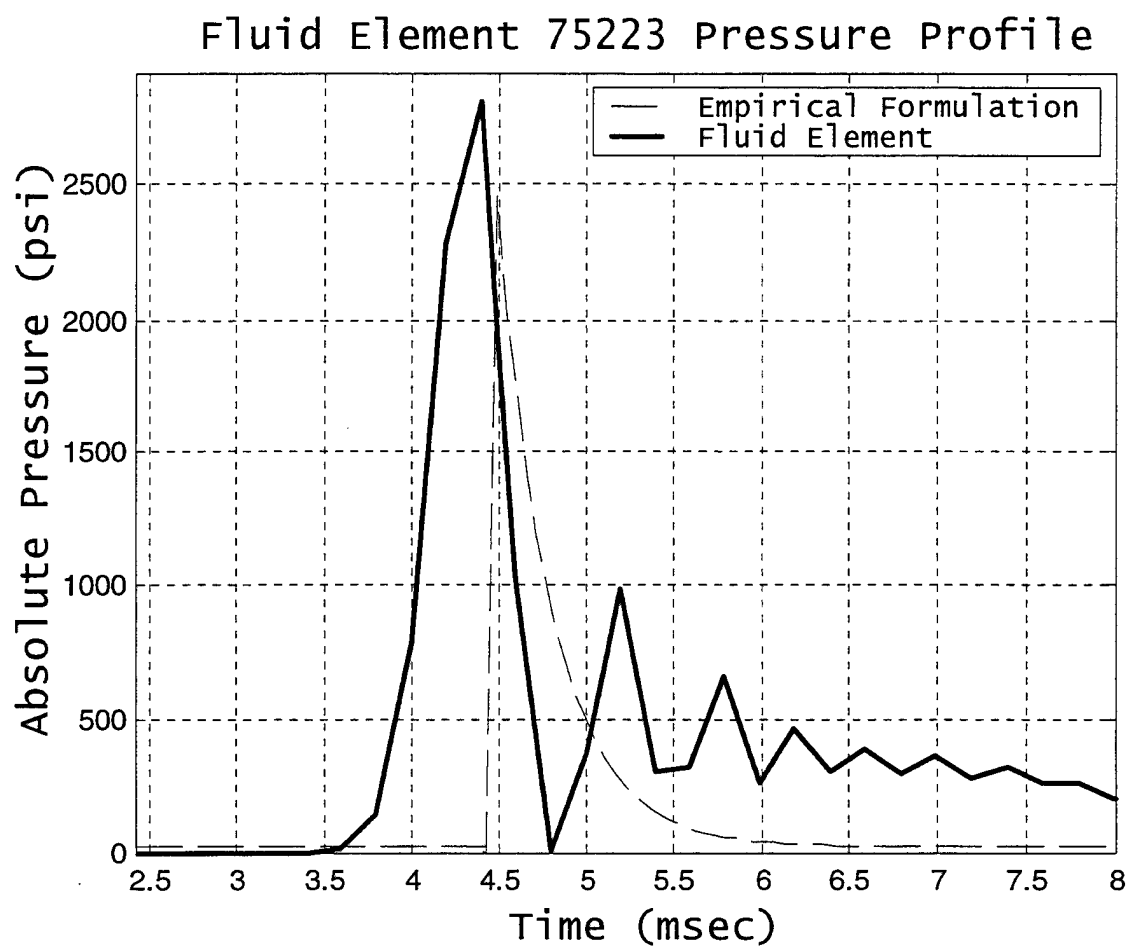


Figure 71. Fluid Element 75223 Pressure Profile
(Stair Case Along NRB 2)

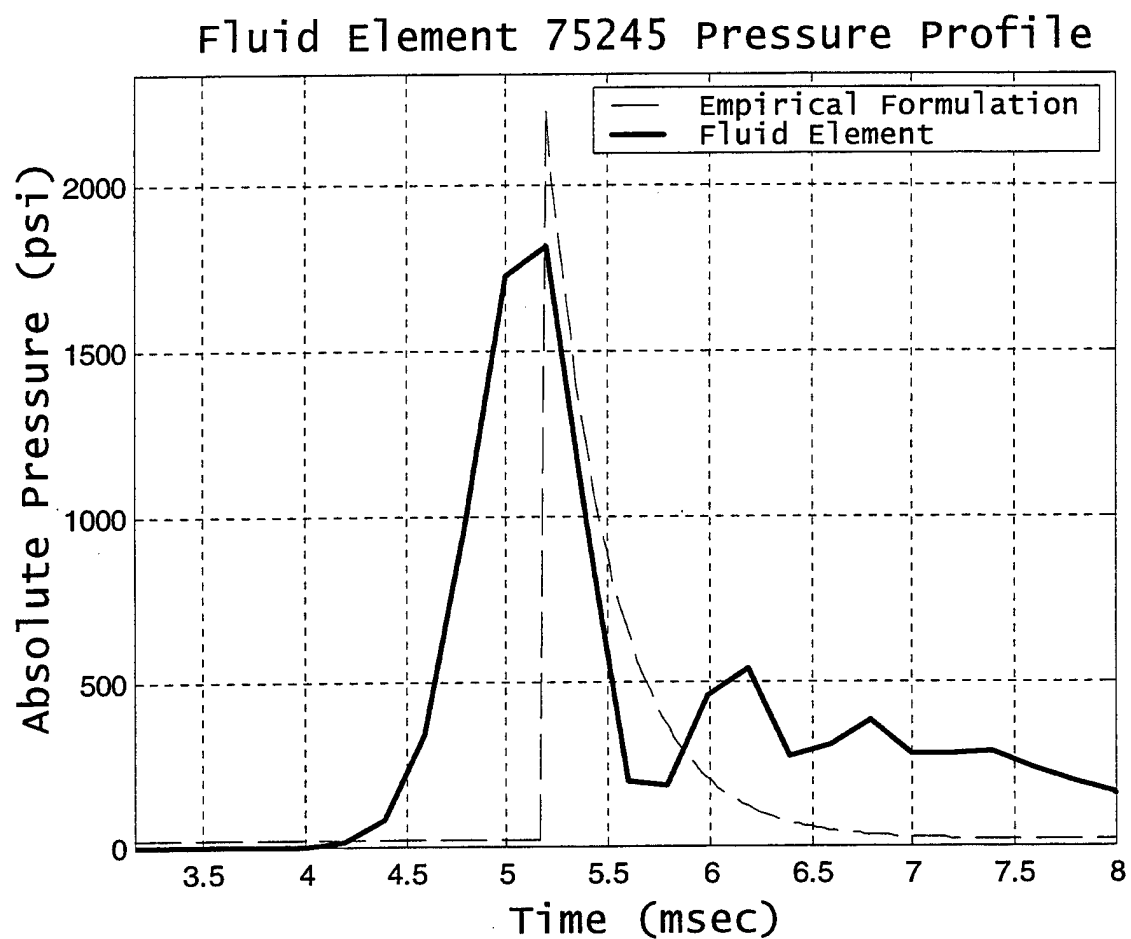


Figure 72. Fluid Element 75245 Pressure Profile
(Stair Case Along NRB 2)

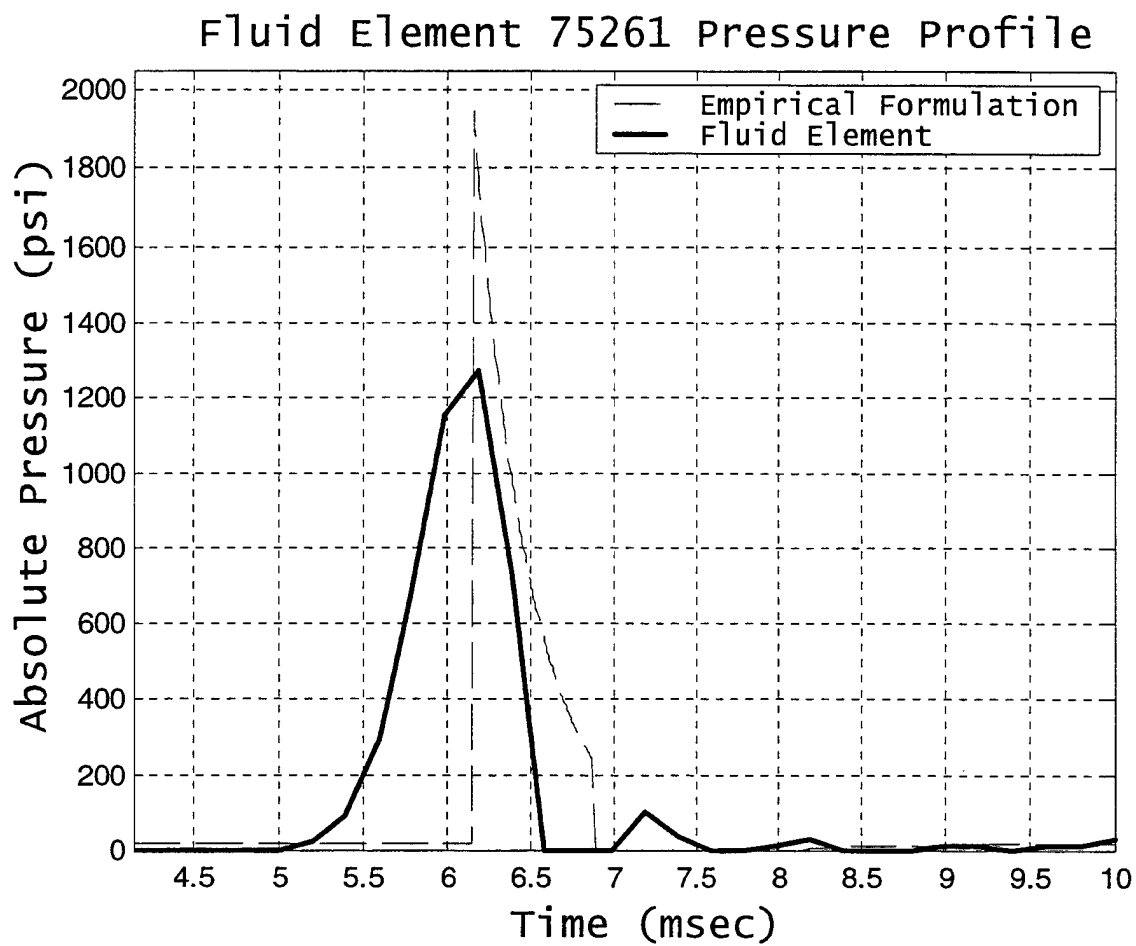


Figure 73. Fluid Element 75261 Pressure Profile
(Stair Case Along NRB 2)

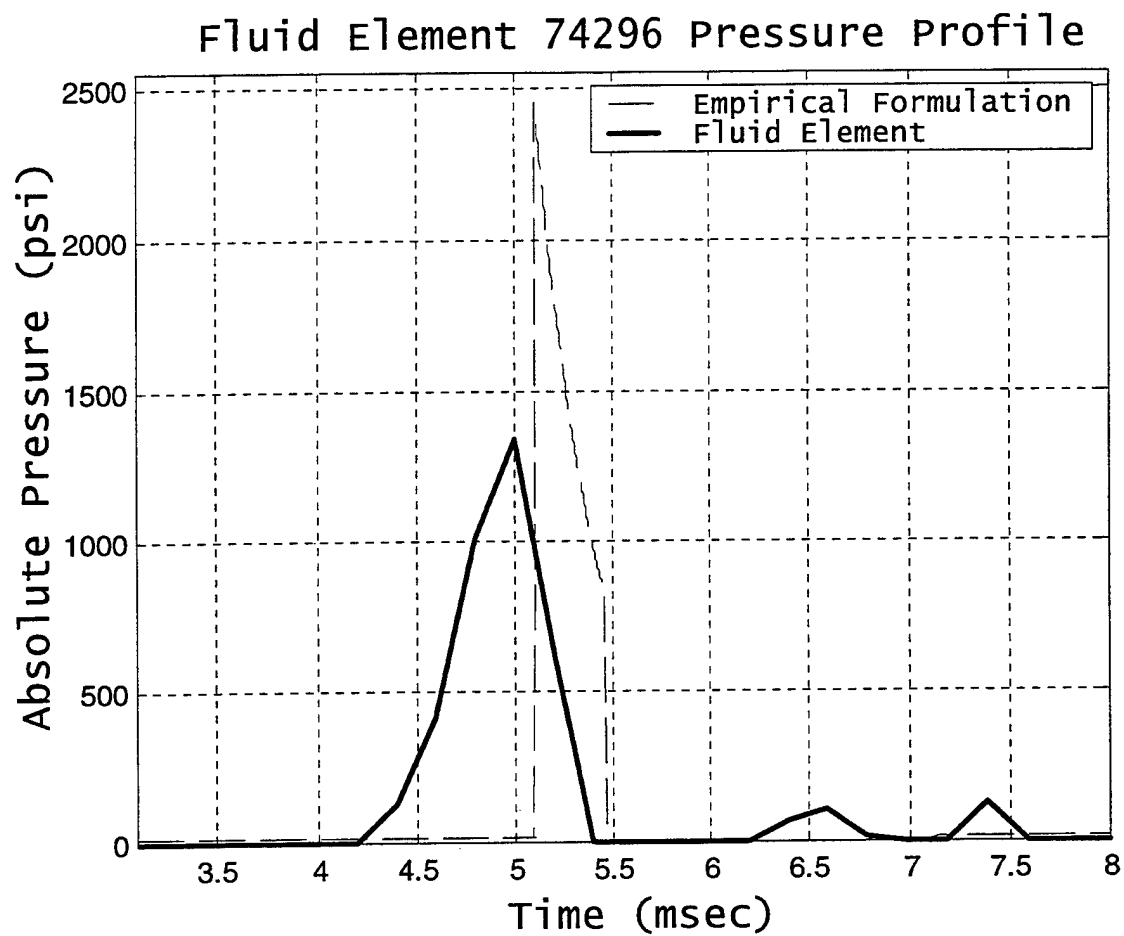


Figure 74. Fluid Element 74296 Pressure Profile
(Stair Case Underneath Barge)

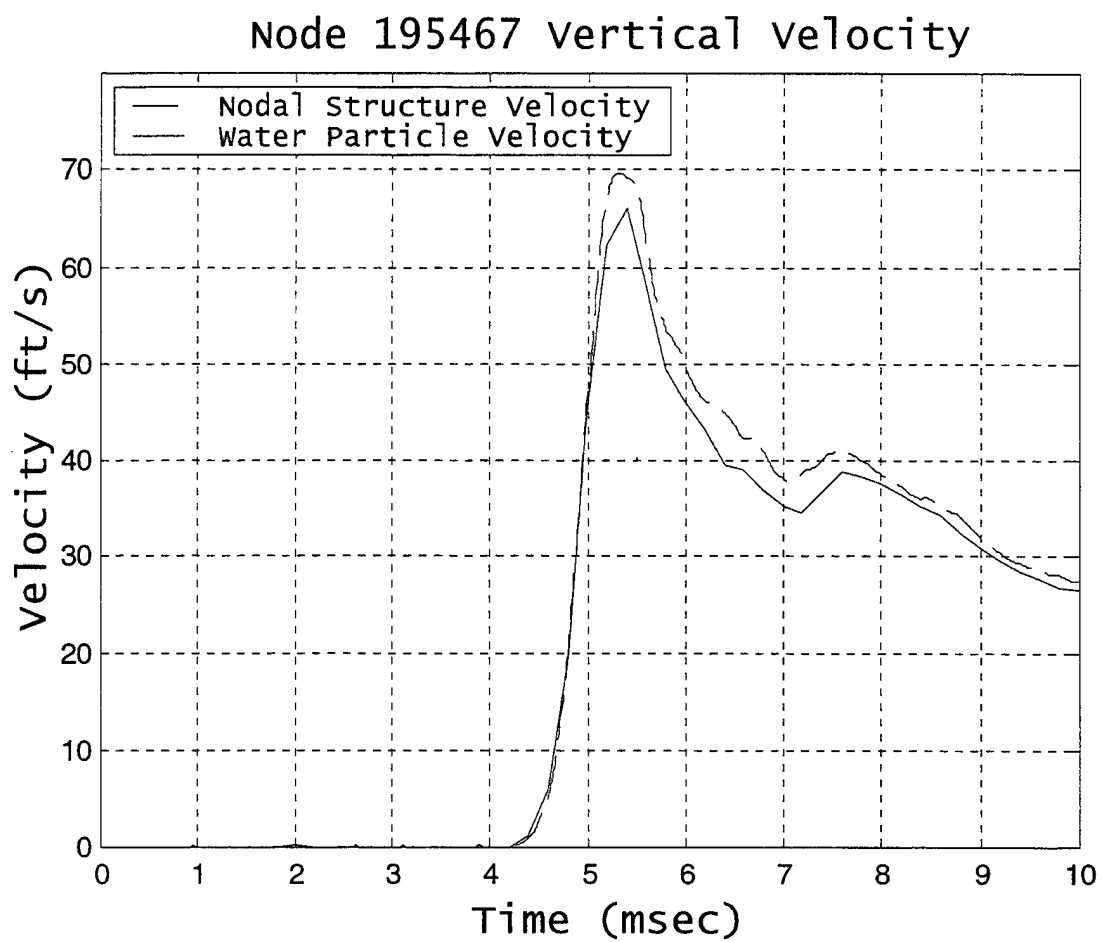


Figure 75. Velocity Response at Nodes 195467/62654

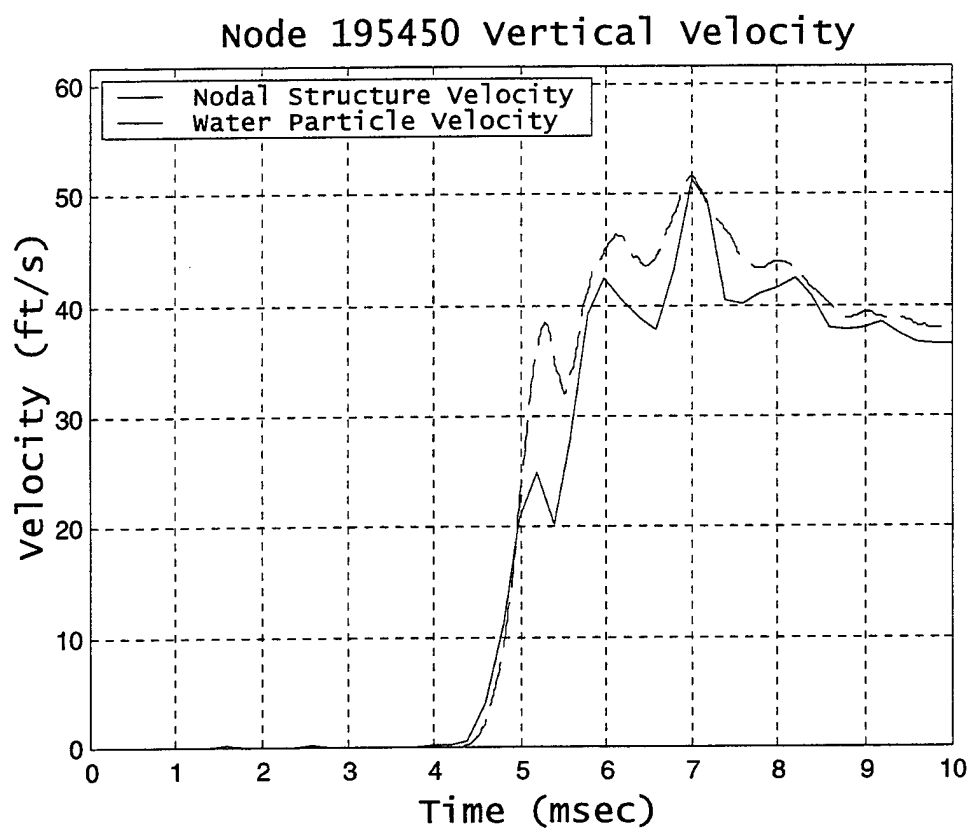


Figure 76. Velocity Response at Nodes 195450/61950

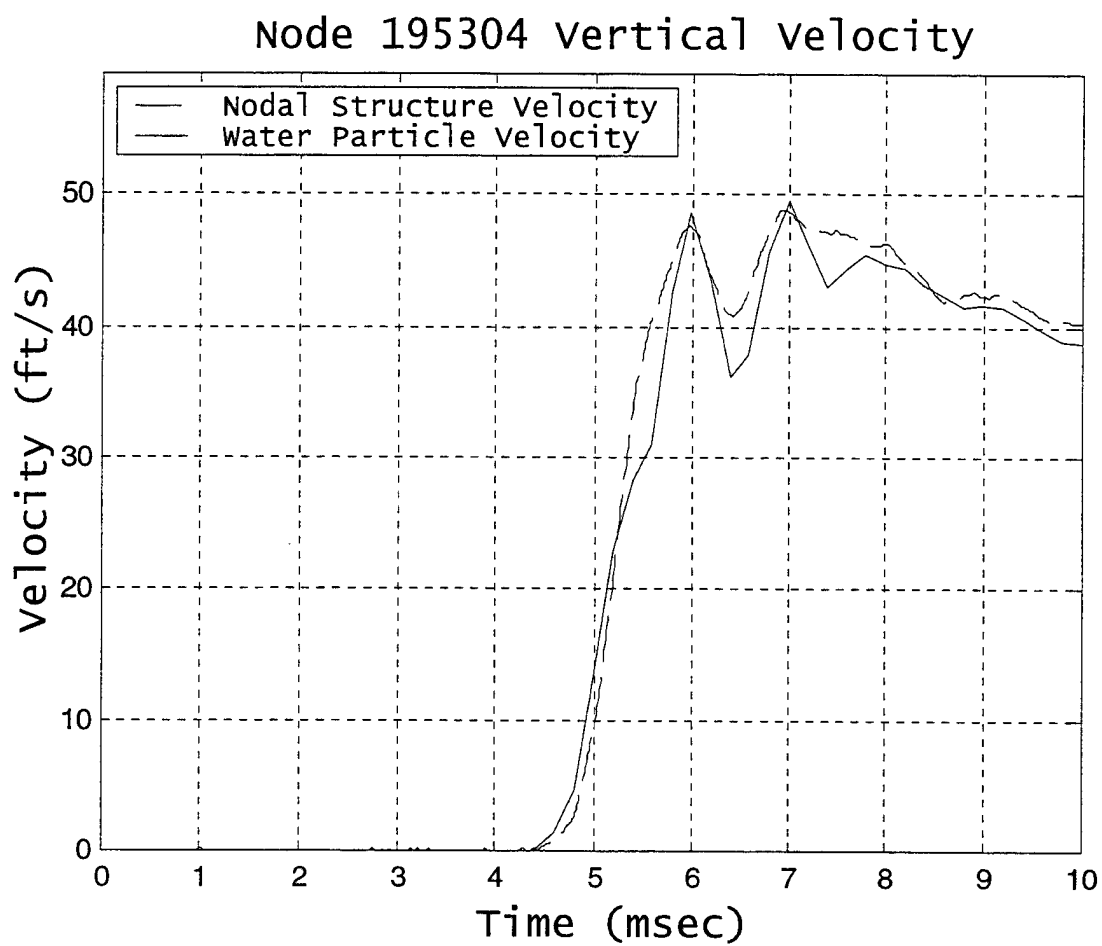


Figure 77. Velocity Response at Nodes 195304/26928

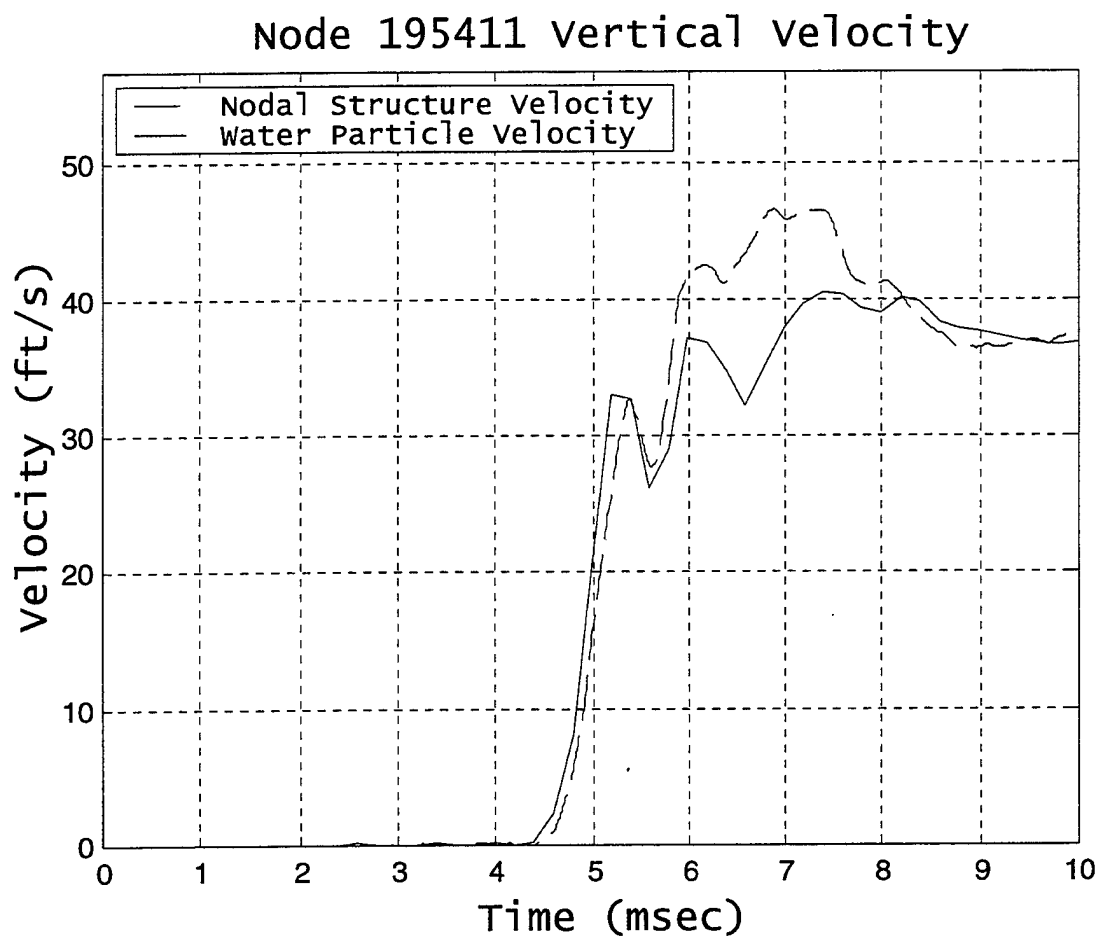


Figure 78. Velocity Response at Nodes 195411/61952

B. TWO-DIMENSIONAL AIR EXPLOSION

As a result of the numerical agreement in the underwater explosion problem, the ALE formulation will be applied to a two-dimensional air explosion problem. It is the intent of this section to demonstrate and lay a foundation on the blast pressure wave signatures in the air medium as well as effects on a structural surface. Three simulations were observed for comparison by varying the structural thickness surrounding the TNT explosive. Although a 2.54 cm (1-inch) air gap existed between the explosive and structural cylinder, other distances could have been chosen. Furthermore, thermal effects were neglected due to the EOS was not capable of handling temperature effects.

In Figures 79 through 81, the pressure rises quickly to maximum pressure, P_{\max} , at a certain time and returns to ambient pressure. The numerical pressure signatures simulated using the ALE technique show similar pressure responses found in earlier studies [Ref. 16]. Air pressure also decreases rapidly when the air element is farther away from the blast center. Notably, the structural cylinder's thickness has a definite effect on the surrounding air pressure. As the thickness of the air cylinder increases, the maximum air pressure also decreases.

The air particle velocities also exhibited a quick rise to a maximum velocity and experienced exponentially decay thereafter (Figures 82 through 84). The air particle velocities show that they reach their maximum velocities at the approximately the same time the maximum air pressure wave arrives. Furthermore, the air particle velocities also decrease at a rapid rate when the air particles are farther away from the blast center.

As the explosion initiates, the cylindrical wall experiences deformation and ultimately ruptures. Although the material's ultimate strength was not used, the structural shell elements were eroded through the material's yield strength in LS-DYNA's material card for the steel in order to provide the needed illustration effects for these models. More research is yet required is to find a suitable tangent modulus and hardening parameter as these factors play a role on material deformation and failure under an applied pressure. As noted in Figure 85, the structural velocities were notably high, especially for the thinnest shell elements.

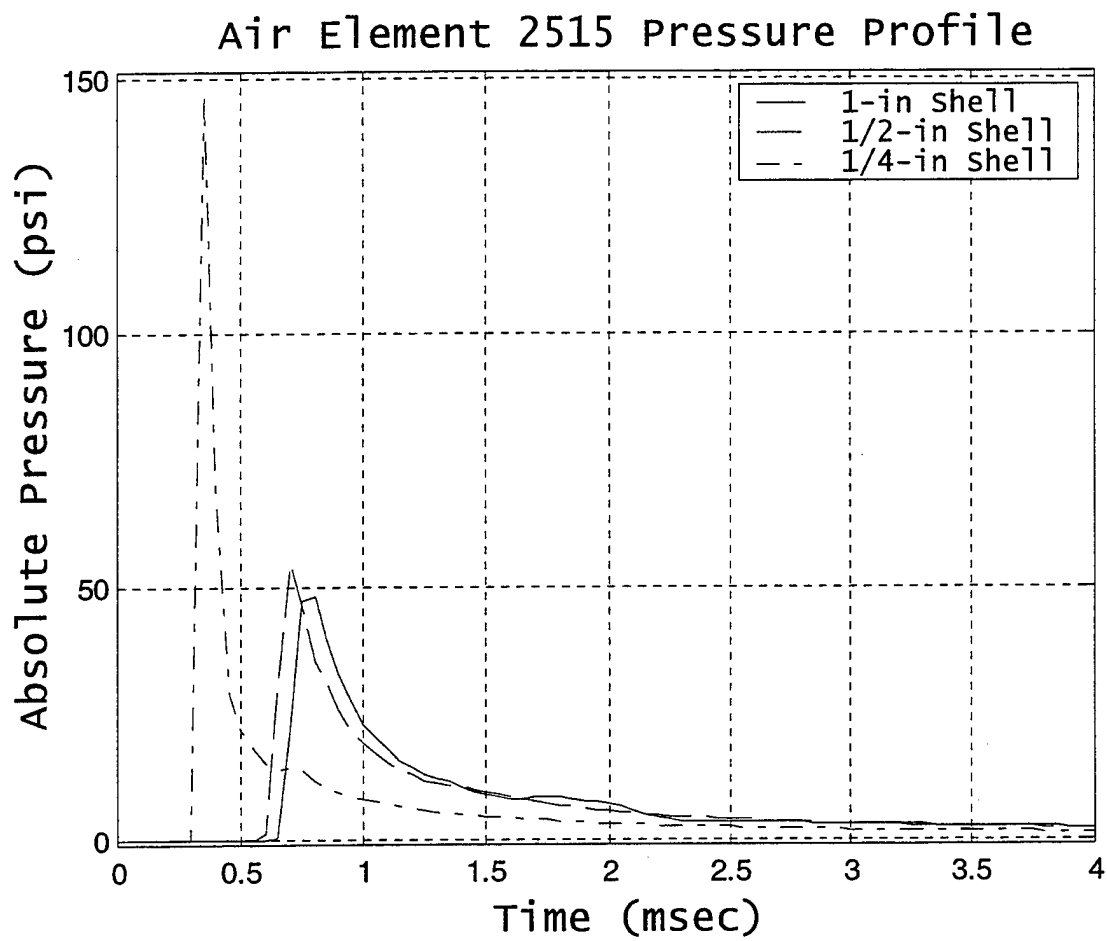


Figure 79. Air Pressure Signatures at Radius = 2.09 ft

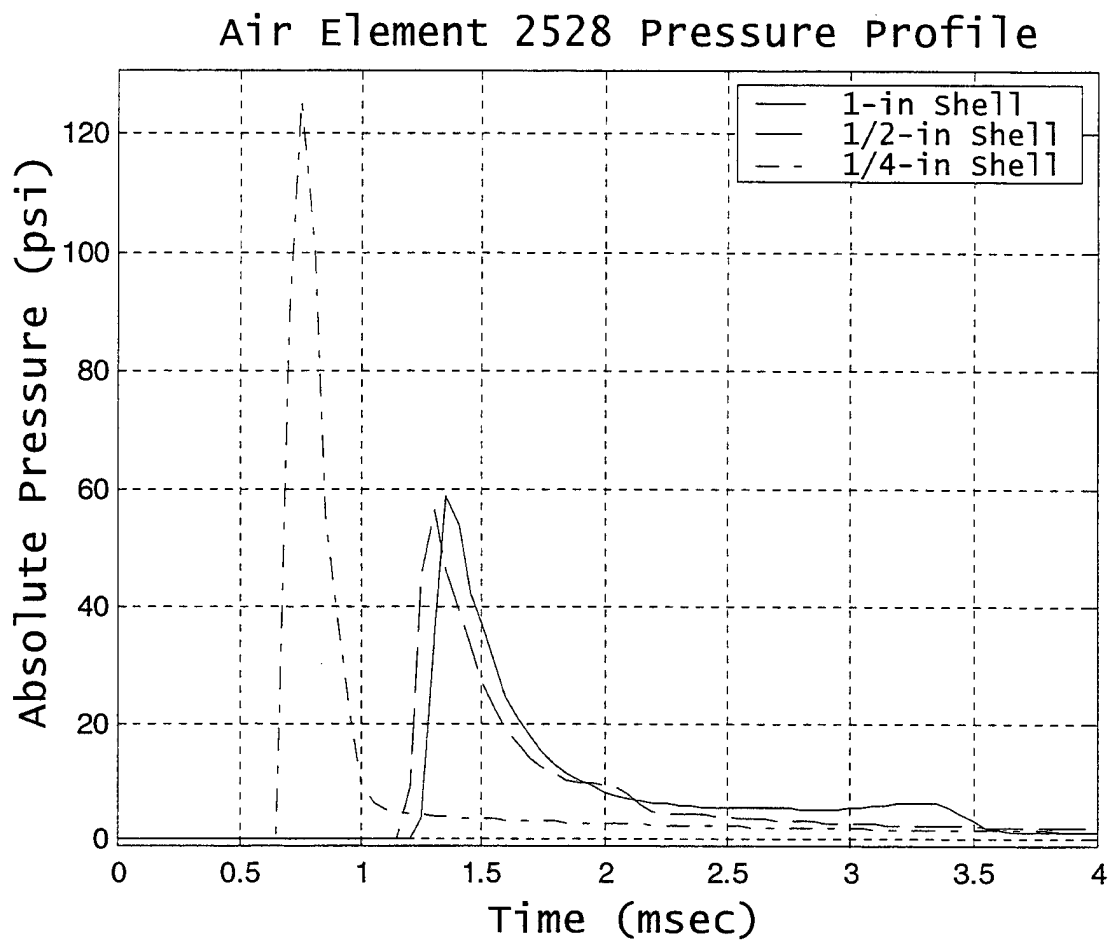


Figure 80. Air Pressure Signatures at Radius = 3.60 ft

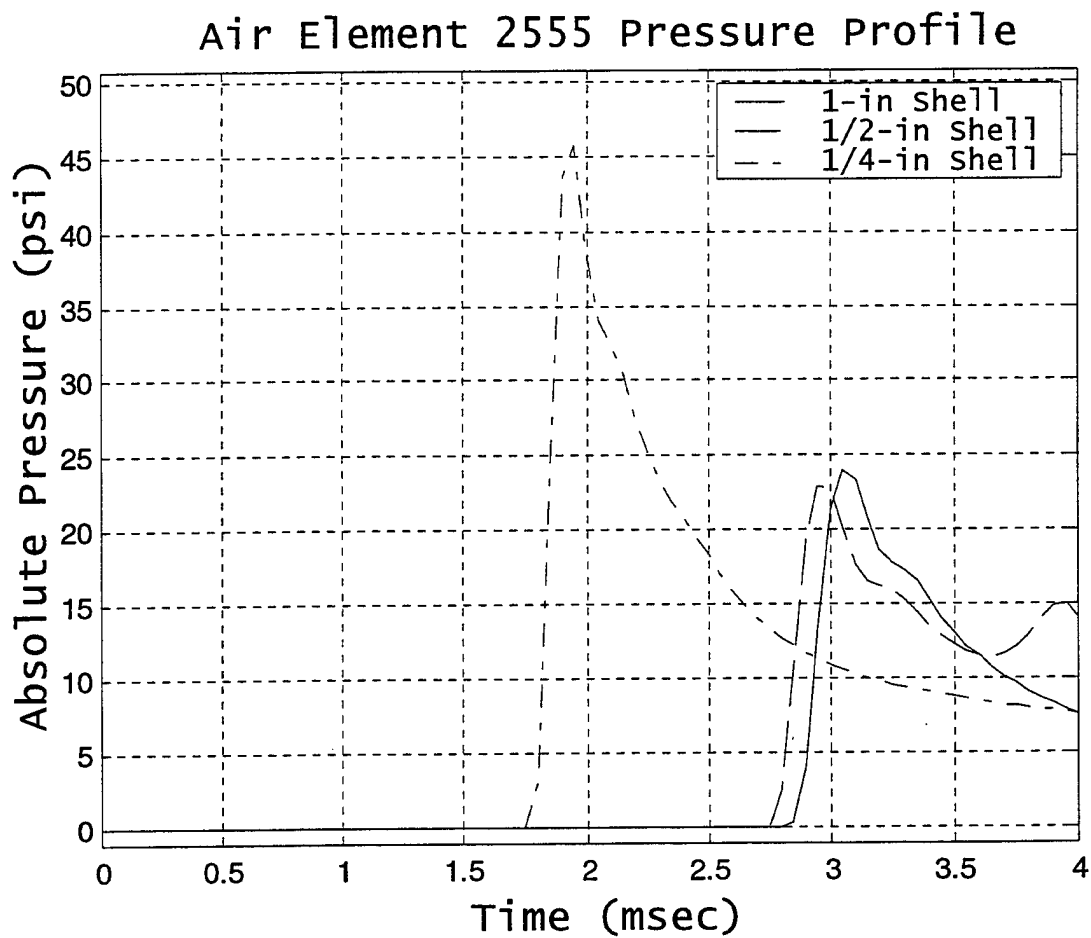


Figure 81. Air Pressure Signatures at Radius = 6.73 ft

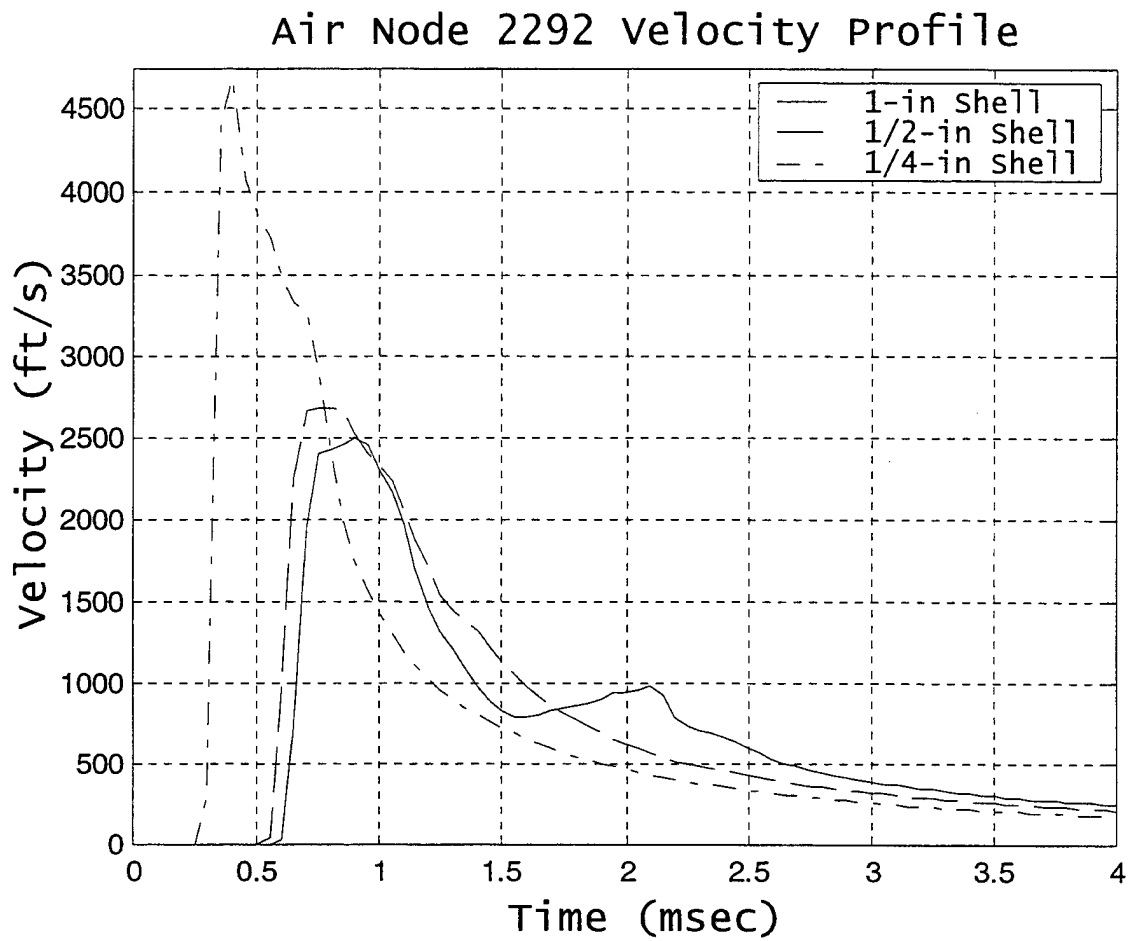


Figure 82. Air Velocity at Radius = 2.09 ft

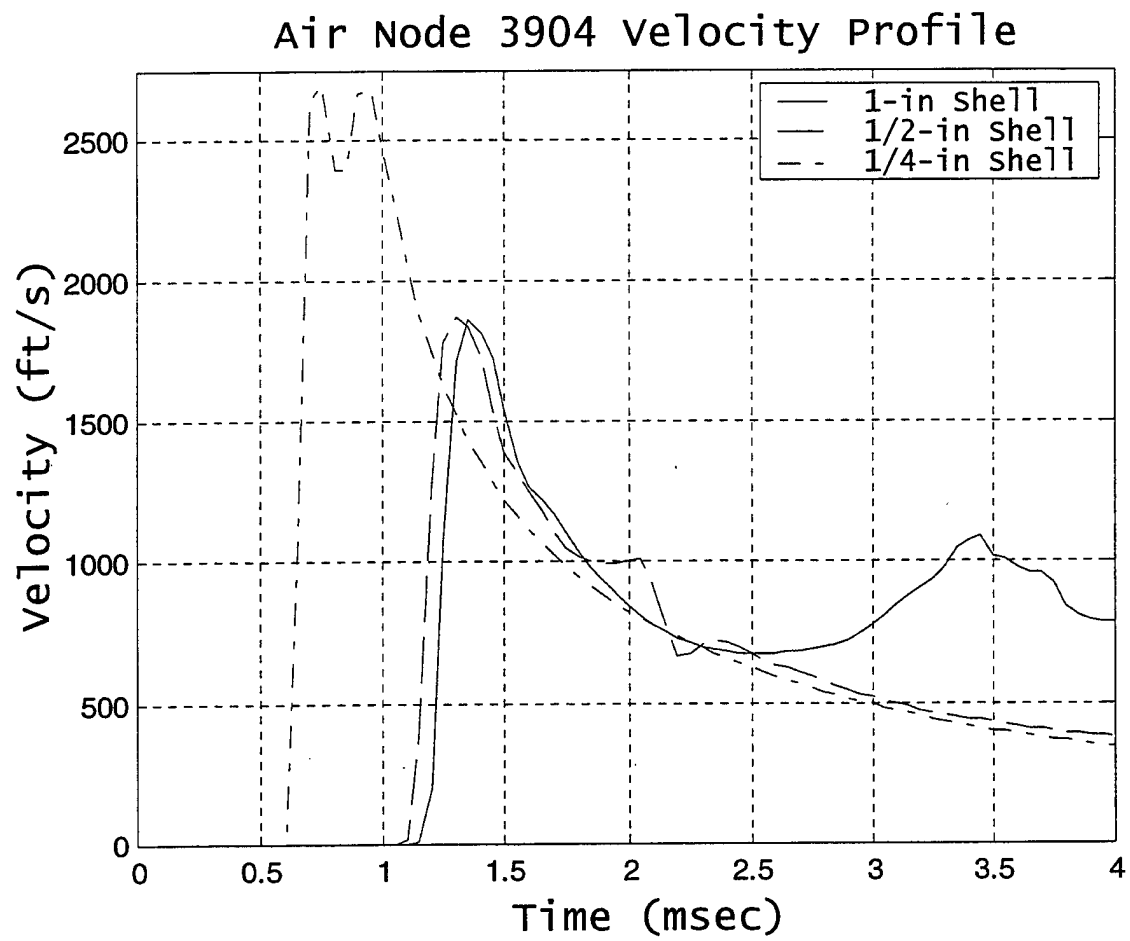


Figure 83. Air Velocity at Radius = 3.60 ft

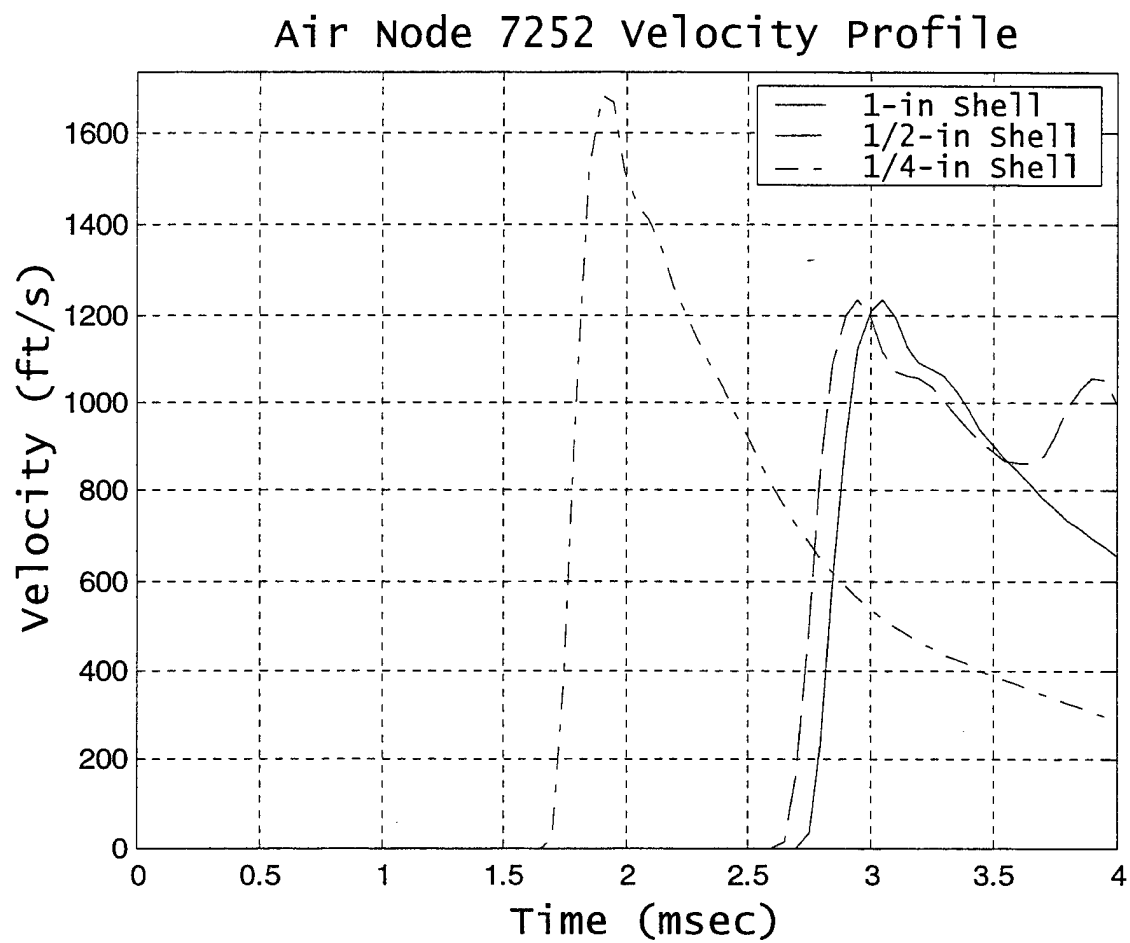


Figure 84. Air Velocity at Radius = 6.73 ft

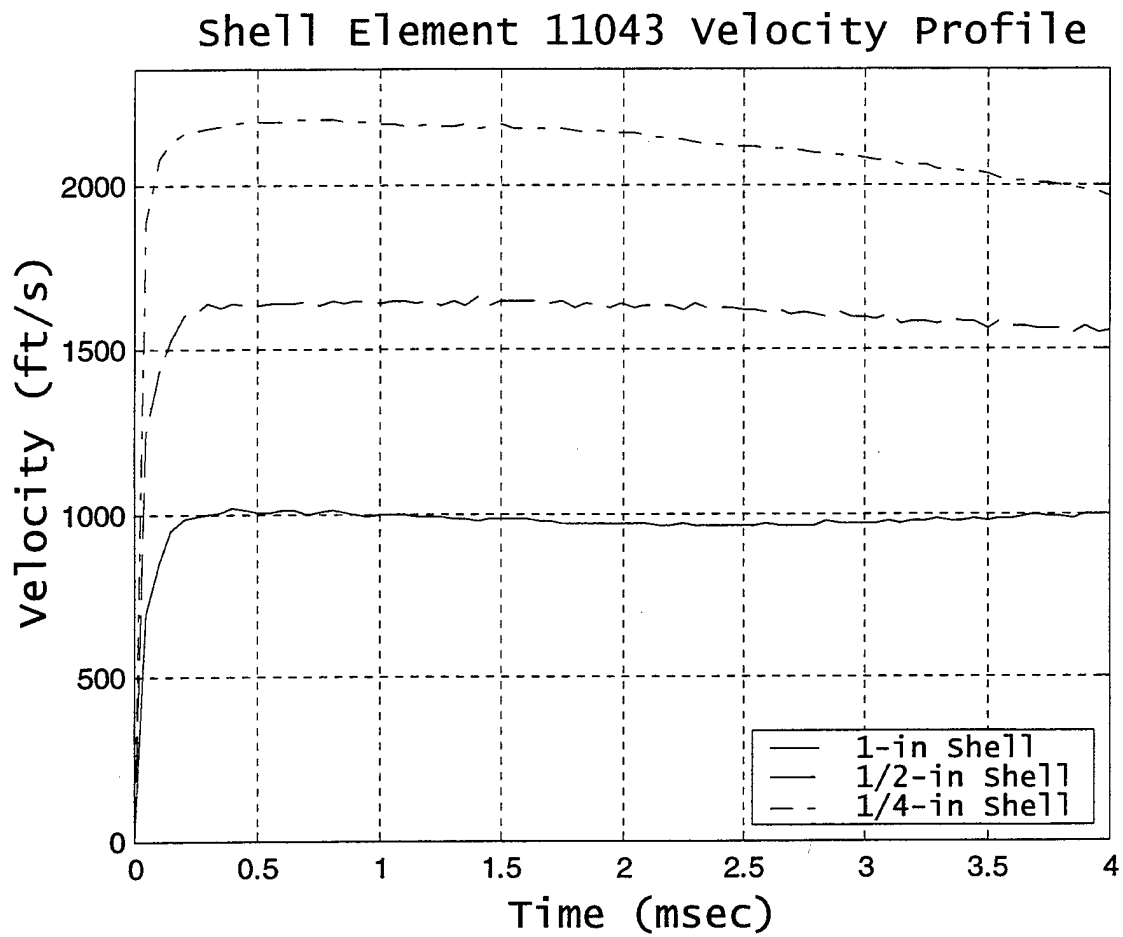


Figure 85. Structural Particle Velocities

THIS PAGE INTENTIONALLY LEFT BLANK

VII. CONCLUSIONS AND RECOMMENDATIONS

The Arbitrary Lagrangian-Eulerian (ALE) numerical technique was used to model a three-dimensional underwater explosion and two-dimensional air explosion. The simulations involved modeling the formation and propagation of the water and air shock waves as well as the fluid-structure and air-structure effects. In the underwater explosion shock wave propagation, the ALE's numerical results were verified with empirical results. With satisfactory results, a numerical confidence was established in the underwater explosion problem. As a result, a two-dimensional air explosion was modeled. The air explosion simulation achieved similar characteristic results from previous studies, although a different processing program code was used in those simulations [Ref. 16].

Through material modeling and using various equations of state, the study incorporated numerous modeling facets. It is recommended that additional studies be conducted to examine further the extent of the ALE formulations. Specifically, the following areas require additional study:

1. The effect of varying the penalty-coupling factor as it effects the fluid/air-structure interface.
2. The effect of reducing the time scale factor i.e. achieving better numerical results versus computational time.
3. Compare other different shock Hugoniots for water using the ALE numerical formulation.
4. Investigate the strain effects in the plastic kinematic/isotropic material model.
5. Investigate an equation of state, which takes into account the thermal effects for an air explosion.

THIS PAGE INTENTIONALLY LEFT BLANK

APPENDIX A. BULK CAVITATION PROGRAM

The following program code determines the bulk cavitation zone by solving Equations (3.18) and (3.19). The code is written for MATLAB Version 5.2 [Ref. 23].

```
% ME 4525 DESIGN PROJECT 1
% by LT Ted Trevino
% This program computes the axisymmetric upper and lower cavitation
% boundaries for an
% input charge (TNT or HBX-1). The program iterates up to a cavitation
% zone radius
% of 1400 ft and vertical distance of -50 ft. The program also
% calculates the maximum
% horizontal radius at its certain depth, and area enclosed by the upper
% and lower
% boundaries. Cavitation boundaries are based on Aron's Method.

clear
clf

gamma = .03703; % seawater weight density @ 1 atm (lbm/in^3)
pa = 14.7; % atmospheric pressure (psi)
c = 5000; % acoustic velocity (ft/s)

disp(' ')
disp('Select charge type number: ');
disp(' (1) HBX-1')
disp(' (2) TNT')
charge_type = input('Enter selection number: ');
W = input('Enter charge weight (lbf): ');
D = input('Enter charge depth (ft): ');

% HBX-1 Calculations
if (charge_type == 1)
    chg_name = 'HBX-1 Charge';
    weight = num2str(W);
    depth = num2str(D);
    K1 = 22347.6; % Constant
    K2 = 0.056; % Constant
    A1 = 1.144; % Constant
    A2 = -0.247; % Constant
    ub_data = []; % Upper boundary data for x and y values
    lb_data = []; % Lower boundary data for x and y values

    % Calculate upper boundary
    for x = 0:1400
        for y = 0:0.1:50;
            r1 = sqrt((D-y)^2 + x^2); % Standoff distance charge-point
            r2 = sqrt((D+y)^2 + x^2); % Standoff distance image-point
            theta = K2*W^(1/3)*(W^(1/3)/r1)^A2/1000; % decay constant (sec)
            Fterm1 = (K1*(W^(1/3)/r1)^A1*exp(-(r2-r1)/(c*theta)));
            Fterm2 = (gamma*y*12) - (K1*(W^(1/3)/r2)^A1);
```

```

        F = Fterm1 + Fterm2 + pa; % Upper cavitation boundary
        if F <= 0
            ub_data = [ub_data; F x -(y)];
            break
        end
    end
end

% Calculate lower boundary
for x = 0:(length(ub_data)-1)
    for y = 0:0.1:50
        r1 = sqrt((D-y)^2 + x^2); % Standoff distance charge-point
        r2 = sqrt((D+y)^2 + x^2); % Standoff distance image-point
        theta = K2*W^(1/3)*(W^(1/3)/r1)^A2/1000; % Decay constant
        % Incident SW pressure
        pi = K1*(W^(1/3)/r1)^A1*exp(-(r2-r1)/(c*theta));
        Gterm1 = -(pi/(c*theta))*(1+(((r2-
            (2*D*(D+y)/r2))/r1)*((A2*r2)/r1)-A2-1)));
        Gterm2 = -((A1*pi)/r1^2)*(r2-2*D*((D+y)/r2));
        Gterm3 = (gamma*12)*((D+y)/r2);
        Gterm4 = (A1/r2)*(pi+pa+(gamma*y*12));
        % Lower cavitation boundary
        G = Gterm1 + Gterm2 + Gterm3 + Gterm4;
        if G >= 0
            lb_data = [lb_data; G x -(y)];
            break
        end
    end
end

% TNT Calculations
elseif (charge_type == 2)
    chg_name = 'TNT Charge';
    weight = num2str(W);
    depth = num2str(D);
    K1 = 22505; % Constant
    K2 = 0.058; % Constant
    A1 = 1.18; % Constant
    A2 = -0.185; % Constant
    ub_data = []; % Upper boundary data for x,y values
    lb_data = []; % Lower boundary data for x,y values

    % Calculate upper boundary
    for x = 0:1400
        for y = 0:0.1:50;
            r1 = sqrt((D-y)^2 + x^2); % Standoff distance charge-point
            r2 = sqrt((D+y)^2 + x^2); % Standoff distance image-point
            theta = K2*W^(1/3)*(W^(1/3)/r1)^A2/1000; % decay constant (sec)
            Fterm1 = (K1*(W^(1/3)/r1)^A1*exp(-(r2-r1)/(c*theta)));
            Fterm2 = (gamma*y*12) - (K1*(W^(1/3)/r2)^A1);
            F = Fterm1 + Fterm2 + pa; % Upper cavitation boundary
            if F <= 0
                ub_data = [ub_data; F x -(y)];
                break
            end
        end
    end
end

```

```

        end
    end

    % Calculate lower boundary
    for x = 0:(length(ub_data)-1)
        for y = 0:0.1:50
            r1 = sqrt((D-y)^2 + x^2); % Standoff distance charge-point
            r2 = sqrt((D+y)^2 + x^2); % Standoff distance image-point
            theta = K2*W^(1/3)*(W^(1/3)/r1)^A2/1000; % Decay constant
            % Incident SW pressure
            pi = K1*(W^(1/3)/r1)^A1*exp(-(r2-r1)/(c*theta));
            Gterm1 = -(pi/(c*theta))*(1+(((r2-
                (2*D*(D+y)/r2))/r1)*((A2*r2)/r1)-A2-1)));
            Gterm2 = -((A1*pi)/r1^2)*(r2-2*D*((D+y)/r2));
            Gterm3 = (gamma*12)*((D+y)/r2);
            Gterm4 = (A1/r2)*(pi+pa+(gamma*y*12));
            % Lower cavitation boundary
            G = Gterm1 + Gterm2 + Gterm3 + Gterm4;
            if G >= 0
                lb_data = [lb_data; G x -(y)];
                break
            end
        end
    end
else
    disp('You did not enter selection 1 or 2. Please rerun program with
    appropriate entry. ');
    break
end

% Define boundary cavitation envelope
ub = find(ub_data(:,3)<lb_data(:,3));
lb = find(lb_data(:,3)>ub_data(:,3));
ub_data(ub,:) = [];
lb_data(lb,:) = [];

height = ub_data(:,3) - lb_data(:,3); % Heights bw up & low boundaries
area = sum(height); % Area enclosed by upper/lower boundaries
vert1 = [-D]; % Charge location vertically
hor1 = [0]; % Charge location horizontally

%disp(' ')
%disp('*****')
%fprintf('The maximum horizontal radius is %1.2f ft at a depth of %1.2f
ft.\n',hor,vert)
%disp(' ')
%fprintf('The 2-D axisymmetric bulk cavitation envelope area = %1.2f
ft^2\n',area)

orient landscape
% Plot upper and lower boundary data and max horizontal radius
plot(ub_data(:,2),ub_data(:,3),'b',lb_data(:,2),lb_data(:,3),'g',hor1,ver
t1,'m*');
grid

```

```
title(['Bulk Cavitation Envelope for ',weight,' lb ',chg_name,' at  
,depth,' ft']);  
xlabel('Horizontal Range (ft)')  
ylabel('Vertical Depth (ft)')  
legend('Cavitation Upper Boundary','Cavitation Lower Boundary',4)  
axis([0 800 -55 5])  
text(25,-2-D,'Charge')
```

APPENDIX B. USEFUL TRUEGRID COMMANDS

TrueGrid [Refs. 7 and 18] is a powerful finite element-modeling tool whose purpose is to create multiple block-structured mesh. The program has many useful features to aid in visualizing and manipulating a finite element model. Different input and output formats are also supported, such as LS-DYNA keyword format. Basic familiarity with TrueGrid is assumed. TrueGrid consists of three phases: control, part and merge phases. In the control phase, material models are defined and initialized. In the part phase, the mesh is constructed through projecting, deleting, and refining the mesh. Boundary conditions are also initialized in this phase. In the merge phase, the different parts are assembled together by merging nodes. Output formats (deck) are constructed during this phase. This appendix will cover some of the important commands used for mesh generation.

A **block** or **cylinder** command can be entered in the control or merge phases. The **block** command syntax consists of *i_indices*; *j_indices*; *k_indices*; *x_coordinates*; *y_coordinate*; *z_coordinates*. Once the **block** command has been entered, the i, j, k indices are found in the computational window while the corresponding x, y, z coordinates exist in the physical window. The **cylinder** command syntax consists of *i_indices*; *j_indices*; *k_indices*; *r_coordinates*; *theta_coordinates*; *z_coordinates*.

Once in the parts phase i.e. a block or cylinder command has been issued, a material number should be established through the **mate** command. Boundary conditions were established using the nodal displacement and rotation constraints, **b**, and non-reflecting boundaries, **nr**, commands. Elements from a part can be deleted using a combination of the computational window and environmental window. Elements needing to be deleted can be highlighted in the computational window using the mouse, then the delete button can be selected in the environmental window. This should generate a new mesh in the physical and computational windows with the elements deleted. For explosives, the detonation point, **detp**, command specifies where the detonation point will be placed in the actual physical window. Lastly, to prevent the structural nodes from merging with the fluid nodes a sliding interface region, **si**, was placed. The fluid nodes were assigned as the master nodes, and the structural nodes were assigned as the slave nodes.

Since the models deal with multi-materials or multi-parts, the nodes must be merged to form some type connectivity. Once all of the parts for the model were entered, the nodes were merged using the **stp** command. The nodes that fall within a specified tolerance defined by the user will merge with the exception of the sliding interface regions. Point masses are added using the **pm** command. After the entire mesh has been generated, LS-DYNA output format was selected using the **OUTPUT** command and then the **WRITE** command with no arguments is selected. This will produce an LS-DYNA format output file name called "trugrdo."

APPENDIX C. TRUEGRID COMMANDS: UNDEX 3-D MODEL WITH BLOCK TNT EXPLOSIVE MODEL

This Appendix provides the input program used for the underwater three-dimensional model using a block TNT explosive model approach. The structural material properties and thickness values were input in LS-DYNA. TrueGrid does offer the feature to input material properties using the LSDYMAT5 command. Appendix B and references 7 and 28 offer the meaning to the command lines.

```
c ted trevino
c tnt block explosive model

c establish explosive mesh using block command
block 1 2 3 4;1 2;1 2;-27.405 -9.135 9.135 27.405;0 17.45;0 17.45;
c set up axis-symmetric boundaries
b 1 1 1 4 1 2 dy 1 ry 1 ;
b 1 1 1 4 2 1 dz 1 rz 1;
c explosive material number that will be used to describe nodes in
c LS-DYNA.
c Material card can be defined in TrueGrid but is defined in LS-DYNA
mate 11
c Establish detonation point for the explosive
detp 11 point -9.135 0 0;
merge

c water mesh
block 1 18 29 30 31 32 43 60;1 2 41 43;1 2 18 22 39;-518.16 -213.36 -
27.405
-9.135 9.135 27.405 213.36 518.16;0 17.45 701.04 731.52;0 17.45 304.8
365.76
670.56;
c delete unwanted water mesh to make room for barge and explosive
dei 3 6; 1 2; 1 2;
dei 2 7; 3 4; 3 4;
c water material nr that will be used in LS-DYNA
mate 10
c Establish axis-symmetric boundaries
b 1 1 1 8 4 1 dz 1 rz 1;
b 1 1 1 8 1 5 dy 1 ry 1;
c Establish non-reflecting boundaries
nr 1 1 1 1 4 5
nr 1 1 5 8 4 5
nr 8 1 1 8 4 5
c setup interface along the water nodes next to the barge so those nodes
c will not merge with the barge. !Important! Defined water as the master
c nodes
sid 1 ldsi p1 ; ;
si 2 3 3 2 4 4 1 m ;
```

```

si 2 3 3 7 3 4 1 m ;
si 7 3 3 7 4 4 1 m ;
si 2 3 3 7 4 3 1 m ;
si 2 3 4 7 4 4 1 m ;
merge

c air mesh
block 1 18 29 30 31 32 43 60;1 3 13;1 2 18 22 39;-518.16 -213.36 -27.405
-9.135
9.135 27.405 213.36 518.16;701.04 731.52 914.4;0 17.45 304.8 365.76
670.56;
c delete unwanted air nodes
dei 1 8; 1 2; 1 3;
dei 1 8; 1 2; 4 5;
dei 7 8; 1 2; 3 4;
dei 1 2; 1 2; 3 4;
c establish axis-symmetric boundary
b 1 1 1 8 3 1 dz 1 rz 1;
c establish non-reflective boundaries
nr 1 1 1 1 3 5
nr 8 1 1 8 3 5
nr 1 1 5 8 3 5
c air material number
mate 12
merge

c barge mesh
block -1 -6 -12 -17;-1 7;-1 4 -7;-213.36 -86.36 86.36 213.36;701.04
762;304.8
335.28 365.76;
c barge material number
mate 1
c establish interface along the barge shells so nodes will not merge with
c with adjacent water. Defined as slave nodes.
si 1 1 1 1 2 3 1 s ;
si 1 1 1 4 1 3 1 s ;
si 4 1 1 4 2 3 1 s ;
si 1 1 1 4 2 1 1 s ;
si 1 1 3 4 2 3 1 s ;
merge
c merge node tolerance
stp 0.1

c add point masses along three nodes
pm 124126 1.16338e+5;
pm 124261 1.16338e+5;
pm 124392 1.16338e+5;

```

APPENDIX D. TRUEGRID COMMANDS: UNDEX 3-D MODEL WITH STAIR TNT EXPLOSIVE MODEL

This Appendix provides the input program used for the underwater three-dimensional model using a stair-cased TNT explosive model approach. The structural material properties and thickness values were input in LS-DYNA. TrueGrid does offer the feature to input material properties using the LSDYMAT5 command. Appendix B and references 7 and 27 offer the meaning to the command lines.

```
c ted trevino
c tnt stair-cased charge model

c charge model
block 1 2 3 4 5 6;1 2 3 4;1 2 3 4;-26.5 -15.91 -5.3 5.3 15.91 26.5;0
10.60
21.2 31.80;0 10.60 21.2 31.80;
c delete numerous blocks to model explosive stair case model
dei 1 2; 1 4; 3 4;
dei 2 3; 1 4; 3 4;
dei 1 2; 1 4; 2 3;
dei 1 2; 2 4; 1 2;
dei 2 3; 3 4; 1 2;
dei 2 3; 3 4; 2 3;
dei 2 3; 2 3; 2 3;
dei 3 4; 2 4; 3 4;
dei 3 4; 3 4; 2 3;
dei 4 6; 1 4; 3 4;
dei 4 5; 2 4; 2 3;
dei 5 6; 1 4; 2 3;
dei 4 6; 3 4; 1 2;
dei 5 6; 2 3; 1 2;
c charge material number
mate 11
c axis symmetric boundary
b 1 1 1 6 4 1 dz 1 rz 1 ;
b 1 1 1 6 1 4 dy 1 ry 1 ;
c establish detonation point
detp 11 point -5.30 0 0;
merge

c fluid model
block 1 21 33 34 35 36 37 38 50 70;1 2 3 4 48 50;1 2 3 4 21 25 45;-518.16
-213.36 -26.50 -15.90 -5.30 5.30 15.90 26.50 213.36 518.16;0 10.60 21.20
31.80
701.04 731.52;0 10.60 21.20 31.80 304.8 365.76 670.56;
c make deletions for fluid to make room for the explosive and barge
dei 3 8; 1 2; 1 2;
dei 4 7; 2 3; 1 2;
```

```

dei 4 7; 1 2; 2 3;
dei 5 6; 3 4; 1 2;
dei 5 6; 1 2; 3 4;
dei 5 6; 2 3; 2 3;
dei 2 9; 5 6; 5 6;
c water material nr
mate 10
c axis-symmetric boundaries
b 1 1 1 10 6 1 dz 1 rz 1 ;
b 1 1 1 10 1 7 dy 1 ry 1 ;
c non-reflective boundaries
nr 1 1 1 1 6 7
nr 10 1 1 10 6 7
nr 1 1 7 10 6 7
c establish interface along the water nodes that will interface on the
c barge nodes. Master nodes.
sid 1 ldsi p1 ; ;
si 2 5 5 2 6 6 1 m ;
si 2 5 5 9 5 6 1 m ;
si 9 5 5 9 6 6 1 m ;
si 2 5 5 9 6 5 1 m ;
si 2 5 6 9 6 6 1 m ;
merge

c air model
block 1 21 33 34 35 36 37 38 50 70;1 3 15;1 2 3 4 21 25 45;-518.16 -
213.36
-26.50
-15.90 -5.30 5.30 15.90 26.50 213.36 518.16;701.04 731.52 914.4;0 10.60
21.20
31.80 304.80 365.76 670.56;
c delete air model portions
dei 1 10; 1 2; 1 5;
dei 1 10; 1 2; 6 7;
dei 1 2; 1 2; 5 6;
dei 9 10; 1 2; 5 6;
c air material number
mate 12
c axis symmetric boundaries
b 1 1 1 10 3 1 dz 1 rz 1;
c nonreflective boundaries
nr 1 1 1 1 3 7
nr 10 1 1 10 3 7
nr 1 1 7 10 3 7
merge

c structure model
block -1 -6 -12 -17;-1 7;-1 4 -7;-213.36 -86.36 86.36 213.36;701.04
762;304.8
335.28 365.76;
c barge material nr
mate 1
c interface on the structure. Slave nodes
si 1 1 1 1 2 3 1 s ;
si 1 1 1 4 1 3 1 s ;

```

```
si 4 1 1 4 2 3 1 s ;  
si 1 1 1 4 2 1 1 s ;  
si 1 1 3 4 2 3 1 s ;
```

```
merge
```

```
c merge tolerance
```

```
stp 0.1
```

```
c point masses
```

```
pm 195338 1.16338e+5;
```

```
pm 195471 1.16338e+5;
```

```
pm 195607 1.16338e+5;
```

THIS PAGE INTENTIONALLY LEFT BLANK

APPENDIX E. LS-DYNA INPUT DECK: UNDEX 3-D MODEL WITH BLOCK TNT EXPLOSIVE MODEL

This Appendix provides the input deck used for the underwater three-dimensional model using a block TNT explosive model approach. Appendix G and references 13 and 25 offer the meaning to the command lines.

```
$ Barge model with TNT explosive offset.
$ Ted Trevino
*KEYWORD
*TITLE
Barge TNT Coupled Eulerian/Lagrangian
*CONTROL_TERMINATION
10000.,0,0.000E+00,0.000E+00,0.000E+00
*CONTROL_TIME_STEP
0,0.67
*DATABASE_BINARY_D3PLOT
200.0,0
*CONTROL_ENERGY
2,1,2,2
*DATABASE_BINARY_D3THDT
1.0,0
*DATABASE_HISTORY_NODE
124190,124173,124024,124139,124149,124134,124164,124287
*DATABASE_NODOUT
1.0
*DATABASE_GLSTAT
1.
*CONTROL_ALE
2,1,2,-1
0.
*CONSTRAINED_LAGRANGE_IN_SOLID
1,2,0,0,0,4,1,0
0,0,0.1
*SET_PART_LIST
1
1
*SET_PART_LIST
2
10,12
*ALE_MULTI-MATERIAL_GROUP_PART
10
*ALE_MULTI-MATERIAL_GROUP_PART
11
*ALE_MULTI-MATERIAL_GROUP_PART
12
*ALE_INTERFACE_RECONSTRUCTION
1
$
```

```

$ DEFINITION OF MATERIAL      1 (SHIP)
$
*MAT_PLASTIC_KINEMATIC
1,7.87,2.1,0.300,4.300E-03,0.000E+00,0.000E+00
0.000E+00,0.000E+00,0.000E+00
*HOURLASS
1,0,0.000E+00,0,0.000E+00,0.000E+00
*SECTION_SHELL
1,2,0.000E+00,3.00,0.000E+00,0.000E+00,0
0.6350,0.6350,0.6350,0.635,0.000E+00
*PART
material type # 3 (Elastic)
1,1,1,0,0,0
$
$ DEFINITION OF MATERIAL      10 (WATER)
$
*MAT_NULL
10,1.00,0.000E+00,0.000E+00,0.000E+00,0.000E+00
*EOS_GRUNEISEN
10,0.148,1.75,0.000E+00,0.000E+00,0.4934,0.000E+00,0.000E+00
1.00
*SECTION_SOLID_ALE
10,11,0
0
*PART
material type # 9 (Fluid)
10,10,10,10,11,0
$
$ DEFINITION OF MATERIAL      11 (TNT)
$
*MAT_HIGH_EXPLOSIVE_BURN
11,1.63,0.693,0.210,0.000E+00
*HOURLASS
11,0,0,0,0,0,0
*EOS_JWL
11,3.71,3.230E-02,4.15,0.950,0.300,4.300E-02,1.0
*SECTION_SOLID_ALE
11,11,0
0
*PART
material type # 8 (High Explosive Burn)
11,11,11,11,11,0
$
$ DEFINITION OF MATERIAL      12 (AIR)
$
*MAT_NULL
12,1.280E-03,0.000E+00,0.000E+00,0.000E+00,0.000E+00
*EOS_LINEAR_POLYNOMIAL
12,0.000E-00,0.0,0.000E+00,0.000E+00,0.400,0.400,0.000E+00
0.000E+00,0.000E+00
*SECTION_SOLID_ALE
12,11,0
0
*PART
material type # 9 (Fluid)

```



```

12,12,12,12,11,0
$
$ NODES
$
*NODE
1,-27.4050007,0.000000000E+00,0.000000000E+00,5,5
2,-27.4050007,0.000000000E+00,17.4500008,2,2
3,-27.4050007,17.4500008,0.000000000E+00,3,3
.
.
.
124461,213.360001,751.840027,355.600037,0,0
124462,213.360001,762.000000,345.440002,0,0
124463,213.360001,762.000000,355.600006,0,0
$
$ ELEMENT CARDS FOR SOLID ELEMENTS
$
*ELEMENT_SOLID
1,11,1,5,7,3,2,6,8,4
2,11,5,9,11,7,6,10,12,8
3,11,9,13,15,11,10,14,16,12
.
.
.
116582,12,123492,123662,123679,123509,123493,123663,123680,123510
116583,12,123662,123832,123849,123679,123663,123833,123850,123680
116584,12,123832,124002,124019,123849,123833,124003,124020,123850
$
$ ELEMENT CARDS FOR SHELL ELEMENTS
$
*ELEMENT_SHELL_THICKNESS
1,1,124021,124025,124026,124022
0.635,0.635,0.635,0.635
2,1,124025,124029,124030,124026
0.635,0.635,0.635,0.635
3,1,124029,124033,124034,124030
0.635,0.635,0.635,0.635
.
.
.
431,1,124459,124461,124432,124431
0.635,0.635,0.635,0.635
432,1,124461,124463,124433,124432
0.635,0.635,0.635,0.635
$
$ SLIDING INTERFACE DEFINITIONS
$
$
$
$ TrueGrid Sliding Interface #      1
$
*SET_SEGMENT
1,0.000E+00,0.000E+00,0.000E+00,0.000E+00
124021,124025,124026,124022,0.000E+00,0.000E+00,0.000E+00,0.000E+00
124022,124026,124027,124023,0.000E+00,0.000E+00,0.000E+00,0.000E+00
.

```

```

.
.
124448,124451,124462,124460,0.000E+00,0.000E+00,0.000E+00,0.000E+00
124460,124462,124463,124461,0.000E+00,0.000E+00,0.000E+00,0.000E+00
124461,124463,124433,124432,0.000E+00,0.000E+00,0.000E+00,0.000E+00
*SET_SEGMENT
2,0.000E+00,0.000E+00,0.000E+00,0.000E+00
14056,29430,29583,16861,0.000E+00,0.000E+00,0.000E+00,0.000E+00
16861,29583,29584,16862,0.000E+00,0.000E+00,0.000E+00,0.000E+00
16862,29584,29585,16863,0.000E+00,0.000E+00,0.000E+00,0.000E+00
.
.
.
99757,99760,99761,99758,0.000E+00,0.000E+00,0.000E+00,0.000E+00
99758,99761,99762,99759,0.000E+00,0.000E+00,0.000E+00,0.000E+00
99759,99762,71944,71926,0.000E+00,0.000E+00,0.000E+00,0.000E+00
$
$ DETONATION POINTS
$
*INITIAL_DETONATION
11,-9.14,0.000E+00,0.000E+00,0.000E+00
$
$ DISCRETE LUMPED MASSES
$
*ELEMENT_MASS
1,124126,116338.0
2,124261,116338.0
3,124392,116338.0
$
$ NONREFLECTING BOUNDARY SEGMENTS
$
*SET_SEGMENT
3,0.,0.,0.,0.
17,19,20,18,0.,0.,0.,0.
18,20,105,89,0.,0.,0.,0.
.
.
.
123799,123969,123986,123816,0.,0.,0.,0.
123816,123986,124003,123833,0.,0.,0.,0.
123833,124003,124020,123850,0.,0.,0.,0.
*BOUNDARY_NON_REFLECTING
3,0.,0.
*END

```

APPENDIX F. LS-DYNA INPUT DECK: UNDEX 3-D MODEL WITH STAIR TNT EXPLOSIVE MODEL

This Appendix provides the input deck used for the underwater three-dimensional model using a stair-cased TNT explosive model approach. Appendix G and references 13 and 25 offer the meaning to the command lines.

```
*KEYWORD
*TITLE
Barge TNT Coupled Eulerian/Lagrangian
*CONTROL_TERMINATION
10000.,0,0.000E+00,0.000E+00,0.000E+00
*CONTROL_TIME_STEP
0,0.67
*DATABASE_BINARY_D3PLOT
200.0,0
*CONTROL_ENERGY
2,1,2,2
*DATABASE_BINARY_D3THDT
1.0,0
*DATABASE_HISTORY_NODE
195467,195304,195450,195416,195426,195411,195561,195441
*DATABASE_NODOUT
1.0
*DATABASE_GLSTAT
1.
*CONTROL_ALE
2,1,2,-1
0.
*CONSTRAINED_LAGRANGE_IN_SOLID
1,2,0,0,0,4,1,0
0,0,0.1
*SET_PART_LIST
1
1
*SET_PART_LIST
2
10,12
*ALE_MULTI-MATERIAL_GROUP_PART
10
*ALE_MULTI-MATERIAL_GROUP_PART
11
*ALE_MULTI-MATERIAL_GROUP_PART
12
*ALE_INTERFACE_RECONSTRUCTION
1
$
$ DEFINITION OF MATERIAL      1 (SHIP)
$
```

```

*MAT_PLASTIC_KINEMATIC
1,7.87,2.1,0.300,4.300E-03,0.000E+00,0.000E+00
0.000E+00,0.000E+00,0.000E+00
*HOURLASS
1,0,0.000E+00,0,0,0.000E+00,0.000E+00
*SECTION_SHELL
1,2,0.000E+00,3.00,0.000E+00,0.000E+00,0
0.6350,0.6350,0.6350,0.635,0.000E+00
*PART
material type # 3 (Elastic)
1,1,1,0,0,0
$
$ DEFINITION OF MATERIAL      10 (WATER)
$
*MAT_NULL
10,1.00,0.000E+00,0.000E+00,0.000E+00,0.000E+00
*EOS_GRUNEISEN
10,0.148,1.75,0.000E+00,0.000E+00,0.4934,0.000E+00,0.000E+00
1.00
*SECTION_SOLID_ALE
10,11,0
0
*PART
material type # 9 (Fluid)
10,10,10,10,11,0
$
$ DEFINITION OF MATERIAL      11 (TNT)
$
*MAT_HIGH_EXPLOSIVE_BURN
11,1.63,0.693,0.210,0.000E+00
*HOURLASS
11,0,0,0,0,0,0
*EOS_JWL
11,3.71,3.230E-02,4.15,0.950,0.300,4.300E-02,1.0
*SECTION_SOLID_ALE
11,11,0
0
*PART
material type # 8 (High Explosive Burn)
11,11,11,11,11,0
$
$ DEFINITION OF MATERIAL      12 (AIR)
$
*MAT_NULL
12,1.280E-03,0.000E+00,0.000E+00,0.000E+00,0.000E+00
*EOS_LINEAR_POLYNOMIAL
12,0.000E-00,0.0,0.000E+00,0.000E+00,0.400,0.400,0.000E+00
0.000E+00,0.000E+00
*SECTION_SOLID_ALE
12,11,0
0
*PART
material type # 9 (Fluid)
12,12,12,12,11,0
$

```

```

$ NODES
$
*NODE
1,-26.5000000,0.000000000E+00,0.000000000E+00,5,5
2,-26.5000000,0.000000000E+00,10.6000004,2,2
3,-26.5000000,10.6000004,0.000000000E+00,3,3
.
.
.
195731,213.360001,751.840027,355.600037,0,0
195732,213.360001,762.000000,345.440002,0,0
195733,213.360001,762.000000,355.600006,0,0
$
$ ELEMENT CARDS FOR SOLID ELEMENTS
$
*ELEMENT_SOLID
1,11,1,5,7,3,2,6,8,4
2,11,5,9,11,7,6,10,12,8
3,11,6,10,12,8,13,15,16,14
.
.
.
185194,12,194559,194799,194819,194579,194560,194800,194820,194580
185195,12,194799,195039,195059,194819,194800,195040,195060,194820
185196,12,195039,195279,195299,195059,195040,195280,195300,195060
$
$ ELEMENT CARDS FOR SHELL ELEMENTS
$
*ELEMENT_SHELL_THICKNESS
1,1,195301,195305,195306,195302
0.635,0.635,0.635,0.635
2,1,195305,195309,195310,195306
0.635,0.635,0.635,0.635
3,1,195309,195313,195314,195310
0.635,0.635,0.635,0.635
.
.
.
430,1,195727,195729,195703,195702
0.635,0.635,0.635,0.635
431,1,195729,195731,195704,195703
0.635,0.635,0.635,0.635
432,1,195731,195733,181580,195704
0.635,0.635,0.635,0.635
$
$ SLIDING INTERFACE DEFINITIONS
$
$
$ TrueGrid Sliding Interface #      1
$
*SET_SEGMENT
1,0.000E+00,0.000E+00,0.000E+00,0.000E+00
195301,195305,195306,195302,0.000E+00,0.000E+00,0.000E+00,0.000E+00
195302,195306,195307,195303,0.000E+00,0.000E+00,0.000E+00,0.000E+00
.

```

```

.
.
195719,181578,195732,195730,0.000E+00,0.000E+00,0.000E+00,0.000E+00
195730,195732,195733,195731,0.000E+00,0.000E+00,0.000E+00,0.000E+00
195731,195733,181580,195704,0.000E+00,0.000E+00,0.000E+00,0.000E+00
*SET_SEGMENT
2,0.000E+00,0.000E+00,0.000E+00,0.000E+00
23234,46275,46453,26927,0.000E+00,0.000E+00,0.000E+00,0.000E+00
26927,46453,46454,26928,0.000E+00,0.000E+00,0.000E+00,0.000E+00
.
.
.
156367,156370,156371,156368,0.000E+00,0.000E+00,0.000E+00,0.000E+00
156368,156371,156372,156369,0.000E+00,0.000E+00,0.000E+00,0.000E+00
156369,156372,112306,112285,0.000E+00,0.000E+00,0.000E+00,0.000E+00
$
$ DETONATION POINTS
$
*INITIAL_DETONATION
11,-5.30,0.000E+00,0.000E+00,0.000E+00
$
$ DISCRETE LUMPED MASSES
$
*ELEMENT_MASS
1,195338,116338.0
2,195471,116338.0
3,195607,116338.0
$
$ NONREFLECTING BOUNDARY SEGMENTS
$
*SET_SEGMENT
3,0.,0.,0.,0.
51,53,54,52,0.,0.,0.,0.
52,54,136,135,0.,0.,0.,0.
.
.
.
195020,195260,195280,195040,0.,0.,0.,0.
195040,195280,195300,195060,0.,0.,0.,0.
*BOUNDARY_NON_REFLECTING
3,0.,0.
*END

```

APPENDIX G. USEFUL LS-DYNA COMMANDS

LS-DYNA [Ref. 25] version 960 (alpha) was used for the numerical computations. This Appendix covers some of the basic commands used in the input decks. The pre-processor.(TrueGrid) primarily outputs into the "trgrdo" file a listing of nodes, solids, shells, boundary conditions, point masses, and detonation points. Note: material type and equation of state information could have been input in TrueGrid, but the data input was not in this case. Since the initial material information and equation of state was not done in the pre-processor, the data was input in LS-DYNA. Reference 25 provides a detailed description of the "keyword" commands. Some of the major keywords are listed below:

- a. ***CONTROL_ALE** sets default control parameters for the Arbitrary Lagrange-Eulerian and Eulerian calculations. This command works in conjunction with ***ALE_MULTI-MATERIAL_GROUP**, and ***SECTION_SOLID_ALE**.
- b. ***ALE_MULTI-MATERIAL_GROUP_PART** defines the **PART ID**'s of each group pertaining to the Arbitrary Lagrangian-Eulerian capability.
- c. ***SECTION_SOLID_ALE** defines section material properties for solid structural and fluid elements.
- d. ***CONSTRAINED_LAGRANGE_IN_SOLID** couples the Lagrangian mesh (slaves) which can consist of shells, solids, or beams to an Eulerian flow (masters). In this command, the penalty coupling is initialized and set to a default of 0.10, although can be changed. May be subject to further study between in structural-fluid interface.
- e. ***CONTROL_ENERGY** provides controls for energy dissipation options. In this command, Rayleigh damping is initialized.
- f. ***CONTROL_TIME_STEP** sets the time step size control using a time scale factor of 0.67 or less for explosives. Any value higher may cause instabilities in the numerical solutions. Reducing the time scale factor may also may subject to additional studies.

- g. ***DATABASE_option** controls database definitions that are necessary in obtaining output files containing results. Three-dimensional plotting information is contained which is used in LS-POST. ASCII information can also be obtained for nodal or element data which can also be used in LS-POST.

APPENDIX H. USEFUL LS-POST COMMANDS

This Appendix contains some of the important LS-POST commands [Ref. 26]. LS-POST is a powerful three-dimensional post-processor, which can be used to display animation graphics as well element or nodal XY plots. In order to access the geometrical two or three-dimensional data, the **d3plot** must be selected.

In order to view the shock pressure waves, the **Fcomp** button was selected in the Main Menu Area. A list of options will appear in the Fringe component window. The **Misc** button was then selected followed by the **Pressure** option. The **Apply** button is then selected in the Fringe component window. Lastly, to view to simulation run time pressure animation, the animation control buttons are used normally in the play position, ►. The other animation control buttons can manipulated to view the animation in reverse, one state at a time, and the animation speed can also be controlled. Most of the animation feature options or selections can be selected and applied from the **Fcomp** button such as stress, strain, and energy three-dimensional plots to name a few.

To view the two or three-dimensional velocity vectors, the **Vector** button is selected from the Main menu area. Next, the **velocity** button is selected, and the vector length can also be scaled using the **SF** button to the user's appropriate needs. Then, to run the velocity animation, follow the steps from the previous paragraph.

To make a movie from the animation sequence that has been run in the graphics window, the user should select the **File** pull down menu and activate the **Movie** selection. The format used was **AVI(rle)** with the size on **NTSC**. The start button was then selected, and the animation sequence is recorded.

XY plots can also be produced using the **History** button in the Main Menu Area. The user then selects either the **Nodal** or **Element** buttons in the Time History Results window. Selecting the **Nodal** button provides nodal coordinates, displacement, velocity and acceleration. Selecting the **Element** button provides the element stresses and strains. After the **Nodal** or **Element** selection has been made, the user then selects the actual node or element in the graphics window with the mouse. After the node or element has been chosen in the graphics window, the **Plot** button in the Time History Results window is

selected. The XY plot is then produced. The plot can be saved while in XY Graph window by selecting the **Save** button. This saves the XY data into file where the data is in a two-column format.

Additionally, nodes or elements selected in LS-DYNA's ***database_option** can be plotted using the **Ascii** button in the Main Menu Area. An Ascii File operation window will appear. The **Load** button was selected followed by the **+nodout***. This generated a Nodout Data window from which the nodes that were selected from LS-DYNA's ***database_option** will appear. The appropriate node was selected with for example **Y-vel** selected. The **Plot** button is then selected in the Nodout Data window. The XY plot is then produced. The plot can be saved using the steps from the previous paragraph.

Lastly, the graphical image in the Graphics window of certain state can be saved into a file using the **File** pull down menu. Next, the **Print** command was selected. A Print Dialog window will appear and the print to **File** was selected. The file format selected was changed from the default of **PS/Image** to **BMP**, which produced the best results.

APPENDIX I. TRUEGRID COMMANDS: 2-D AIR EXPLOSION

This Appendix provides the input program used for the two-dimensional air explosion using TNT. This program provides and generates the initial input mesh. All of the structural material properties and thickness values were input into LS-DYNA. These commands offer the template for the other two air explosion scenarios. TrueGrid does offer the feature to input material properties using the LSDYMAT5 command. Appendix B and references 7 and 25 offer the meaning to the command lines.

```
c establish the air/explosive mesh
cylinder 1 2 89;1 62;1 2;0 3.54 311.52;0 90;0 3.54;
c air material nr. The nodes for the explosive are changed in LS-DYNA
c to prevent using the interface command
mate 12
c setup the detonation point
detp 11 point 0 0 0;
c establish axis-symmetric boundaries
b 1 1 1 3 1 2 dy 1 ry 1 ;
b 1 2 1 3 2 2 dx 1 rx 1 ;
c constrain nodes in the z direction to maintain problem physics
b 1 1 1 3 2 2 dz 1 rz 1 ;
merge

c establish cylindrical shell
cylinder -1;1 30;1 2;6.08;0 90;0 3.54;
c shell material number
mate 1;
merge
```

THIS PAGE INTENTIONALLY LEFT BLANK

APPENDIX J. LS-DYNA INPUT DECK: 2-D AIR EXPLOSION WITH ONE-INCH THICK STEEL

This Appendix provides the input deck used for the air explosion two-dimensional air explosion interacting with a one-inch thick steel. Appendix K and references 13 and 25 offer the meaning to the command lines.

```
*KEYWORD
*TITLE
APM Steel-TNT Coupled Eulerian/Lagrangian
*CONTROL_TERMINATION
4000.,0,0.000E+00,0.000E+00,0.000E+00
*CONTROL_TIME_STEP
0,0.67
*DATABASE_BINARY_D3PLOT
50.0,0
*CONTROL_ENERGY
2,1,2,2
*DATABASE_BINARY_D3THDT
1.0,0
*DATABASE_HISTORY_NODE
2000
*DATABASE_NODOUT
.8
*DATABASE_GLSTAT
1.
*CONTROL_ALE
2,1,2,-1
0.
*CONSTRAINED_LAGRANGE_IN_SOLID
1,2,0,0,0,4,1,0
0,0,0.1
*SET_PART_LIST
1
1
*SET_PART_LIST
2
10,12
*ALE_MULTI-MATERIAL_GROUP_PART
10
*ALE_MULTI-MATERIAL_GROUP_PART
11
*ALE_MULTI-MATERIAL_GROUP_PART
12
*ALE_INTERFACE_RECONSTRUCTION
1
$
```

```

$ DEFINITION OF MATERIAL      1 (Steel)
$
*MAT_PLASTIC_KINEMATIC
1,7.87,2.1,0.300,4.300E-03,0.000E+00,0.000E+00
0.000E+00,0.000E+00,0.0
*HOURLASS
1,0,0.000E+00,0,0.000E+00,0.000E+00
*SECTION_SHELL
1,2,0.000E+00,3.00,0.000E+00,0.000E+00,0
2.54,2.54,2.54,2.54,0.000E+00
*PART
material type # 3 (Kinematic/Isotropic Elastic-Plastic)
1,1,1,0,0,0
$
$ DEFINITION OF MATERIAL      10 (WATER) Not used in this simulation
$
*MAT_NULL
10,1.00,0.000E+00,0.000E+00,0.000E+00,0.000E+00
*EOS_GRUNEISEN
10,0.148,1.75,0.000E+00,0.000E+00,0.280,0.000E+00,0.000E+00
1.00
*SECTION_SOLID_ALE
10,11,0
0
*PART
material type # 9 (Fluid)
10,10,10,10,11,0
$
$ DEFINITION OF MATERIAL      11 (TNT)
$
*MAT_HIGH_EXPLOSIVE_BURN
11,1.63,0.693,0.210,0.000E+00
*HOURLASS
11,0,0,0,0,0,0
*EOS_JWL
11,3.71,3.230E-02,4.15,0.950,0.300,4.300E-02,1.0
*SECTION_SOLID_ALE
11,11,0
0
*PART
material type # 8 (High Explosive Burn)
11,11,11,11,11,0
$
$ DEFINITION OF MATERIAL      12 (AIR)
$
*MAT_NULL
12,1.280E-03,0.000E+00,0.000E+00,0.000E+00,0.000E+00
*EOS_LINEAR_POLYNOMIAL
12,0.000E-00,0.0,0.000E+00,0.000E+00,0.400,0.400,0.000E+00
0.000E+00,0.000E+00
*SECTION_SOLID_ALE
12,11,0
0
*PART
material type # 9 (Fluid)

```

```

12,12,12,12,11,0
$
$ NODES
$
*NODE
1,0.000000000E+00,0.000000000E+00,0.000000000E+00,5,5
2,0.000000000E+00,0.000000000E+00,3.53999996,5,5
3,0.000000000E+00,0.000000000E+00,0.000000000E+00,3,3
.
.
.
11094,0.329162806,6.07108307,3.53999996,0,0
11095,0.000000000E+00,6.07999992,0.000000000E+00,0,0
11096,0.000000000E+00,6.07999992,3.53999996,0,0
$
$ ELEMENT CARDS FOR SOLID ELEMENTS
$
*ELEMENT_SOLID
1,11,1,125,127,3,2,126,128,4
2,11,3,127,129,5,4,128,130,6
3,11,5,129,131,7,6,130,132,8
.
.
.
5367,12,10785,10909,10911,10787,10786,10910,10912,10788
5368,12,10909,11033,11035,10911,10910,11034,11036,10912
$
$ ELEMENT CARDS FOR SHELL ELEMENTS
$
*ELEMENT_SHELL_THICKNESS
1,1,11037,11039,11040,11038
02.54,2.54,2.54,2.54
2,1,11039,11041,11042,11040
02.54,2.54,2.54,2.54
.
.
.
29,1,11093,11095,11096,11094
02.54,2.54,2.54,2.54
$
$ DETONATION POINTS
$
*INITIAL_DETONATION
11,0.000E+00,0.000E+00,0.000E+00,0.000E+00
*END

```

THIS PAGE INTENTIONALLY LEFT BLANK

APPENDIX K. LS-DYNA INPUT DECK: 2-D AIR EXPLOSION WITH HALF- INCH THICK STEEL

This Appendix provides the input deck used for the air explosion two-dimensional air explosion interacting with a half-inch thick steel. Appendix G and references 13 and 25 offer the meaning to the command lines.

```
*KEYWORD
*TITLE
APM Steel-TNT Coupled Eulerian/Lagrangian
*CONTROL_TERMINATION
4000.,0,0.000E+00,0.000E+00,0.000E+00
*CONTROL_TIME_STEP
0,0.67
*DATABASE_BINARY_D3PLOT
50.0,0
*CONTROL_ENERGY
2,1,2,2
*DATABASE_BINARY_D3THDT
1.0,0
*DATABASE_HISTORY_NODE
2000
*DATABASE_NODOUT
.8
*DATABASE_GLSTAT
1.
*CONTROL_ALE
2,1,2,-1
0.
*CONSTRAINED_LAGRANGE_IN_SOLID
1,2,0,0,0,4,1,0
0,0,0.1
*SET_PART_LIST
1
1
*SET_PART_LIST
2
10,12
*ALE_MULTI-MATERIAL_GROUP_PART
10
*ALE_MULTI-MATERIAL_GROUP_PART
11
*ALE_MULTI-MATERIAL_GROUP_PART
12
*ALE_INTERFACE_RECONSTRUCTION
1
$
```

```

$ DEFINITION OF MATERIAL      1 (Steel)
$
*MAT_PLASTIC_KINEMATIC
1,7.87,2.1,0.300,4.300E-03,0.000E+00,0.000E+00
0.000E+00,0.000E+00,0.0
*HOURLASS
1,0,0.000E+00,0,0.000E+00,0.000E+00
*SECTION_SHELL
1,2,0.000E+00,3.00,0.000E+00,0.000E+00,0
1.27,1.27,1.27,1.27,0.000E+00
*PART
material type # 3 (Kinematic/Isotropic Elastic-Plastic)
1,1,1,0,0,0
$
$ DEFINITION OF MATERIAL      10 (WATER)
$
*MAT_NULL
10,1.00,0.000E+00,0.000E+00,0.000E+00,0.000E+00
*EOS_GRUNEISEN
10,0.148,1.75,0.000E+00,0.000E+00,0.280,0.000E+00,0.000E+00
1.00
*SECTION_SOLID_ALE
10,11,0
0
*PART
material type # 9 (Fluid)
10,10,10,10,11,0
$
$ DEFINITION OF MATERIAL      11 (TNT)
$
*MAT_HIGH_EXPLOSIVE_BURN
11,1.63,0.693,0.210,0.000E+00
*HOURLASS
11,0,0,0,0,0,0
*EOS_JWL
11,3.71,3.230E-02,4.15,0.950,0.300,4.300E-02,1.0
*SECTION_SOLID_ALE
11,11,0
0
*PART
material type # 8 (High Explosive Burn)
11,11,11,11,11,0
$
$ DEFINITION OF MATERIAL      12 (AIR)
$
*MAT_NULL
12,1.280E-03,0.000E+00,0.000E+00,0.000E+00,0.000E+00
*EOS_LINEAR_POLYNOMIAL
12,0.000E+00,0.0,0.000E+00,0.000E+00,0.400,0.400,0.000E+00
0.000E+00,0.000E+00
*SECTION_SOLID_ALE
12,11,0
0
*PART
material type # 9 (Fluid)

```

```

12,12,12,12,11,0
$
$ NODES
$
*NODE
1,0.000000000E+00,0.000000000E+00,0.000000000E+00,5,5
2,0.000000000E+00,0.000000000E+00,3.53999996,5,5
3,0.000000000E+00,0.000000000E+00,0.000000000E+00,3,3
.
.
.
11095,0.000000000E+00,6.07999992,0.000000000E+00,0,0
11096,0.000000000E+00,6.07999992,3.53999996,0,0
$
$ ELEMENT CARDS FOR SOLID ELEMENTS
$
*ELEMENT_SOLID
1,11,1,125,127,3,2,126,128,4
2,11,3,127,129,5,4,128,130,6
3,11,5,129,131,7,6,130,132,8
.
.
.
5367,12,10785,10909,10911,10787,10786,10910,10912,10788
5368,12,10909,11033,11035,10911,10910,11034,11036,10912
$
$ ELEMENT CARDS FOR SHELL ELEMENTS
$
*ELEMENT_SHELL_THICKNESS
1,1,11037,11039,11040,11038
1.27,1.27,1.27,1.27
2,1,11039,11041,11042,11040
1.27,1.27,1.27,1.27
.
.
.
28,1,11091,11093,11094,11092
1.27,1.27,1.27,1.27
29,1,11093,11095,11096,11094
1.27,1.27,1.27,1.27
$
$ DETONATION POINTS
$
*INITIAL_DETONATION
11,0.000E+00,0.000E+00,0.000E+00,0.000E+00
*END

```

THIS PAGE INTENTIONALLY LEFT BLANK

APPENDIX L. LS-DYNA INPUT DECK: 2-D AIR EXPLOSION WITH QUARTER- INCH THICK STEEL

This Appendix provides the input deck used for the air explosion two-dimensional air explosion interacting with a half-inch thick steel. Appendix G and references 13 and 25 offer the meaning to the command lines.

```
*KEYWORD
*TITLE
APM Steel-TNT Coupled Eulerian/Lagrangian
*CONTROL_TERMINATION
4000.,0,0.000E+00,0.000E+00,0.000E+00
*CONTROL_TIME_STEP
0,0.67
*DATABASE_BINARY_D3PLOT
50.0,0
*CONTROL_ENERGY
2,1,2,2
*DATABASE_BINARY_D3THDT
1.0,0
*DATABASE_HISTORY_NODE
2000
*DATABASE_NODOUT
.8
*DATABASE_GLSTAT
1.
*CONTROL_ALE
2,1,2,-1
0.
*CONSTRAINED_LAGRANGE_IN_SOLID
1,2,0,0,0,4,1,0
0,0,0.1
*SET_PART_LIST
1
1
*SET_PART_LIST
2
10,12
*ALE_MULTI-MATERIAL_GROUP_PART
10
*ALE_MULTI-MATERIAL_GROUP_PART
11
*ALE_MULTI-MATERIAL_GROUP_PART
12
*ALE_INTERFACE_RECONSTRUCTION
1
$
$ DEFINITION OF MATERIAL      1 (Steel)
```

```

$
*MAT_PLASTIC_KINEMATIC
1,7.87,2.1,0.300,4.300E-03,0.000E+00,0.000E+00
0.000E+00,0.000E+00,0.0
*HOURLASS
1,0,0.000E+00,0,0.000E+00,0.000E+00
*SECTION_SHELL
1,2,0.000E+00,3.00,0.000E+00,0.000E+00,0
0.635,0.635,0.635,0.635,0.000E+00
*PART
material type # 3 (Kinematic/Isotropic Elastic-Plastic)
1,1,1,0,0,0
$
$ DEFINITION OF MATERIAL      10 (WATER)
$
*MAT_NULL
10,1.00,0.000E+00,0.000E+00,0.000E+00,0.000E+00
*EOS_GRUNEISEN
10,0.148,1.75,0.000E+00,0.000E+00,0.280,0.000E+00,0.000E+00
1.00
*SECTION_SOLID_ALE
10,11,0
0
*PART
material type # 9 (Fluid)
10,10,10,10,11,0
$
$ DEFINITION OF MATERIAL      11 (TNT)
$
*MAT_HIGH_EXPLOSIVE_BURN
11,1.63,0.693,0.210,0.000E+00
*HOURLASS
11,0,0,0,0,0,0
*EOS_JWL
11,3.71,3.230E-02,4.15,0.950,0.300,4.300E-02,1.0
*SECTION_SOLID_ALE
11,11,0
0
*PART
material type # 8 (High Explosive Burn)
11,11,11,11,11,0
$
$ DEFINITION OF MATERIAL      12 (AIR)
$
*MAT_NULL
12,1.280E-03,0.000E+00,0.000E+00,0.000E+00,0.000E+00
*EOS_LINEAR_POLYNOMIAL
12,0.000E-00,0.0,0.000E+00,0.000E+00,0.400,0.400,0.000E+00
0.000E+00,0.000E+00
*SECTION_SOLID_ALE
12,11,0
0
*PART
material type # 9 (Fluid)
12,12,12,12,11,0

```

```

$
$ NODES
$
*NODE
1,0.000000000E+00,0.000000000E+00,0.000000000E+00,5,5
2,0.000000000E+00,0.000000000E+00,3.53999996,5,5
3,0.000000000E+00,0.000000000E+00,0.000000000E+00,3,3
.
.
.
11094,0.329162806,6.07108307,3.53999996,0,0
11095,0.000000000E+00,6.07999992,0.000000000E+00,0,0
11096,0.000000000E+00,6.07999992,3.53999996,0,0
$
$ ELEMENT CARDS FOR SOLID ELEMENTS
$
*ELEMENT_SOLID
1,11,1,125,127,3,2,126,128,4
2,11,3,127,129,5,4,128,130,6
3,11,5,129,131,7,6,130,132,8
.
.
.
5366,12,10661,10785,10787,10663,10662,10786,10788,10664
5367,12,10785,10909,10911,10787,10786,10910,10912,10788
5368,12,10909,11033,11035,10911,10910,11034,11036,10912
$
$ ELEMENT CARDS FOR SHELL ELEMENTS
$
*ELEMENT_SHELL_THICKNESS
1,1,11037,11039,11040,11038
0.635,0.635,0.635,0.635
2,1,11039,11041,11042,11040
0.635,0.635,0.635,0.635
3,1,11041,11043,11044,11042
0.635,0.635,0.635,0.635
.
.
.
29,1,11093,11095,11096,11094
0.635,0.635,0.635,0.635
$
$ DETONATION POINTS
$
*INITIAL_DETONATION
11,0.000E+00,0.000E+00,0.000E+00,0.000E+00
*END

```

THIS PAGE INTENTIONALLY LEFT BLANK

LIST OF REFERENCES

1. NAVSEA 0908-LP-000-3010A, *Shock Design Criteria for Surface Ships*, October 1994.
2. Military Specification, MIL-S-901D, Shock Tests, High Impact Shipboard Machinery, Equipment and Systems, Requirements for, March 1989.
3. OPNAV Instruction 9072.2, "Shock Hardening of Surface Ships", January 1987.
4. USS John Paul Jones (DDG-53) Shock Trial Final Report, AEGIS Program Manager (PMS-400), November 1994.
5. Mair, H.A. and Reese, M.R., "Simulated Ship Shock Tests/Trials?" [<http://www.ida.org/LFTEsimulation/documents/SSSTT.htm>]. Not Dated.
6. Mair, H.A., "Simulation in Support of Live Fire Test & Evaluation." [<http://www.ida.org/LFTEsimulation/documents/SSSTT.htm>]. Not Dated.
7. XYZ Scientific Applications, Inc., *TrueGrid®: A Quality Mesh in a Fraction of the Time*, Livermore, CA, 1997.
8. Livermore Software Technology Corporation, *LS-DYNA Keyword User's Manual Nonlinear Dynamic Analysis of Structures*, Livermore, CA, May 1999.
9. Wood, S.L., "Cavitation Effects on a Ship-Like Box Structure Subjected to an Underwater Explosion", Master's Thesis, Naval Postgraduate School, Monterey, CA, September 1998.
10. Mair, H.A., "Review: Hydrocodes for Structural Response to Underwater Explosions," *Shock and Vibration* 6/2 (1999), 81-96.
11. Chisum, J.E., "Simulation of the Dynamic Behavior of Explosion Gas Bubbles in a Compressible Fluid Medium", Ph.D. Dissertation, Naval Postgraduate School, Monterey, CA, December 1996.

12. Zukas, J.A., and others, *Impact Dynamics*, Kreiger Publishing Company, 1992.
13. Souli, M., "LS-DYNA Advanced Course in ALE and Fluid/Structure Coupling", Course Notes for Arbitrary Lagrangian-Eulerian Formulation Technique, Livermore Software Technology Corporation, Livermore, CA, 16 February 2000.
14. Livermore Software Technology Corporation, *LS-DYNA Theoretical Manual*, Livermore, CA, May 1998.
15. Cengel, Y.A. and Boles, M.A., *Thermodynamics: An Engineering Approach*, 3d ed., WCB McGraw Hill, 1998.
16. Shin, Y.S., and others, "Modeling mitigation effects of watershield on shock waves," *Shock and Vibration* 5 (1998), 225-234.
17. Dobratz, B.M., *LLNL Explosives Handbook, Properties of Chemical Explosives and Explosive Simulants*, University of California, Lawrence Livermore National Laboratory, Rept. UCRL-52997, 1981.
18. Cole, R.H., *Underwater Explosions*, pp. 3-13, Princeton University Press, 1948.
19. Shin, Y.S., "Overview of Underwater Shock and DDAM", Short Course Notes for 68th Shock and Vibration Symposium, Naval Postgraduate School, Monterey, CA, 1997.
20. Arons, A.B., et al, "Long Range Shock Propagation in Underwater Explosion Phenomena II," *Underwater Explosion Compendium*, Vol. 1, October 1949.
21. Costanzo, F.A. and Gordon, J.D., "An Analysis of Bulk Cavitation in Deep Water," DTNSRDC, UERD Report, May 1980.
22. Stow, B.M. and Gordon, J.D., "Bulk Cavitation Caused by a Plane Shock Wave," DTNSRDC Report 84/047, October 1984.

23. Hanselman, D. and Littlefield, B., *The Student Edition of MATLAB, Version 5 User's Guide*, Prentice Hall, 1997.
24. Higdon, A., and others, *Mechanics of Materials*, 4th ed., John Wiley & Sons, Inc., 1985.
25. Livermore Software Technology Corporation, *LS-DYNA Keyword User's Manual*, Version 950, Livermore, CA, May 1999.
26. Livermore Software Technology Corporation, "LS-POST A New Post Processor for LS-DYNA", Notes, Livermore, CA, May 1999.
27. XYZ Scientific Applications, Inc., *TrueGrid Manual*, version 2.0, XYZ Scientific Applications, Inc., 1999.

THIS PAGE INTENTIONALLY LEFT BLANK

INITIAL DISTRIBUTION LIST

	<u>No. Copies</u>
1. Defense Technical Information Center 8725 John J. Kingman Rd., Ste 0944 Ft. Belvoir, VA 22060-6218	2
2. Dudley Knox Library Naval Postgraduate School 411 Dyer Rd. Monterey, CA 93943-5101	2
3. Professor Young S. Shin, Code ME/Sg Department of Mechanical Engineering Naval Postgraduate School Monterey, CA 93943	2
4. Naval/Mechanical Engineering Curricular Office (Code 34) Department of Mechanical Engineering Naval Postgraduate School Monterey, CA 93943	1
5. LT Theodore Trevino 220 S. Indiana Weslaco, TX 78596	2
6. Michael C. Winnette Carderock Division Naval Surface Warfare Center 9500 MacArthur Blvd. West Bethesda, MD 20817-5700	1
7. Dr. Fred Randall Bath Iron Works 700 Washington St. Mail Stop 6300 Bath, ME 04530	1
8. Stephen Schreppler Office of Naval Research Code 334 800 North Quincy Street Arlington, VA 22217-5660	1

9. Brian Bonkoksy, Chief Engineer 1
U.S. Army TACOM, Grizzly Product Management Office
Attn: AMSTA-LC-AC-G(415)
Warren, MI 48397-5000
10. COL Michael K. Asada..... 1
U.S. Army TACOM, Grizzly Product Management Office
Attn: AMSTA-LC-AC
Warren, MI 48397-5000
11. Darrol Spurgeon..... 1
U.S. Army TACOM, Grizzly Product Management Office
Attn: AMSTA-LC-AC
Warren, MI 48397-5000